UNIVERSITY OF CALIFORNIA SAN DIEGO

Periodic poling of thin-film lithium niobate for second-harmonic generation and entangled photon-pair generation

A dissertation submitted in partial satisfaction of the
requirements for the degree
Doctor of Philosophy

in

Electrical Engineering (Photonics)

by

Jie Zhao

Committee in charge:

Professor Shayan Mookherjea, Chair
Professor James Friend
Professor Eric E. Fullerton
Professor Yu-Hwa Lo
Professor George C. Papen

2020

The dissertation of Jie Zhao is approved, and it is acceptable in quality and form for publication on microfilm and electronically:

_____

_____

_____

_____

_____

Chair

University of California San Diego

2020

DEDICATION

To Yue and our parents.

EPIGRAPH

There is only one heroism in the world:

to see the world as it is, and to love it.

—Romain Rolland

TABLE OF CONTENTS

LIST OF FIGURES

LIST OF TABLES

ACKNOWLEDGEMENTS

Above all, I would like to express my sincere gratitude to my advisor, Prof. Shayan Mookherjea, for the constant support and guidance of my Ph.D. study and research, for his patience in training me, and for believing in me and offering me the opportunity to work in the most creative and cooperative team that I could ever dream of. It is my great honor to be able to graduate from his group, and I could not have imagined having a better advisor for my Ph.D. study.

Besides my advisor, I would like to thank the rest of our group members, Dr. Peter O. Weigel, Dr. Michael Rüsing, Mr. Xiaoxi (Josh) Wang, Dr. Chaoxuan (Ellen) Ma, Dr. Hannah R. Grant, Mr. Forrest Valdez, and Mr. Ruoyu Zhao. It was a great pleasure working with them. Special thanks goes to my mentor Peter, who has been so patient and nice to me since the day I joined this group, sharing with me his invaluable experience and expertise in nonlinear simulations, fabrication and optical measurements without reservation. He has taught me more than I could ever give him credit for here. My sincere thanks also goes to Michael, without whom none of this would be possible. He has been my work partner, collaborator, and mentor, who was there to offer me help every time I felt frustrated and discouraged. I enjoyed and learned from every stimulating discussion that we had. He has shown me, by his example, what a good scientist should be. To Josh, for always making me feel safe and comfortable asking any questions I had in my mind anytime. I admire his abundant positive energy and enthusiasm for research and life, which has inspired and influenced me deeply. I also truly enjoyed our passionate conversations on food and movie, exchanging opinions and suggestions on our personal favorites, which have brought plenty of joy to my Ph.D. experience. I would also like to thank Ellen for her genuine suggestions and generous help over the years. I was lucky to have her as a labmate and also as a friend, with whom I could talk about my concerns in research, as well as share life experiences. I highly appreciated her help on the SPDC work, without which the experiment would not be able to run so smoothly.

To the Sandia National Laboratories team led by Dr. Anthony Lentine, for supporting my doctoral work. In particular, I would like to thank Anthony, for his constant support and timely help on the SHG project, for his efforts in realizing our design ideas, and for recognizing our work.

I would also like to thank our collaborators from University of Rochester, Prof. Qiang Lin, Mr. Usman A. Javid, Mr. Jingwei Ling, Mr. Mingxiao Li, and Dr. Rui Luo, for their help in fabricating the TFLN waveguides, and for their patience and trust while we were drafting and revising the SHG paper. Also to our collaborators from Technische Universität Dresden, Prof. Lukas M. Eng, Dr. Michael Rüsing, and Mr. Matthias Roeper, for providing the beautiful PFM images of our PPLN chips.

I acknowledge all the staff engineers and friends that I was blessed to meet in the Nano3 cleanroom, because of whom, I was able to enjoy the time I spent in the cleanroom. Especially to Mr. Sean Parks, for training and authorizing me on all the thin-film deposition machines in the cleanroom, before when I was still too afraid to fill up the liquid nitrogen bucketback by myself. To Mr. Larry Grissom, for being extremely patient and kind to me, even when I used to break the gold wire of the wire bonder every time I used it in my first year. I know how tedious and tiring it is to get the bonder back in shape. To Dr. Xuekun Lu, for sharing with me his precious experience in micro-fabrication. To Dr. Junhee Park, for offering me generous help, comfort, and encouragement whenever I needed it. I wish nothing but the best for him and his family.

I thank Prof. Zhaowei Liu, for his guidance in the first one and a half years of my Ph.D. study, and for his understanding and support when I decided to switch to my current group.

To my parents, for respecting my every single choice and for believing in me unconditionally. It is my biggest wish that one day I could be with them whenever I want and anytime they need me, and show them the bigger world that I have seen all these years when I am far away from home. To my brother and my sister-in-law, for supporting me, and for taking care of our parents. To my two lovely nephews, for bringing joy and happiness to their grandparents, and for

keeping them company.

To all the extraordinary artists who created the music in my playlist, which brightened up all my sleepless nights in the lab. In particular, to Johann Sebastian Bach, Claude Debussy, Queen, The Beatles, New Pants, Linkin Park and Taylor Swift, for their masterpieces, which resonated deep in my heart and brought me restfulness and delight in the darkest days.

Finally, I acknowledge my significant other, Yue. Meeting him in graduate school is the most wonderful thing that has ever happened to me. He has been my most intimate friend, and the only person, with whom I feel absolutely safe to share all my feelings, emotions and thoughts. I admire his inherent optimistic attitude to life, his unconditional kindness to others, and the great patience and persistence that he possesses in research. I am glad that we have witnessed each other's growth over the years. All my successes are shared with him.

Jie Zhao

San Diego, CA

Thanksgiving

Chapter 3, contains the material as it appears in the following: Jie Zhao, Michael Rüsing, and Shayan Mookherjea, "Optical diagnostic methods for monitoring the poling of thin-film lithium niobate waveguides", Optics Express 27 (9), 12025 (2019) and Jie Zhao, Michael Rüsing, Matthias Roeper, Lukas M. Eng, and Shayan Mookherjea, "Poling thin-film x-cut lithium niobate for quasi-phase matching with sub-micrometer periodicity", Journal of Applied Physics 127, 193104 (2020). The dissertation author, together with her adviser, led the research efforts for this work and co-authored the paper.

Chapter 4, contains the material as it appears in the following: Jie Zhao, Michael Rüsing, Usman A. Javid, Jingwei Ling, Mingxiao Li, Qiang Lin, and Shayan Mookherjea, "Shallow-etched thin-film lithium niobate waveguides for highly-efficient second-harmonic generation", Optics Express 28(13), 19669 (2020). The dissertation author, together with her adviser, led the research efforts for this work and co-authored the paper.

Chapter 5, contains the material as it appears in the following: Jie Zhao, Michael Rüsing, Usman A. Javid, Jingwei Ling, Mingxiao Li, Qiang Lin, and Shayan Mookherjea, "Shallow-etched thin-film lithium niobate waveguides for highly-efficient second-harmonic generation", Optics Express 28(13), 19669 (2020). The dissertation author, together with her adviser, led the research efforts for this work and co-authored the paper.

Chapter 6, contains the material as it appears in the following: Jie Zhao, Chaoxuan Ma, Michael Rüsing, and Shayan Mookherjea, "High-quality entangled photon-pair generation in periodically-poled thin-film lithium niobate waveguides", Physical Review Letters 124, 163603 (2020). The dissertation author, together with her adviser, led the research efforts for this work and co-authored the paper.

Appendix B, contains the material as it appears in the following: Jie Zhao, Michael Rüsing, Matthias Roeper, Lukas M. Eng, and Shayan Mookherjea, "Poling thin-film x-cut lithium niobate for quasi-phase matching with sub-micrometer periodicity", Journal of Applied Physics 127, 193104 (2020). The dissertation author, together with her adviser, led the research efforts for this work and co-authored the paper.

Appendix C, contains the material as it appears in the following: Jie Zhao, Michael Rüsing, Usman A. Javid, Jingwei Ling, Mingxiao Li, Qiang Lin, and Shayan Mookherjea, "Shallow-etched thin-film lithium niobate waveguides for highly-efficient second-harmonic generation", Optics Express 28(13), 19669 (2020). The dissertation author, together with her adviser, led the research efforts for this work and co-authored the paper.

Appendix D, contains the material as it appears in the following: Jie Zhao, Michael Rüsing, Usman A. Javid, Jingwei Ling, Mingxiao Li, Qiang Lin, and Shayan Mookherjea, "Shallow-etched thin-film lithium niobate waveguides for highly-efficient second-harmonic generation", Optics Express 28(13), 19669 (2020). The dissertation author, together with her adviser, led the research efforts for this work and co-authored the paper.

VITA

2014	B. S. in Optical Information Science and Technology, China University of Mining and Technology
2018	M. S. in Electrical Engineering (Photonics), University of California San Diego
2020	Ph. D. in Electrical Engineering (Photonics), University of California San Diego

PUBLICATIONS

Jie Zhao, Chaoxuan Ma, Michael Rüsing, and Shayan Mookherjea, "High-quality entangled photon-pair generation in periodically-poled thin-film lithium niobate waveguides", Physical Review Letters 124, 163603, 2020.

Jie Zhao, Michael Rüsing, Usman A. Javid, Jingwei Ling, Mingxiao Li, Qiang Lin, and Shayan Mookherjea, "Shallow-etched thin-film lithium niobate waveguides for highly-efficient second-harmonic generation", Optics Express 28(13), 19669, 2020.

Jie Zhao, Michael Rüsing, Matthias Roeper, Lukas M. Eng, and Shayan Mookherjea, "Poling thin-film x-cut lithium niobate for quasi-phase matching with sub-micrometer periodicity", Journal of Applied Physics 127, 193104, 2020.

Jie Zhao, Michael Rüsing, and Shayan Mookherjea, "Optical diagnostic methods for monitoring the poling of thin-film lithium niobate waveguides", Optics Express 27(9), 12025, 2019.

Jie Zhao, Chaoxuan Ma, Michael Rüsing, and Shayan Mookherjea, "High-quality photon-pair and heralded single-photon generation using periodically-poled thin-film lithium niobate", Frontiers in Optics, paper FTu6A.3, 2019.

Michael Rüsing, Jie Zhao and Shayan Mookherjea, "Second harmonic microscopy of poled x-cut thin film lithium niobate: Understanding the contrast mechanism", Journal of Applied Physics 126(11), 114105, 2019.

Peter O. Weigel, Jie Zhao, Kelvin Fang, Hasan Al-Rubaye, Douglas Trotter, Dana Hood, John Mudrick, Christina Dallo, Andrew T. Pomerene, Andrew L. Starbuck, Christopher T. DeRose, Anthony L. Lentine, Gabriel Rebeiz, and Shayan Mookherjea, "Bonded thin film lithium niobate modulator on a silicon photonics platform exceeding 100 GHz 3-dB electrical modulation bandwidth", Optics Express 26(18), 23728, 2018.

Peter O. Weigel, Jie Zhao, Douglas Trotter, Dana Hood, John Mudrick, Christina Dallo, Andrew T. Pomerene, Andrew L. Starbuck, Christopher T. DeRose, Anthony L. Lentine, and Shayan Mookherjea, "Foundry-compatible Hybrid Silicon/Lithium Niobate Electro-Optic Modulator", Conference on Lasers and Electro-Optics (CLEO), paper SF2I.4, 2018.

Xiaoxi Wang, Peter O. Weigel, Jie Zhao, Michael Rüsing, and Shayan Mookherjea, "Achieving beyond-100-GHz large-signal modulation bandwidth in hybrid silicon photonics Mach Zehnder modulators using thin film lithium niobate", APL Photonics 4(9), 096101, 2019.

Michael Rüsing, Peter O. Weigel, Jie Zhao, and Shayan Mookherjea, "Toward 3D Integrated Photonics Including Lithium Niobate Thin Films: A Bridge Between Electronics, Radio Frequency, and Optical Technology", IEEE Nanotechnology Magazine 13(4), 18, 2019.

Peter O. Weigel, Forrest Valdez, Jie Zhao, Huiyan Li, and Shayan Mookherjea, "Design of High-Bandwidth, Low-Voltage and Low-Loss Hybrid Lithium Niobate Electro-Optic Modulators", Journal of Physics: Photonics 3, 012001, 2021.

Haoliang Qian, Su-Wen Hsu, Kargal Gurunatha, Jie Zhao, Conor T Riley, Dylan Lu, Andrea R Tao, and Zhaowei Liu, "Investigation of the light generation from crystalline Ag-cubes based metal-insulator-metal tunnel junctions", Conference on Lasers and Electro-Optics (CLEO), paper FM3H.7, 2017.

Haoliang Qian, Su-Wen Hsu, Kargal Gurunatha, Conor T. Riley, Jie Zhao, Dylan Lu, Andrea R. Tao, and Zhaowei Liu, "Efficient light generation from enhanced inelastic electron tunnelling", Nature Photonics 12(8), 485, 2018.

Sven Reitzig, Michael Rüsing, Benjamin Kirbus, Joshua Gössel, Ekta Singh, Lukas M. Eng, Jie Zhao, and Shayan Mookherjea, "μ-Raman Investigations of Periodically-Poled X-Cut Thin-Film Lithium Niobate for Integrated Optics", 2020 Joint Conference of the IEEE International Frequency Control Symposium and International Symposium on Applications of Ferroelectrics (IFCS-ISAF), 2020.

M. Rüsing, M. Roeper, Z. Amber, B. Kirbus, L.M. Eng, J. Zhao, and S. Mookherjea, "Periodic Poling of X-Cut Thin-Film Lithium Niobate: The Route to Submicrometer Periods", 2020 Joint Conference of the IEEE International Frequency Control Symposium and International Symposium on Applications of Ferroelectrics (IFCS-ISAF), 2020.

ABSTRACT OF THE DISSERTATION

Periodic poling of thin-film lithium niobate for second-harmonic generation and entangled photon-pair generation

by

Jie Zhao

Doctor of Philosophy in Electrical Engineering (Photonics)

University of California San Diego, 2020

Professor Shayan Mookherjea, Chair

High-fidelity periodic poling of thin film lithium niobate (TFLN) waveguides is critical for robust, quasi-phase-matched three-wave mixing process such as second-harmonic generation and spontaneous parametric down conversion. Over the past decade, extensive research has been performed on design and fabrication of TFLN based optical waveguides, demonstrating high-performance electro-optic modulators, efficient wavelength converters and revealing their great potentials in heterogeneous integration with the conventional silicon photonic material platform. However, studies on poling of TFLN are still lacking, and uniformity of TFLN poling needs to be further improved, to achieve a comparable conversion efficiency as in its bulk counterparts. This

dissertation discusses evaluation and optimization of TFLN poling, waveguide design, and device demonstration through characterization of efficient second-harmonic generation and high-quality entangled photon-pair generation. The results presented here indicate promising applications for robust and efficient TFLN devices in nonlinear and quantum optics in the telecommunications regime.

Chapter 1

Introduction

1.1 Motivation

1.1.1 Periodic poling of thin-film lithium niobate

Periodically-poled lithium niobate (PPLN), which can achieve quasi-phase matching (QPM) of nonlinear interactions between different wavelengths, is widely used to realize waveguide devices for applications in quantum communication [1, 2], optical parametric oscillators [3, 4, 5], and wavelength converters [6, 7]. Further improvements in performance (e.g., enhanced nonlinear conversion efficiency and reduced footprint) are anticipated when using thin-film lithium niobate (TFLN), which achieves a smaller mode cross-sectional area, and thus, higher nonlinear conversion efficiency, compared to the traditional Ti diffused or proton-exchanged LN waveguides. Thus, high-fidelity periodic poling of TFLN will be essential for efficient integrated nonlinear optical devices using the TFLN materials platform, which are recently being studied [8, 9, 10, 11, 12, 13].

Periodic poling of LN is achieved by the application of a strong electric field to the crystal through lithographically-defined electrodes on LN surfaces. The electrodes are fabricated in a periodic pattern, which creates a periodic reversal of the ferroelectric domain orientation, and the

resulting periodicity of the nonlinear polarization achieves a crystal momentum that assists in phase-matching of waves that would normally not interact. At the microscopic level, uniform and accurately-sized periodically-inverted domains are the sign of high poling quality. The most popular conventional way to evaluate poling quality is one based on selective HF etching [14] combined with SEM imaging, but the process is difficult to control in LN thin films. Especially for x-cut TFLN, the buried oxide layer underneath the LN thin film itself can be etched by HF. To estimate the poling depth, FIB is often required to first expose the xy face of LN, and then the cross-section of the material is immersed and wet-etched in the HF solution, during which the top LN thin-film layer could collapse very easily. Moreover, the process of HF etching also damages the LN waveguide itself, and is not a method that can be used for in-process diagnostics of the same waveguide. Thus, there is need to develop diagnostic methods for studying the poling characteristics of TFLN devices, and in particular, in-situ methods that do not destroy the waveguide or the surrounding materials.

1.1.2 Second-Harmonic Generation

Over the past few years, many efficient wavelength converters have been demonstrated based on x-cut and y-cut thin-film PPLN waveguides [8, 9, 10, 11, 12, 13]. Because of the tight light confinement in the thin-film waveguides, more than one order of magnitude improvement have been achieved in the normalized conversion efficiency (η_{norm}) [10], compared to the traditional proton-exchanged bulk LN waveguides [6]. This waveguide structure allows access to the highest second-order nonlinear coefficient of LN (d_{33}), and enables poling with electrodes fabricated on the surface of the thin film of LN. The required poling period (Λ) for the first-order QPM in TFLN waveguides is generally much smaller than that of the bulk waveguides, because of the high dispersion of the confined modes with smaller cross-sectional area. In most of the reported TFLN SHG devices, Λ is 4 - 6 μm. The theoretical η_{norm} can be further improved, according to our simulations as well as the simulations in Refs. [11, 13], if a lower value of Λ can be fabricated.

However, lateral spreading of the inverted domains becomes non-negligible when Λ gets smaller, which hinders the realization of $\sim 50\%$ poling duty cycle and more importantly, adjacent domains may merge before the thin film is completely inverted in depth. Recently, Rao *et al.* [13] have demonstrated a high value of $\eta_{\text{norm}} \approx 4600\ \%.\text{W}^{-1}.\text{cm}^{-2}$ from a relatively short etched PPLN waveguide (0.3 mm length). However, because the length of the waveguide is on sub-millimeter scale, the measured conversion efficiency ($\eta = 10\ \%.\text{W}^{-1}$) is still significantly lower than other bulk ($\eta_{\text{max}} = 1634\ \%.\text{W}^{-1}$ [6]) or thin-film devices ($\eta_{\text{max}} = 416\ \%.\text{W}^{-1}$ [10]). Therefore, as is mentioned by the authors, the uniformity of poling needs to be further improved, to achieve a comparable conversion efficiency (η) as in the bulk PPLN waveguides. While the conversion efficiency can be further enhanced through resonant structures, as have been demonstrated in z-cut TFLN microrings very recently [15], resonant devices do not support broadband conversion, the operating temperature range is limited, and the device performance is more sensitive to fabrication errors. Thus, it is important to understand and improve the poling process, to fabricate longer waveguides, and design waveguide structures whose SHG performance will remain relatively insensitive to fabrication or layer-thickness variations.

1.1.3 Spontaneous Parametric Down-Conversion

Spontaneous parametric down-conversion (SPDC) was widely used to generate the entangled photons used in first demonstrations of quantum teleportation, entanglement-based cryptography, satellite-ground quantum communication experiments, tests of Bell's inequality, multi-photon entanglement, one-way optical quantum computing and other notable experiments [16, 17, 18, 19, 20, 21, 22, 23]. Nanoscale waveguides, which reduce the modal cross-section area by 10x compared to traditional LN waveguides, could result in lowering the power requirements by a factor of 100x and simultaneously improve the quality of the generated photon pairs. This double advantage could enable large-scale multiplexing and scale-up towards realistic quantum information processing photonic circuits, which so far is based on other materials with a

weaker, third-order nonlinearity like silica or silicon [24, 25, 26]. Periodic poling in a ferroelectric waveguide allows quasi phase matching (QPM) between waves of different frequencies and type-0 QPM with a first-order grating offers the most efficient and desired multi-wave interaction with free choice in the state of polarization and mode [3]. The second-order nonlinear optical process of SPDC in traditional LN waveguides can yield photon pairs of high quality but is relatively inefficient, typically requiring a dedicated tens-of-milliwatt-class single-mode laser diode or a high-peak power mode-locked laser for a bright, high-quality entangled-photon source [27, 28]. Efficient telecommunications-band entangled photon pair generation at sub-milliwatt power levels has, for example, been developed in silicon photonics, but at the cost of using a weaker, third-order optical nonlinearity and achieving the best performance from micro-resonator devices, which require stringent control and stabilization [29, 30]. Thus, the realization of high-quality SPDC in nanoscale LN waveguides is under active study.

1.2 Overview of this Dissertation

This dissertation discusses periodic poling of TFLN and its applications for second-harmonic generation and entangled photon-pair generation. The dissertation is organized as follows: Chapter 2 introduces the LNOI material platform and compares waveguides in bulk LN and TFLN, Chapter 3 demonstrates periodic poling of TFLN, where two different poling diagnostic methods are introduced. A new non-destructive optical diagnostic method, confocal scanning second-harmonic microscopy, is established and discussed in detail. It can image the inverted domains in both bulk and thin-film LN non-invasively, and it allows us to unambiguously distinguish between a fully-inverted and partially-inverted film in depth within the limits of lateral resolution. This technique provides quick feedback and guidance for the poling recipe optimization. Using this approach, we were able to demonstrate uniformly-inverted domains over a 5 mm long poling region, with a 2.8 μm period. Poling results of domain structures with

sub-micrometer periodicities are presented and analyzed based on the measured SH and PFM images. Chapter 4 discusses the design of the PPLN waveguides for efficient SHG from 1560 nm to 780 nm. Chapter 5 presents SHG measurement results from the fabricated PPLN waveguides, including the measured SHG spectra, SH-pump power dependence, as well as tuning of the SHG spectra through variations in both the waveguide geometry and the temperature. Chapter 6 reports measurements of time-frequency entangled photon pairs generated from the PPLN waveguides using SPDC, with a high Coincidences-to-Accidentals Ratio (CAR) at high pair brightness, a low value of the conditional self-correlation function [$g_H^{(2)}(0)$], and high two-photon energy-time Franson interferometric visibility, which demonstrate the high quality of the entangled photon pairs and heralded single photons.

Chapter 2

Thin-film Lithium Niobate

2.1 Lithium Niobate

Lithium niobate ($LiNbO_3$) is a human-made dielectric material that is first grown in the single crystal form by Czochralski technique in Bell Laboratories in 1965 [31]. Details of its growth, crystal structures and domain structures were reported in the subsequent publications in 1966 [32, 33, 34, 35, 36]. It has a trigonal crystal system which exhibits ferroelectricity, piezoelectricity, pyroelectricity, the Pockels effect, and second-order optical nonlinearity. The versatility of lithium niobate makes it widely used in a broad range of applications including electro-optic modulators, surface acoustic wave devices, optical frequency doublers, and optical parametric oscillators. In particular, lithium niobate is the material of choice as nonlinear photonic devices owing to its large electro-optic coefficient ($r_{33} \approx 31\ pm.V^{-1}$ at 633 nm) [37], strong second-order nonlinear coefficient ($d_{33} \approx 27\ pm.V^{-1}$ at 1064 nm) [38], and broad transparent window (350 nm - 5 μm) [39]. According to a recent industry report [40], the global market estimate for lithium niobate modulators may reach to $36.711 billion by 2026, increasing from $6.568 billion in 2018. Therefore, research into improving lithium niobate photonic devices may translate into technological advances and societal benefit.

2.1.1 Waveguides in Lithium Niobate

Fabrication of waveguides in LN is crucial for its applications in integrated photonics, which require low power consumption, small device footprint and reduced fabrication cost. The essence of waveguide formation in a material is to increase the light confinement in a certain region (known as the core), by introducing an index difference between the waveguide core and the cladding material. In bulk LN, this is usually achieved by Ti in-diffusion or proton exchange, and the fabricated waveguides are called channel waveguides. In the Ti in-diffusion process, Ti diffuses in to the LN crystal as a results of cationic migration, from a thin-layer of Ti strip deposited on the surface of the crystal. Through thermal annealing (at temperatures from hundreds to a thousand degrees Celsius), the Ti strip first oxidizes and forms TiO_2, then Ti^{4+} ions diffuses into the crystal and occupies vacant Li and Nb sites [41], while simultaneously Li^+ and Nb^{5+} diffuse into the TiO_2 strip. The formed waveguide has a bell-shaped refractive index distribution in both the lateral and in-depth directions, with an increase in both the ordinary and extraordinary refractive indices of $\Delta n_e < 0.04$ and $\Delta n_o < 0.02$ [42]. Therefore, Ti in-diffused LN waveguides provide light confinement for both TE and TM modes. Proton exchange is another conventional technique to fabricate waveguides in LN. During this process, LN crystal is immersed in a proton source, which is usually an acid or hydrate melt, and heated for several hours at temperatures varying from 150 to 300 degrees Celsius. Under these conditions, Li^+ ions are replaced by H^+ protons, and thus introduces an increase in the extraordinary refractive index ($\Delta n_e \simeq 0.1$) and a reduction in the ordinary refractive index ($\Delta n_o \simeq -0.05$) of the crystal [42]. Proton exchange is usually complemented with a post-annealing step to improve the nonlinear and piezoelectric properties of the crystal, which are degraded in the standard proton exchange process [41, 42]. Compared to the Ti in-diffused waveguides, the proton exchanged waveguides can only guide one single polarization, which places a certain limitation for applications.

Waveguides in LN crystal can also be formed by plasma etching combined with Ti in-diffusion [43] or proton exchange [44], precision diamond saw cutting [45], and wet etching [46].

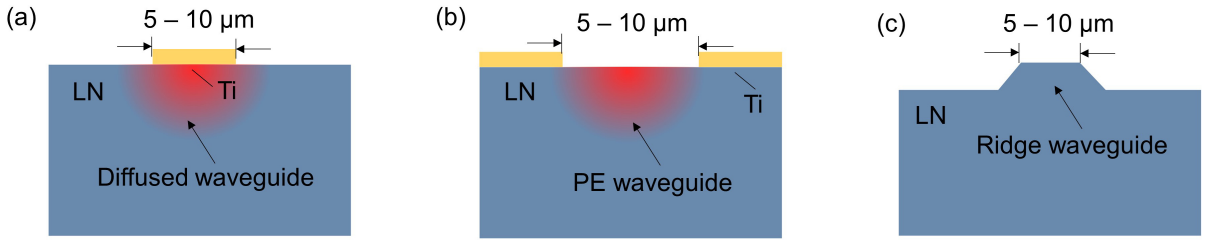

Figure 2.1: Cross sections (not to scale) of Ti in-diffused (a), proton exchanged (b) and ridge (c) waveguiding structures in bulk LN. PE: Proton exchanged.

These ridge waveguides provide a stronger light confinement compared to the channel waveguides through the large refractive index difference between the waveguide core (LN, $n_o \approx 2.2$) and the cladding material, which is often air ($n = 1$) or SiO_2 ($n \approx 1.44$).

2.2 Lithium Niobate On Insulator

Although waveguides in bulk LN bring a certain degree of light confinement, the mode area is still quite high ($> 25\ \mu m^2$), which results in large bending radii, high half-wave voltage-length product ($V_\pi L$) for electro-optic modulators, limited conversion efficiency for nonlinear optical devices, compromising footprint and integration density of the fabricated devices [47, 48]. To overcome these drawbacks, in the past two decades, extensive research efforts have been devoted to the development of thin-film LN. In 1998, 10 μm thick free-standing LN films were demonstrated by Levy et al. [49] through crystal ion slicing. These single-crystal films were proved to have the same dielectric and pyroelectric properties at room temperature, and ferroelectric transition temperature as the bulk crystals. Subsequently, a 0.68 μm thick LN thin-film was produced and bonded to a LN substrate over an area of $\sim 1\ cm^2$ [50]. In 2010, wafer-scale (3-inch diameter) LN single-crystal films of 0.76 μm thickness was reported by Hu et al. [51]. Inspired by name of silicon on insulator (SOI) wafers, which are also fabricated using ion slicing and layer transfer, the resulting material platform is called lithium niobate on insulator

(LNOI). Later in 2013, researchers from CREOL demonstrated 3-inch LNOI wafers with Si substrates, paving the way heterogeneous integration of TFLN devices with the traditional Si photonic devices. Nowadays, optical-quality LNOI wafers with sizes up to 6 inches are available from several vendors [52, 53, 54], accelerating the development of this platform.

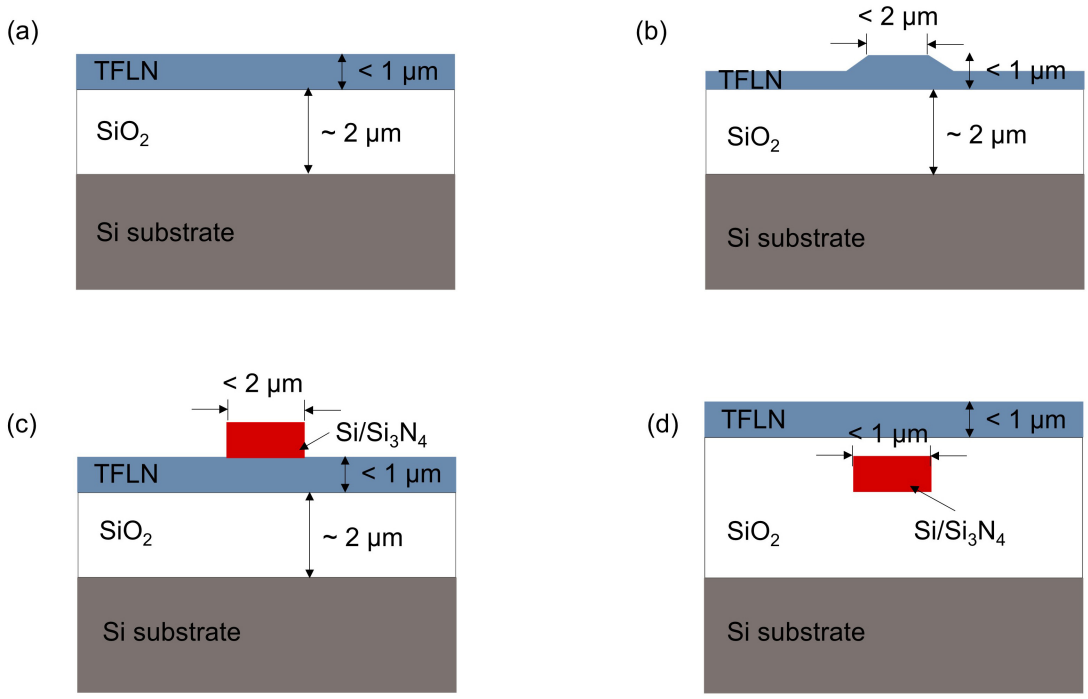

Figure 2.2: Cross sections (not to scale) of TFLN (a), dry-etched TFLN waveguides (b), Si/Si_3N_4 rib-loaded TFLN waveguides (c) and bonded hybrid Si/Si_3N_4 - TFLN waveguides.

2.2.1 Waveguides in LNOI

As is shown in Fig. 2.2(a), in cross section, LNOI wafers consist of a top functional layer, which is several hundred of nanometers thick TFLN, and the thin film is bonded to Si or LN substrates with an insulator layer in between. Waveguides in LNOI can be formed by dry etching [see Fig. 2.2(b)], waveguide rib-loading [see Fig. 2.2(c)], and heterogeneous integration with Si waveguides [see Fig. 2.2(d)]. In either waveguiding structure, because of the strong light confinement in both lateral and vertical directions, mode areas as small as $\leq 1\ \mu m^2$ are achieved,

drastically improving the device performances. For electro-optic modulators, the reduction in the optical mode size allows for much smaller gaps between the signal and ground electrodes (without compromising the waveguide propagation loss), and thus about 5-times improvement has been demonstrated in $V_\pi L$ [55, 56]. More than 20-times enhancement has been reported for the normalized wavelength conversion efficiency of frequency doublers, as the nonlinear interaction strength is proportional to light intensity in the optical waveguides [57, 13, 58]. Bending radius as small as 10 μm has been achieved on the Si-TFLN platform [59], while for the Ti in-diffused bulk LN waveguides a radius of curvature larger than 25 mm is needed for negligible bending losses [60]. The LNOI platform enables heterogeneous integration with the SOI material platforms through direct die bonding [61]. Table 2.1 summaries and compares different technical properties reported for waveguides based on bulk LN and LNOI material platform.

Table 2.1: Comparison of technical properties reported for waveguides based on bulk LN and LNOI.

Platform	Bulk LN	LNOI
Propagation loss (1550 nm)	0.02 - 1 dB/cm [41]	0.03 - 3 dB/cm [67, 68]
Mode area	5 - 25 μm^2 [69]	$\sim 1\ \mu m^2$
Material index contrast	$\Delta n_e \simeq 0.1$ [42]	$\Delta n_e \approx 0.7$ (SiO_2/LN)
Bending radius	30 mm [60]	10 μm [59]

Polarization elements such as mode convertors and polarization rotators could be demonstrated in dry-etched LNOI waveguides, as the strong material birefringence of LN can be managed to compensate for the structural birefringence of LNOI ridge waveguides. For example, mode hybridization between the fundamental TE_0 and TM_0 mode was observed in microring resonators fabricated based on x-cut LNOI ridge waveguides [62]. A TE/TM-pass polarizer design

has been proposed based on x-cut LNOI ridge waveguides, where by varying the ridge waveguide height, the unwanted polarization would radiate into the slab mode [63]. On the other hand, the strongly confined optical mode in LNOI based waveguides brings challenges for coupling to optical fibers. For edge couplers, because of the large mode mismatch between the optical mode in LNOI waveguides and that in optical fibers, mode size converters are required for efficient coupling. Typical edge coupling losses for the fundamental TE optical mode of dry-etched waveguide structures in x-cut TFLN are 5 - 10 dB/facet [64, 10, 58]. Further improvements in the edge coupling efficiency could be achieved using a bilayer tapered mode size converter, where a 1.7 dB/facet coupling loss has been demonstrated from a dry-etched LNOI waveguide (with a 1 μm thick SiO_2 cladding layer) to a high numerical aperture fiber (MFD $\approx$ 3.2 μm) [65]. Grating couplers could also be used for coupling, which enable wafer-scale optical testing and provide higher alignment tolerance compared to edge couplers, but at the cost of coupling efficiency and working bandwidth. To improve the coupling efficiency, often a reflective gold layer is used, which reflects the optical power radiated towards the substrate. For dry-etched z-cut LNOI waveguides, coupling loss of $\approx$ 3.5 dB/coupler and $\approx$ 7.1 dB/coupler has been achieved for TE and TM polarized light respectively [66].

Chapter 3

Periodic Poling of TFLN

3.1 Poling Setup

In LN, poling is most commonly achieved by the application of a strong electric field along the ferroelectric z axis of the crystal. During the electric field poling process, new domains nucleate at the poling electrodes and predominantly grow along the z axis (forward growth), while at the same time spreading laterally. We consider electrical poling of x-cut TFLN, in which configuration the surface normal of the film is along the x-axis of the LN crystal. X-cut TFLN allows for poling with surface electrodes, while poling z-cut TFLN often requires buried electrodes [70], which is not favorable for low-loss optical waveguide applications due to the resulting presence of buried metal electrodes in the vicinity of the optical mode. Alternatively, the poling ground electrode for z-cut TFLN can be formed at the backside of the chip handle, yet elevated poling temperature is needed to reduce the coercive field of LN and thus the poling voltage [15]. In addition, x-cut TFLN permits access to the largest second-order nonlinear coefficient of the crystal (d_{33}) through the TE-polarized optical modes.

Poling of the sample was realized by applying high voltage pulses to the lithographically-defined surface electrodes. As is shown in Fig. 3.1, an arbitrary waveform generator (AWG) is

used to create the tailored poling waveform, which is amplified by a high voltage amplifier (HVA). The high voltage pulse is then applied through a poling circuit to the surface of the TFLN sample, using two Tungsten needle probes with transformer oil surrounding the probe-pad contact point and the immediate vicinity of the electrodes.

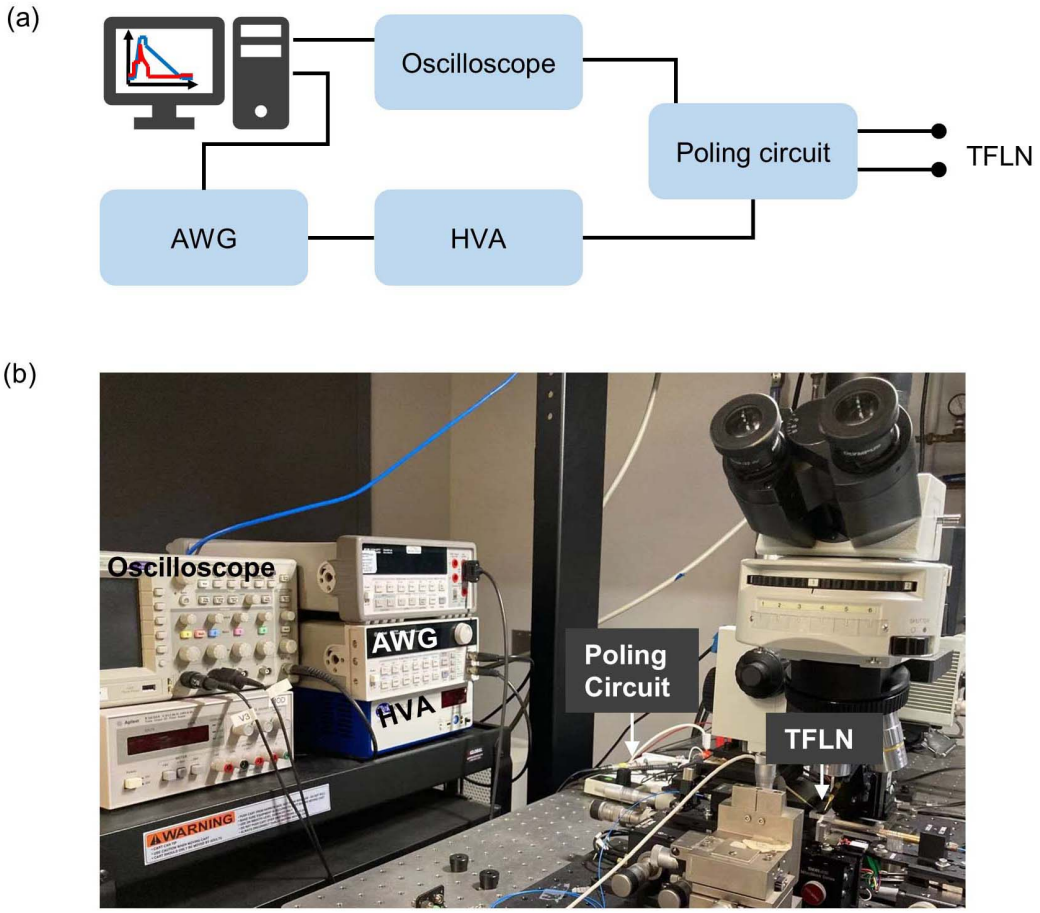

Figure 3.1: Schematic illustration (a) and photograph (b) of the poling setup.

3.2 Mechanism of Domain Growth

Electric-field-driven ferroelectric domain reversal in LN is typically characterized in four steps [71]: (1) nucleation of new domains, (2) axial growth along the z axis of the crystal, (3) lateral spread and growth in the x and y directions of the crystal and (4) coalescence of

neighboring domains. Domain reversal in bulk and thin-film LN is usually observed to start at the positive electrode [72, 73], which is traced back to the difference in Schottky barriers at polar surfaces in LN [74]. The nucleation probability of new domains scales exponentially with the applied field [75, 76]. Therefore, we expect domain nucleation to start only close to the positive electrode tips. The domain propagation speed is characterized by a pronounced asymmetry, where the growth in the axial direction is about two to three orders of magnitude larger, than the spread in the lateral direction. Domains in congruent lithium niobate typically grow in hexagonal cross sections in the *x*-*y* plane, with the *y* axis of the crystals pointing into the corners of the hexagon [73].

3.3 Second-Harmonic Microscope Imaging

Perhaps the most popular conventional way to evaluate poling quality is one based on selective HF etching [14], but the process is difficult to control in thin LN films, and especially in hybrid devices which include materials, such as silicon dioxide, which are themselves etched by HF. Moreover, the process of HF etching also damages the LN waveguide itself, and is not a method that can be used for in-process diagnostics of the same waveguide. In bulk crystals, confocal Raman microscopy [77, 78, 79] can provide a 3D visualization of domains, but only offers a depth resolution of about 1 μm, which is too large for the TFLN thickness. PFM is a standard technique for investigation of surface ferroelectric domain structures with nanometer resolution. While the PFM amplitude signal can potentially provide depth information for thin films [80, 81], it is not well-suited for imaging over chip-scale areas as required here in terms of the scanning speed. Thus, there is need to develop non-destructive diagnostic methods for studying the poling characteristics of TFLN devices, which provides a quick feedback on the poling fidelity and guides the optimization of the poling pulse.

Second-harmonic microscope imaging has been used to visualize domain structures in

thin-film and bulk LN [82, 83, 84, 72, 85, 86, 87]. The technique makes use of the fact that the SH generation observed in back-reflection (i.e., in the absence of any user-induced phase-matching) upon surface illumination using femtosecond optical pulses is highly sensitive to local changes in crystal structure and symmetry. While the technique is well understood in bulk LN, SH microscopy in thin films is influenced by interfacial reflections and resonant enhancements, which depend on film thicknesses and substrate materials. Here, we use a SH microscope to image the domains structures in TFLN, and investigate the imaging contrast mechanism on poled x-cut LN thin films.

3.3.1 Second-Harmonic Microscope Setup

The setup is shown in Fig. 3.2, in which a femtosecond Ti: Sapphire (95 MHz repetition rate, $<$ 100 fs pulse length, 25 mW focused power) operating at around 800 nm wavelength was focused, via an infinity corrected objective lens (50x Mitotuyo Plan Apo, infinity corrected, NA = 0.55; 100x Zeiss Epiplan-NEOFLUAR NA = 0.9), on the sample surface. Depending on the nonlinear properties in the focus region, second-harmonic light (around 400 nm wavelength) is generated, which was collected in back-scattering mode using the same objective. The reflected pump light was blocked by a dichroic beam-splitter and band-pass filters (Schott BG39). The filtered SH light was detected by a single-photon avalanche diode (MPD, PDM series) connected via a single-mode optical fiber with a 2.4 μm core diameter, which also served as the confocal pinhole. The optical system provides in vacuum a lateral resolution of about 400 nm and an axial (depth) resolution of about 2000 nm. It should be noted, that the depth resolution and to a lesser degree the lateral resolution deteriorates, when focusing into refracting media [88]. For our experiment this is of no concern, as these effects start to become noticeable, when focusing tens of microns below interfaces. However, in our experiment we are investigating the TFLN layer exposed at the surface, which in any case is thinner than the depth resolution. Due to the confocal configuration, scanning of the sample, rather than the beam, was performed in order to generate a

"map" of the domain structure. To achieve this, the sample was mounted on a 3-axis piezo-stage and scanned, whereas the optical beam maintained a fixed focus point. In order to create a typical 2D image, a selected region was scanned with 100 nm step width along the y and z axes of the TFLN, and 10 ms signal integration time per acquisition point. The step width is chosen to be smaller than the optical resolution to acquire an image with a resolution limited by the optical setup rather the step size.

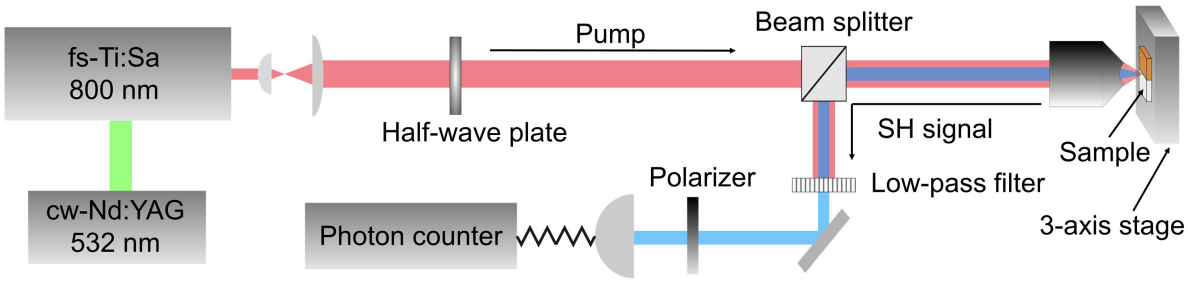

Figure 3.2: Schematic illustration of the SH microscopy setup.

3.3.2 Simulated Second-Harmonic Signatures

Figure 3.3(a) shows an as-measured second harmonic image taken around two electrode pairs after applying four consecutive poling pulses to a hybrid (bonded) Si-TFLN waveguide, as shown in Fig. 3.8(a). For comparison Fig. 3.3(b) shows a simplified sketch of this region highlighting the scan area in relation to main features. In this sketch, unpoled regions are colored in grey, while poled regions are colored in orange. As the sketch Fig. 3.3(b) suggests, the second harmonic image can be divided into three main sections: the electrodes, the unpoled, and the poled regions. Further, the Si waveguide is visible as a line with decreased, but nonzero intensity. For visibility it is highlighted by a red border. The electrodes, which are highlighted by yellow lines, provide no SH signal, as the metal is not transparent and has no $\chi^{(2)}$ nonlinearity at this wavelength. The unpoled regions of the TFLN provide a homogeneous SH signal level due to the intrinsic nonlinearity of LN. The poled regions feature the general trapezoid shape with a

broader base close to the positive electrodes as described above, but an additional substructure with broad dark areas surrounding bright areas is also observed. To understand these observations, the contrast mechanism in the system needs to be considered.

In general, the pump light will generate second harmonic generation in forward (FW), i.e. propagation in the same directions as the pump beam, or backward (BW) direction, as shown in Fig. 3.3(c). BW and FW generated SH light is characterized by different phase matching conditions and therefore coherence lengths for the SHG process (FW: $\Delta k = k_{SH} - 2k_f$; BW: $\Delta k = k_{SH} + 2k_f$ [84]). Taking the extraordinary refractive indices of lithium niobate at the pump and SH wavelength into account, this results in a coherence length of $l_{C,\,BW} \approx 44$ nm for BW scattering and $l_{C,\,FW} \approx 1275$ nm for FW scattering. If BW scattering is the only dominant process in SH microscopy of the TFLN, one will expect a dark contrast for two stacked domains of opposing direction almost independent of their relative thickness. This is similar to previous observations of stacked domains in a similar geometry, where reference beams [86] or reference samples [89] can be used to visualize domains or domain polarity, rather than domain walls. However, in the thin film geometry, the FW generated light will also be detected in the backward direction due to reflections at the LN/SiO_2 and SiO_2/Si interfaces. The SH intensity scales quadratically with the interaction length. The interaction length for FW generation is more than 10 times longer, than the coherence length of BW generation, and also is more than twice the thickness of the TFLN. Therefore the FW signal will be more than 2 orders of magnitude larger, compared to the BW generated SH light. Based on the refractive indices at 400 nm, the reflectivity at the interfaces can be estimated at 0.05 for the LN/SiO_2 interface, and up to 0.34 for the Si/SiO_2 interface, due to the high index of Si at 400 nm (up to 5.57) [90]. This presents an explanation for the large intensities, we observed in SH microscopy from the TFLN.

The importance of reflected signal from the bottom layer also can explain another observation in the data. Although the waveguide is below the layer, its presence is clearly visible by a drop in SH intensity in the scan, which can only be explained if light interaction with the layer

below the film contributes to the detected signal. Here, the only 320 nm wide waveguide will partly diffract, scatter and absorb the FW generated SH signal, leading to a reduction in intensity.

Table 3.1: Refractive indices of the materials used in SH signature simulation.

Wavelength	LN (n_e)	SiO_2	Si
800 (Pump)	2.1755	1.4533	3.6941 + 0.0065435i
400 nm (SH)	2.3321	1.4701	5.5674 + 0.38612i

The coherence length for FW generated light is longer than the TFLN thickness. Therefore, the FW generated light can coherently and continuously interact over the complete thickness of the film. For a growing domain with thickness d (Fig. 3.3(c)), a continuously decreasing signal with a minimum at about half the film thickness may be predicted. This is consistent with our observation of a gradual decrease and increase of signals in the regions which we suspect are only partially poled. It should be noted that the sensitivity for the inversion depth is purely dependent on the coherent nature of the nonlinear process, and is at first order not dependent on the diffraction limited depth resolution of the optical system.

To confirm this prediction, we have modeled the nonlinear response for a partially poled film in back-reflection based on a model and code developed by Sandkuijl et. al. [91]. Refractive indices used in the calculations are summarized in Table 3.1 [92, 93, 94, 95]. The model can describe the nonlinear response from an arbitrary $\chi^{(2)}$ distribution in the focal spot of a pump beam, using full three-dimensional vectorial calculations. The model also includes the effects of reflection, as well as includes reflection from planar interfaces for fundamental and SH light treated in a transfer matrix formalism. For more details on the code and calculation methodology, the original work by Sandkuijl et. al. [91] should be concerned. In our calculation we assume a numerical aperture of 0.55, illuminated with linear polarized plane waves. The polarization is aligned parallel to the z axis of LN and the focus is placed at the center of the LN layer. For

simplification the $\chi^{(2)}$ of LN is only represented by a single tensor element d_{33}, which is similar to our experiment. Due to the low order NA, the amount of non-x polarized components in the focus spot is minimal. The model includes a 600 nm film of lithium niobate on a 3.2 μm SiO_2 layer, with a silicon substrate, similar to our structure as shown in Fig. 3(a). The waveguide is currently not included in the model, as the calculation can only treat reflections between infinite interfaces orthogonal to the beam propagation. All materials are described with their respective refractive indices at the fundamental and SH wavelength (LN(e): $n_f = 2.1755$, $n_{SH} = 2.3321$; SiO_2: $n_f = 1.4533$, $n_{SH} = 1.4701$; Si: $n_f = 3.7$, $n_{SH} = 5.57$) [90, 94, 93]. In the simulation, the depth d of a domain with $-\chi^{(2)}$ is increased in 10 nm steps in the TFLN, as shown in Fig. 3.3(c), and the SH intensity collected by the objective in backscattering is calculated. The simulation result is normalized to the maximum intensity observed for a fully inverted ($x = 1$) or non-inverted ($x = 0$) domain. The result is depicted in Fig. 3.3(d) and shows a gradual decrease of the SH intensity to a minimum of 15% for a roughly 50% inverted film. The decrease is not symmetrical, which suggests a more complex interplay of reflections, resonant enhancements or phase matching. The weak oscillations, for example, are consistent with a period of about 90 nm hinting a BW phase-(mis)-matched process being responsible for parts of the signal.

The simulation suggests that SH microscopy may be able to detect the inversion depth non-destructively and with high resolution, i.e. line scans as displayed in Figs. 3.3(e) and (f), may be interpreted as partly inverted films as in Figs. 3.3(g) and (h). Detailed investigation of this process is reported in Ref. [96]. where extensive simulations confirm that generated SH signal from thin poled films allows to unambiguously distinguish areas, which are completely or only partly inverted in depth. In addition, effects of film thicknesses, handle materials and limits of this method were also discussed.

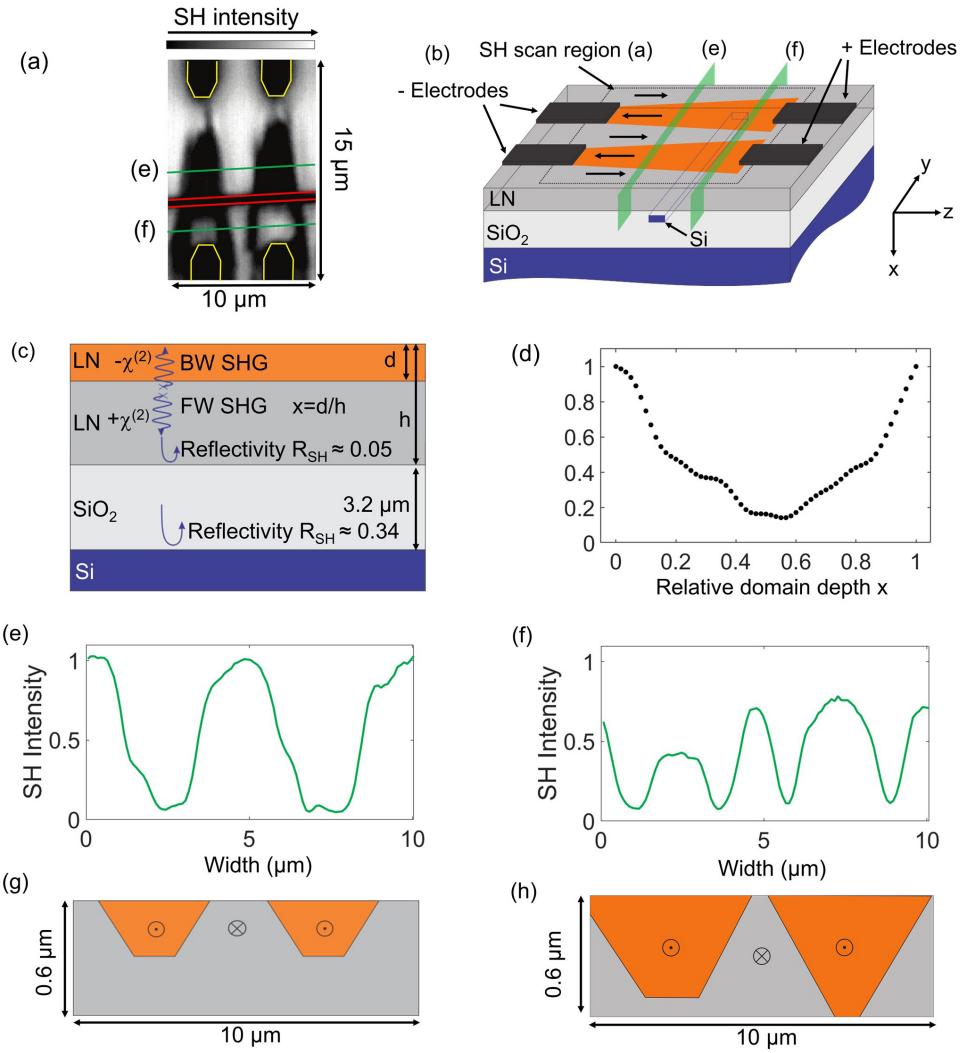

Figure 3.3: (a) Typical SH microscopy scan result of a poled sample. For clarity the waveguide and electrodes are highlighted in red and yellow, respectively. (b) Sketch of the imaging and domain geometry of the scanned region in (a). Poled regions are marked in orange, while unpoled lithium niobate is colored in gray. (c) Not-to-scale cross-section of the sample highlighting the involved processes, i.e. BW SHG, FW SHG and reflections at the interfaces. (d) Simulated SH signal for a varying relative domain depth x. (e)-(f) Line scans of the nonlinear signal taken along the lines highlighted in (a). (g)-(h) Sketches of the suggested depth profile of the domains estimated from the simulation results in (d).

3.4 Poling Monitoring

As is demonstrated in the previous section, SH microscopy provides information of the local texture, poling depth as well as uniformity of individual domain structures of the

TFLN. Except for SH microscopy, in-situ second harmonic generation (SHG) measurement has also been used to evaluate the poling fidelity [13], but it requires knowledge of the phase matching conditions before poling. Missey et al. [97] and Grilli et al. [98] have presented in-situ visualization of the domain formation process in bulk LN, while the demonstrated resolution was on the order of tens of microns. Karlsson et al. [99] developed a real-time poling monitoring technique, based on the electro-optic effect in ferroelectric crystals. This technique has been successfully demonstrated in the poling process of bulk KTP and RTP [99, 100, 101]. However, poling monitoring of TFLN has not yet been presented. Here we implement this technique in LN thin-films, and prove that it provides us the poling information path-averaged along the entire waveguide structure. This useful data may improve the tailored development of optimized poling recipes and result in improved device structures.

3.4.1 Concept

A schematic illustration of the fabricated device is shown in Fig. 3.4(a), with the stitched microscope images of a fabricated device shown in Fig. 3.4(b). The TFLN waveguides were fabricated using the oxide-bonding process we have previously described in detail for ultra-high RF frequency electro-optic modulators [61]. Two sets of electrodes, labeled poling and monitoring electrodes in Figs. 3.4(a) and (b), were fabricated by photolithography. In cross-section, the electrodes consist of a 10 nm Cr adhesion layer deposited on TFLN, followed by a 100 nm Au layer. For this study, we fabricated poling electrodes with a uniform 5 μm period, and with different duty cycles (the fraction of the period that is covered by Au) ranging from 25% to 50%. The separation gap between the two opposing electrode "teeth" facing each other [see inset of Fig. 3.4(b)] was defined by lithography to be 10 μm, based on an estimate of the critical field required for initiating poling (described further below). The center of the optical mode in the hybrid waveguide is placed closer to the positive poling electrodes, which allows the optical mode to see the most uniformly inverted region, based on insights in poling thin films [102]. Fig. 2

depicts the simulated electric field distribution in the poling region with 400 V applied to the monitoring electrodes. As shown in Fig. 3.5(b), the optical mode sees relatively uniform electric field in both the poled and unpoled area during the monitoring steps.

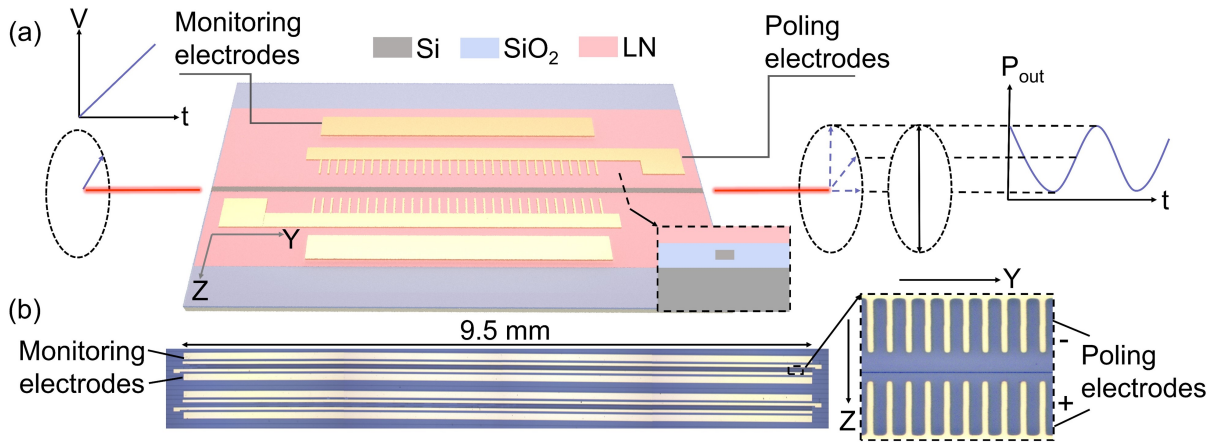

Figure 3.4: (a) Schematic illustration of the poling monitoring process. (b) Top-view optical micrograph of the fabricated chip, which includes hybrid Si-TFLN waveguides and two sets of poling and monitoring electrodes.

Hybrid Si-TFLN waveguides were used to couple light into and out of the chip. Continuous-wave laser light at 1550 nm wavelength, polarized at 45° to the x and z axes of the TFLN microchip (see Fig. 3.4), was launched along the y axis, through the hybrid Si-TFLN waveguides. Tapered lensed fibers were used to couple light to the chip. When a voltage was applied to the electrodes (inducing an electric field along the z axis), the electro-optic effect rotates the output state-of-polarization (SOP) of the transmitted light. We quantified the change in the SOP by transmitting the light through a fiber-coupled polarizer and measuring the power on a photodiode. The voltage (linear) ramp was synchronized to the photodiode readout, so that the resulting waveform could be observed and interpreted as an "oscillation" (or lack thereof) of the recorded output light power

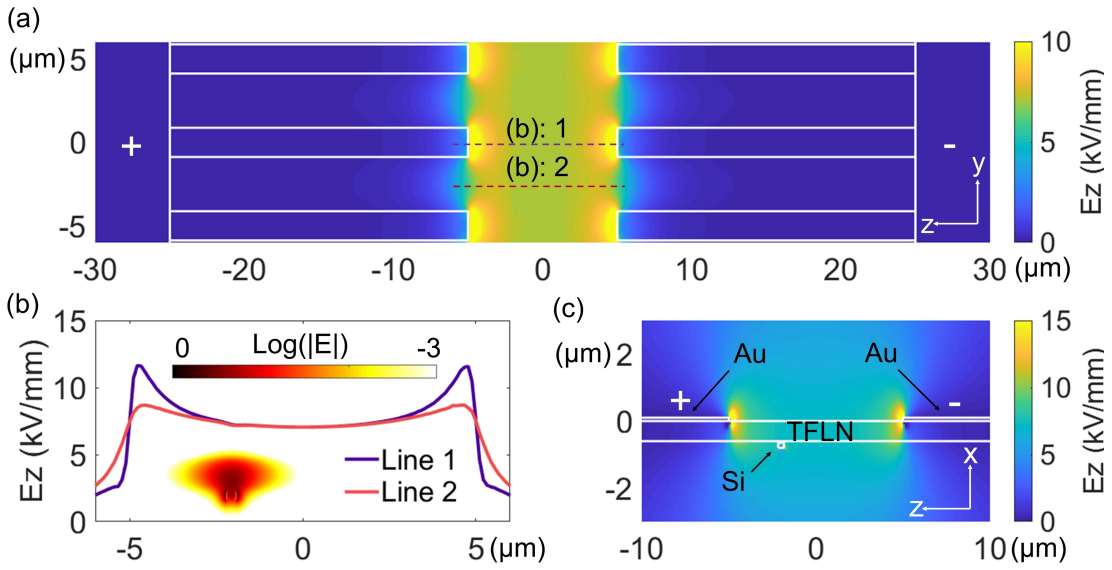

Figure 3.5: Numerically simulated electric field distributions (all shown in E_z component) with 400 V applied to the monitoring electrodes (not shown here). (a) E_z distribution in the y-z plane, at a slice through the middle of the TFLN region. (b) E_z variation in the z direction along the two dashed lines shown in (a). Simulated E field intensity of the fundamental TE optical mode is overlaid in the plot, which shows the electrical field distribution seen by the optical mode. (c) E_z distribution in the x-z plane.

(P_{out}) versus (probe) voltage.

Analytically, P_{out} depends on the total phase retardation between the x and z components of the light (Γ), and can be expressed as [100]:

$$P_{\text{out}} \propto (1-\cos\Gamma), \tag{3.1}$$

where, in bulk LN, Γ is described by [100]:

$$\begin{aligned}\Gamma &= \frac{2\pi}{\lambda}(n_z-n_x)L+\frac{2\pi}{\lambda}E_z\left[\left(\frac{n_x^3}{2}r_{13}-\frac{n_z^3}{2}r_{33}\right)(L-x)-\left(\frac{n_x^3}{2}r_{13}-\frac{n_z^3}{2}r_{33}\right)x\right]\\ &= \frac{2\pi}{\lambda}(n_z-n_x)L+\frac{2\pi}{\lambda}E_z\left(\frac{n_x^3}{2}r_{13}-\frac{n_z^3}{2}r_{33}\right)(L-2x).\end{aligned} \tag{3.2}$$

E_z is the magnitude of the electric field applied for monitoring in the z direction, L is the total

length of the poling region, x is the length of the inverted domains, $n_{\{x,\,z\}}$ is the refractive index in the x or z polarized direction, r_{13} and r_{33} are the electro-optic coefficients of LN, and λ is the wavelength of the input light. The poling duty cycle (ξ) is defined as $\xi = x/L \times 100\%$.

The physics of Eq. (3.2) describes the differential phase accumulation between the two interfering field components, which translate, in the context of TFLN waveguides, to the (quasi-) TE and TM polarized lowest-order modes. Thus, in our experiment,

$$\Gamma = \frac{2\pi}{\lambda}(n_{\text{eff}}^{\text{TE}} - n_{\text{eff}}^{\text{TM}})L + \frac{2\pi}{\lambda}\left\{\left[\Delta n_{\text{eff}}^{\text{TE}}(E_z) - \Delta n_{\text{eff}}^{\text{TM}}(E_z)\right](L-x) + \left[\Delta n_{\text{eff}}^{\text{TE}}(-E_z) - \Delta n_{\text{eff}}^{\text{TM}}(-E_z)\right]x\right\}, \tag{3.3}$$

where $\Delta n_{\text{eff}}^{\{\text{TE, TM}\}}(\{E_z,\ -E_z\})$ is the fundamental TE or TM mode index change in the unpoled or poled region, respectively. Note that, here, the sign reversal of the electric field is equivalent to that of r_{13} or r_{33}, because $\Delta n_{\text{LN}}^{\{\text{TE, TM}\}}(E_z) = -1/2 n_{\{z,\,x\}}^3 r_{\{33,\,13\}} E_z$, for the TE and TM polarizations, respectively.

In the case of unpoled bulk LN ($x = 0$), as one applies a linearly-increasing E field, i.e., a voltage ramp, the measured P_{out} would behave as $1 - \cos\{\Gamma' + \Gamma[E_z(t)]\}$, where Γ' and $\Gamma[E_z(t)]$ are the phase differences caused by the modal dispersion and the electro-optic effect, respectively. During poling, the oscillation gradually disappears as ξ increases from 0 up to 50%, and then appears again as the poling duty cycle increases further. This is because the phase retardation in the inverted and uninverted domains will be mutually cancelled out if $L = 2x$ (i.e., duty cycle = 50%), which results in $\Gamma[E_z(t)] = 0$.

In the hybrid Si-TFLN waveguides, $\Delta n_{\text{eff}}^{\{\text{TE, TM}\}}(E_z) \neq -1/2 n_{\{z,\,x\}}^3 r_{\{33,\,13\}} E_z$. Therefore, we used a finite-difference eigenmode solver to simulate the waveguide cross-section and calculate the effective indices. Figure 3.6(a) depicts the cross section of the hybrid Si-TFLN waveguide used in the simulations. The axial components of the calculated Poynting vector (i.e., along the propagation direction) for the fundamental (quasi-) TE and TM lowest-order modes are shown in Fig. 3.6(b). The hybrid waveguides are designed so that the optical mode is laterally confined in

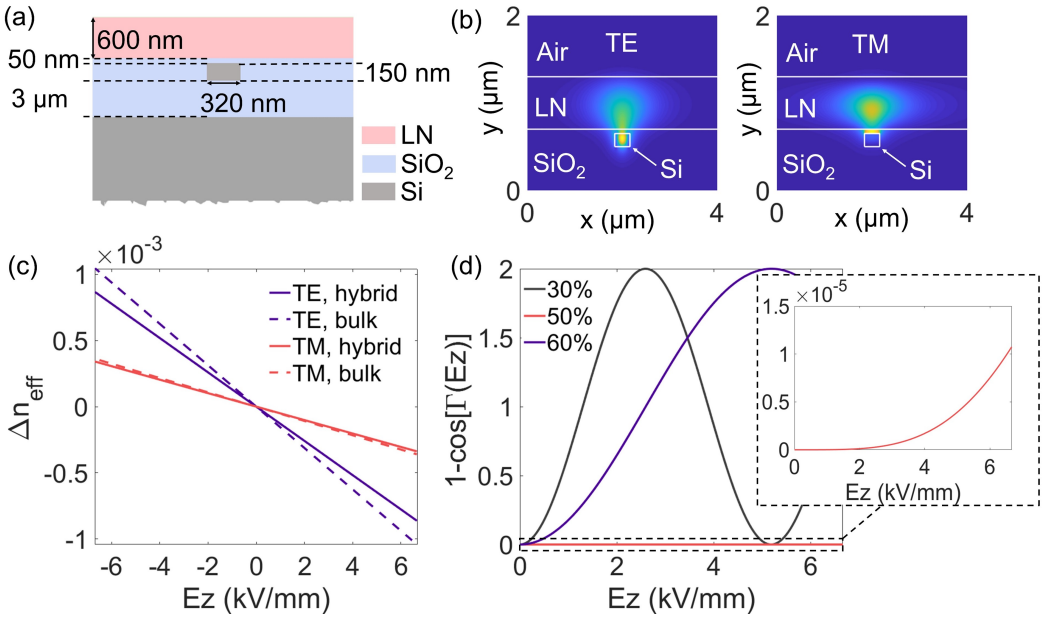

Figure 3.6: (a) Schematic cross section of the hybrid Si-TFLN waveguide. (b) Simulated TE and TM mode Poynting vector components along the direction of propagation at 1550 nm. (c) Calculated TE and TM mode refractive index variation as a function of the applied electric field in hybrid Si-TFLN waveguides (solid line) and bulk LN (dashed line). (d) Calculated 1-cos[$\Gamma(E_z)$] as a function of the applied electric field with different poling duty cycles.

the Si waveguide while most (75% and 85% for TE and TM mode, respectively) of the power resides in the LN region. Such a structure provides a nearly linear relationship between the mode refractive index variation and the applied electric field in the hybrid Si-TFLN waveguide, which is very similar to that of the bulk LN [see Fig. 3.6(c)]. Therefore, when exactly half of the sample is poled, we expect that the measured monitoring signal will be almost flat as a function of the monitoring voltage, the same behavior as seen in bulk LN [see Fig. 3.6(d)]. The slight nonlinearity of Δn_{eff} with respect to E_z in Fig. 3.6(c) is because the portion of light confined in the LN region, relative to the surrounding materials, changes with the applied voltage. However, this effect is minor, and the trend shown in Fig. 3.6(c) appears linear, for all practical purposes.

3.4.2 Bonded TFLN Poling and Monitoring

The voltages required for poling TFLN are generally less than 1 kV, which is much smaller than for poling conventional LN waveguides. No special holder was required; however the device was poled with transformer oil surrounding the probe-pad contact point and the immediate vicinity of the electrodes along the entire length of the waveguide, which helped prevent arcing and electrode breakdown. We applied a sequence of 500 V or 600 V pulses to the poling (electrical) circuit using a high voltage amplifier (HVA) as shown in Fig. 3.7(a). We choose a commonly-used poling voltage waveform [see Fig. 3.8(a)], i.e., a rapid ramp-up of the poling voltage to a value higher than voltage required to exceed the coercive field strength (here, calculated to be about 210 V), which initiates the generation of nucleation sites, followed by a slow ramp-down of the poling voltage, which stabilizes the newly-formed domains (in analogy with the known mechanisms in bulk LN [75]).

The optical monitoring technique was included as part of the poling setup, as shown in Fig. 3.7(a), which allows diagnostics of poling without removing the chip from the setup. (In these experiments, however, the chip was removed and replaced, in order to perform microscopic imaging of the domain walls using second-harmonic microscopy. Exact re-positioning of the sample was not achieved, resulting in some mis-alignment in the visual appearance of successive traces, as evident in the figures. These do not significantly affect either the results or the interpretation.)

A linearly-increasing voltage waveform i.e., a ramp, with a minimum at 0 V and a maximum at 400 V over 50 s was applied to the monitoring electrodes, and the output light power was recorded by a multimeter. Traces were recorded before poling was initiated, and were also recorded after each poling pulse. By comparing the magnitude and number of oscillations in the measured monitoring signals, we can infer how much of the LN has been poled; the oscillations (as a function of probe voltage) are expected to nearly completely disappear when exactly one-half of the LN is poled, and are expected to be clearly evident both for under-poling

and for over-poling.

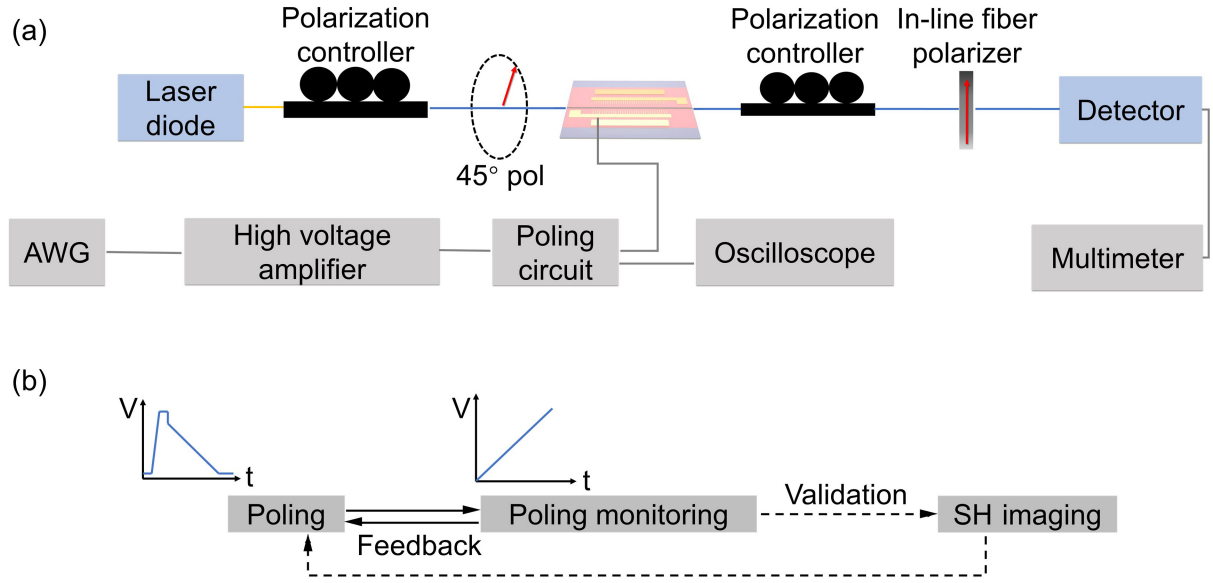

Figure 3.7: Schematic illustration of poling and poling monitoring setup (a) and the measurement process (b).

3.4.3 Results and Discussion

The measured poling voltage and current waveforms are shown in Fig. 3.8(a), the optical monitoring signals are shown in Fig. 3.8(b) and the domain-wall images using SH microscopy are shown in Fig. 3.8(c), after a certain number of poling pulses were applied. For these measurements, the length of the poling electrode was $L = 0.95$ cm, with 5 μm period and 35% duty cycle. Four 500 V and twelve 600 V pulses were applied to this sample in total. In these experiments, the chip was removed and replaced, in order to image the gradual growth of the inverted domains after each poling pulse, while the scanned area was kept the same. Exact re-positioning of the sample was not achieved, resulting in some mis-alignment in the visual appearance of successive traces, as evident in Fig. 3.8(c). These do not significantly affect either the results or the interpretation. However, not all the applied pulses made notable contributions to the poling process, which will be explained further below. The TFLN used in this experiment was commercially acquired

(NanoLN, Jinan Jingzheng Electronics Co., Ltd.) and is single-domain film before poling.

As shown in Fig. 3.8(a), a large current spike was measured during the first voltage pulse, which suggests most of the nucleation cites have been generated near the electrode that carries the positive charge. The recorded monitoring signal (Fig. 3.8(b), solid red line) shows fewer oscillations compared to what was measured before poling (Fig. 3.8(b), solid purple line). This suggests that some of the domains have propagated, upon application of the poling pulses, to the physical region of the LN film where the optical mode sits. This agrees well with the SH images shown in Fig. 3.8(c), where red and yellow solid lines were added manually to outline the Si waveguides and the poling electrodes respectively.

After the fourth poling pulse, the oscillations in the monitoring signal further decrease, which suggests that the poled area grew more into a region shared with the optical mode; this is confirmed by the SH image. We observed a decrease in the poling voltage on the sample after the first poling pulse, when keeping the output voltage from the high-voltage amplifier constant at 500 V. This may be because the generation of domain walls may have increased the conductivity of the TFLN [103, 104]. This may also explain why we did not observe a noticeable domain growth in the z direction until we increased the poling voltage from 500 V up to 600 V. Oscillations in the monitoring signal almost disappeared after the sixth poling pulse, which indicates the desired end-point of the poling process at which about one-half of the LN region, as sampled by the guided optical mode itself, has been poled. Note that this does not mean that the poling duty cycle is 50% everywhere, and indeed, the SH image of a certain portion of the waveguide shows that the area near the positive electrodes is slightly overpoled, while the other side stays underpoled. For this experiment, we proceeded to pole further, and as expected, the oscillations are once again clearly measured. This demonstrates the usefulness of the optical monitoring method in non-destructively measuring the poling characteristics of TFLN waveguides.

Here, to better evaluate the consistency of the two methods, we extract the poling duty

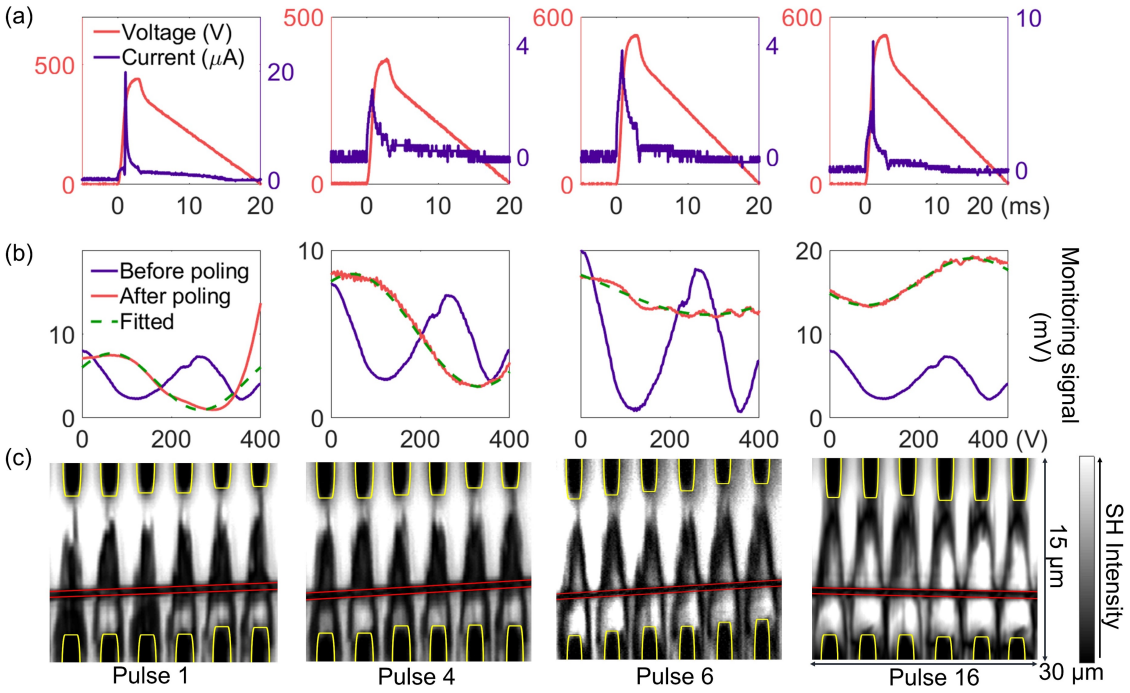

Figure 3.8: (a) Measured poling voltage and current waveforms. (b) Recorded poling monitoring signals. (c) Second-harmonic confocal microscope images, after the indicated number of poling pulses were applied.

cycle (ξ) by fitting the measured monitoring signals, based on the following equation:

$$P_{\text{out}} = A \times (1 - \cos[\Delta\phi_{\text{in}}(\xi_{\text{m}}) + \Delta\phi(\xi_{\text{m}}) + \theta]) + C. \tag{3.4}$$

P_{out} is the recorded monitoring data, $\Delta\phi_{\text{in}}(\xi_{\text{m}})$ and $\Delta\phi(\xi_{\text{m}})$ are the phase differences between the TE and TM mode in the inverted and uninverted regions, assuming the poling duty cycle is ξ_{m}, which are calculated based on the simulation results from Eq. (3.3). The fitting parameters are A, θ, ξ_{m} and C. Note that to extract these parameters, we also need to know the actual electric field (E_{R}) in the monitoring region. Here, E_{R} was calculated by fitting the recorded monitoring signal before poling. A good agreement is obtained by setting $E_{\text{R}} = 3.5$ kV/mm in contrast with the simulated value $E_z \approx 7.2$ kV/mm [see Fig. 2(b)]. This discrepancy may come from the differences in the actual waveguide structure and material properties compared to the assumptions made in the simulation, which did not take into account finite conductivity of the electrodes, imperfect

contacts, or other sources of the voltage loss. In addition, 400 V was the output voltage from the HVA, the voltage applied on the sample is approximately 350 V. For the four poling pulses shown in Fig. 3.8, the predicted poling duty cycles are 20%, 29%, 64% and 75%. Substituting these parameters in Eq. (3.4), we were able to reproduce the measured monitoring signal after each poling pulse (Fig. 3.8(b), dashed green lines).

In agreement with the monitoring data, the nonlinear images in Fig. 3.8(c) show a gradual increase of the poled area after each pulse. A particular large increase can be seen at pulse 6 compared to the previous images, as the voltage was increased. Assuming this local SH image is representative of the complete device, the images can be used to estimate the poling duty cycles. We numerically define and calculate the poling duty cycles based on the SH images as

$$\xi_{\mathrm{SH}} = \frac{A_{\mathrm{O}} \cap A_{\mathrm{in}}}{A_{\mathrm{O}}} \times 100\%. \tag{3.5}$$

A_{O} is the area where the optical mode sits; this area was defined here as the geometrical rectangle that extends ± 2 μm from the center of the Si waveguide. A_{in} is the area that represents the inverted region, which is the area outlined by the boundaries of the inverted domains as identified by SH microscopy. This formula itself can provide an estimation of the duty cycle, if an area (that overlaps with the optical mode) is completely inverted, i.e., the measured SH signal level is similar to the unpoled regions, and a thin boundary to an uninverted region is observed. Note that, as is mentioned above, the prerequisite for applying Eq. (5) to the measured SH images is that the local SH image is representative of the entire structure, i.e., the uniformity of the poled regions is fairly good along the y axis of the TFLN. In our experiment, these conditions are satisfied only after the sixth voltage pulse, where all depicted inverted regions in the image show a comparable width and general appearance. In contrast to this, for the preceding pulses each inverted region has a unique shape, width and appearance, rather than a similar shape. For example after the first pulse, some areas around the waveguide have already been completely inverted as shown by the SH images, while other areas are only partly inverted and to a varying

degree. Therefore, for the pulses before the sixth pulse, we can only estimate an effective duty cycle of less than 50% as an upper boundary, which is in agreement with our observations from the monitoring signals. The interpretation of the SH contrast mechanism, as explained in Sec. 3.2., suggests that it may be possible to extract an approximate depth of the inverted domain from the signal decrease of the SH signal level. This mechanism, combined with optimized poling recipe (better poling uniformity), might allow us to estimate an effective duty cycle for partly inverted structures. However, further investigations are necessary to understand the detailed mechanisms and influence of different parameters, such as the signal decrease due to the waveguide or oxide and TFLN thicknesses, which is beyond the scope of this work.

The SH images indicate the inhomogeneity of the inverted domains along the z axis. To improve the poling process further, there are a number of steps that could be taken. We conjecture that poling homogeneity in the z direction can be improved by using a thin insulation layer to prevent domain spreading in the y direction [105]. Narrower poling electrodes, with a smaller duty cycle, in combination with shorter and higher poling pulses may also help in achieving uniform poling.

Figure 3.9 compares the ξ_m values with the calculated ξ_{SH} values, where ξ_m shows a clear transition from under-poling to over-poling. Despite the small areas of the SH scans, the results from the two methods are in agreement with each other, which indicates a comparable domain structure over the complete sample. SH images were not recorded after the eighth, nineth, or eleventh through fifteenth voltage pulses, because these pulses were applied consecutively, without stopping the experiment to remove and measure the microchip in the SH setup as previously observed changes were only minor. All the corresponding SH images are presented in the Appendix.

In this section, we showed gradual poling of bonded hybrid TFLN waveguides using a series of voltage pulses between 500 V and 600 V, and we developed and demonstrated an electro-optical monitoring technique for suggesting the ideal end-point of the poling process,

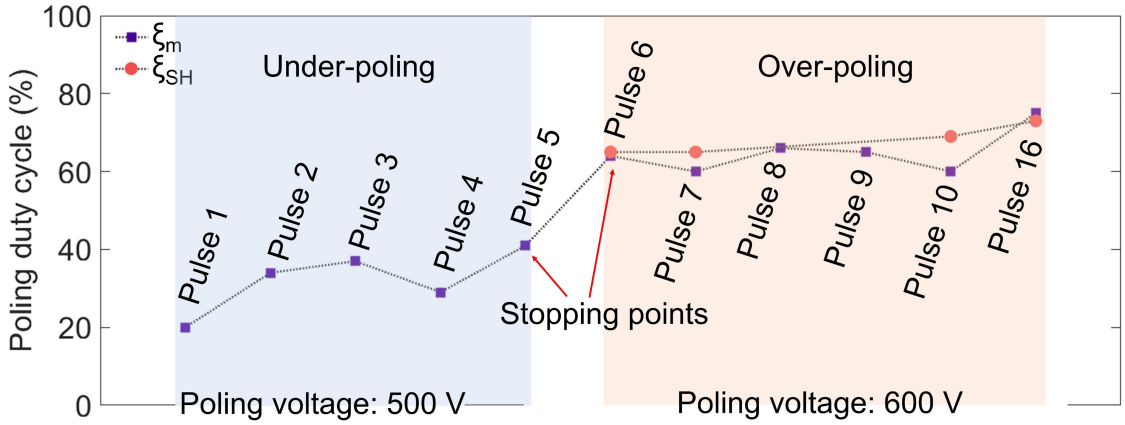

Figure 3.9: Comparison of the predicted poling duty cycles (ξ_m) inferred from the recorded monitoring signals, and the calculated poling duty cycles (ξ_{SH}) based on the measured SH images.

i.e., how many voltage pulses should be applied. Here, the predictions of the optical monitoring technique were validated by the second-harmonic images. This technique, combined with second harmonic microscopy can provide us both local and global information of the poling results, and thus yield useful data that may improve the tailored development of optimized poling recipes and improved device structures. This technique can also be used together with conventional monitoring techniques such as readout of the voltage and current characteristics, and second harmonic generation measurements. Additionally, in contrast with HF-etching based diagnostics, all of these methods are non-destructive. We believe the techniques and results presented here will benefit and accelerate the development of integrated quasi-phase-matched structures in integrated photonics incorporating thin-film lithium niobate.

3.5 Poling Waveform Optimization

In the previous sections, we have shown two different poling diagnostic methods, and demonstrated their potential provide guidance and feedbacks for poling pulse optimization. Optimal poling waveform is the key to achieve high-fidelity poling, i.e., to fabricate uniformly

inverted domains with 50% duty cycle. As a starting point for the subsequent optimization, a standard poling voltage waveform was chosen here, i.e., an initial rapid ramp-up of the voltage to initiate the generation of nucleation sites, a hold of the voltage above the coercive field strength for about 1 ms, and then a slow ramp- down of the voltage to stabilize the newly formed domains, as is shown in Fig. 3.10. Specifically, we investigate poling of 5 mol% magnesium oxide (MgO) doped, 300-nm thick x-cut lithium niobate on insulator (LNOI), as is used for device demonstration, which will be discussed in the following chapters. In our experiments, we use one single high voltage pulse for poling, with the poling gap fixed at 20 μm. Note that it is by no means the only combination to achieve successful poling, and high-fidelity poling with multiple pulses and different gaps have been shown in other publications [10, 13, 105, 106].

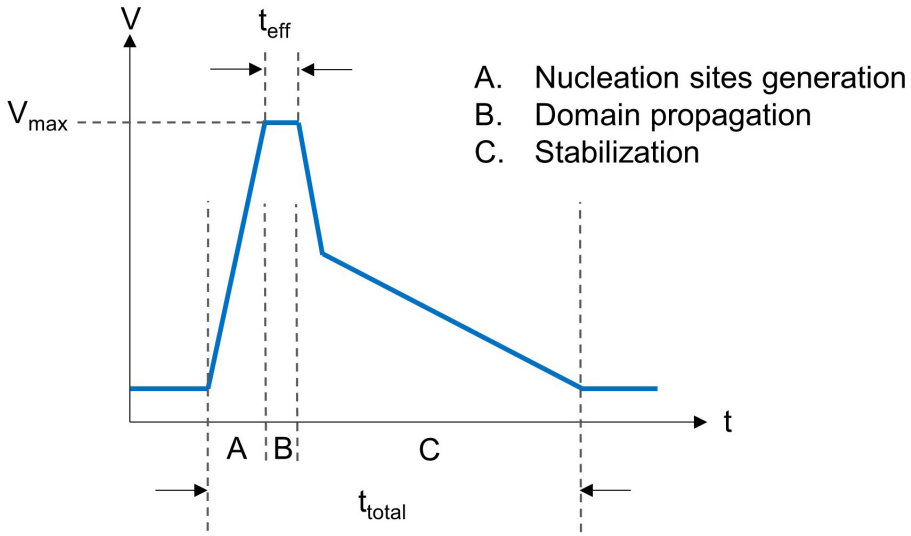

Figure 3.10: Sketch for the poling waveform used in this experiment.

3.5.1 Simulated Second-Harmonic Signatures

As we have demonstrated in previous sections, SH microscopy is sensitive to the depth of an inverted domain [107]. This can be easily understood if two domains of different orientation are stacked vertically, the SH signal generated in each of these vertically stacked domains will

destructively interfere, leading to a decrease in the generated SH signal compared to that from a completely inverted or unpoled region. In a fully inverted domain, only the dark lines belonging to the domain transitions are expected to be seen. To show the contrast mechanism of SH microscopy, we have modeled the nonlinear response for a partially poled film in back-reflection based on a model and code developed by Sandkuijl *et al.* [91], which was adapted and applied to the LNOI geometry considered here. The simulated SH signatures of different domain structures are shown in Fig. 3.15. Note that only vertical or horizontal domain walls are considered here (300-nm thick x-cut LNOI). Discussions about more complex domain geometries, e.g. angled structures or hexagonal cross sections, can be found in Ref. [47]. As shown in Fig. 3.15(a), when simulating the SH response across a single, vertical domain wall, a drop in the SH signal is observed, as the generated SH light in the inverted region interferes destructively with that in the uninverted region. To achieve high nonlinear conversion efficiency, the poled domains have to penetrate the complete film thickness. To consider this, we have simulated the SH response from a thin film with a horizontal domain transition with growing domain penetration depth h_{DW}. In this case, a continuously decreasing signal with a minimum at about half the film thickness is predicted, as the forward generated SH light coherently and continuously interacts over the complete film thickness. The decrease is not symmetrical though, which is due to the interplay of reflections, resonances and phase matching, and this has been discussed in detail in Ref. [47].

3.5.2 Challenges

Figure 3.12 summaries SH images of samples with different poling conditions. Figure 3.12(a) is an SH image generated from an unpoled area. As is consistent with the previous simulations, we measured uniform SH signals in the un-inverted poling region. In this figure, poling electrodes are visible as dark stripes and rectangles at the top and bottom of the image because the electrode material (gold) features no second order nonlinearity in the optical band. Figures 3.12(c) and (d) present measured SH images from under-poled regions, meaning either not

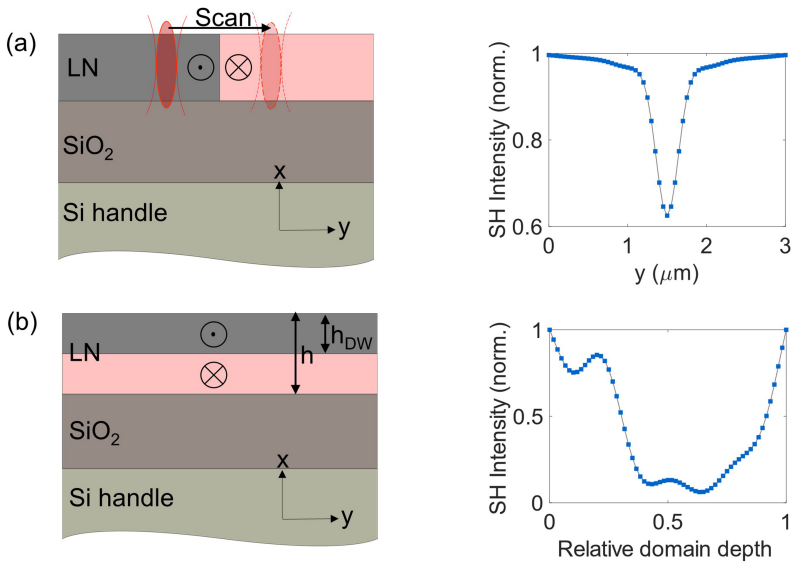

Figure 3.11: (a) Simulated SH signature of a single, vertical domain wall. (b) Evolution of the SH response from a domain with varying thickness h_{DW}. Relative domain depth is defined as h_{DW}/h.

all the domains are inverted, or the width of inverted domain is too narrow (narrower than half of the poling period). In these figures, the domain walls (DWs) appear as dark lines stretching from the positive to the negative electrodes and the bright regions surrounded by the DWs correspond to the inverted regions. Under-poling is often either caused by low V_{max}, or short t_{eff}. On the contrary, the sample will be over-poled [see Figs. 3.12(e)-(f)], meaning width of the inverted domain is wider than half of the poling period, and adjacent can even merge together, if the applied pulse is higher or longer than the optimal value. As has been mentioned in Sec. 3.2, newly-inverted domains are quite unstable, the poling voltage should be ramped down slowly, otherwise the newly-formed domains will flip back and causes back-poling, shown as the dark lines in the inverted domains in Fig. 3.12(b).

3.5.3 Optimal Poling Results

Through extensive experiments, it has been proven that poling of LN can be affected by various factors. For example, the poling electrode material has been shown to have a large effect

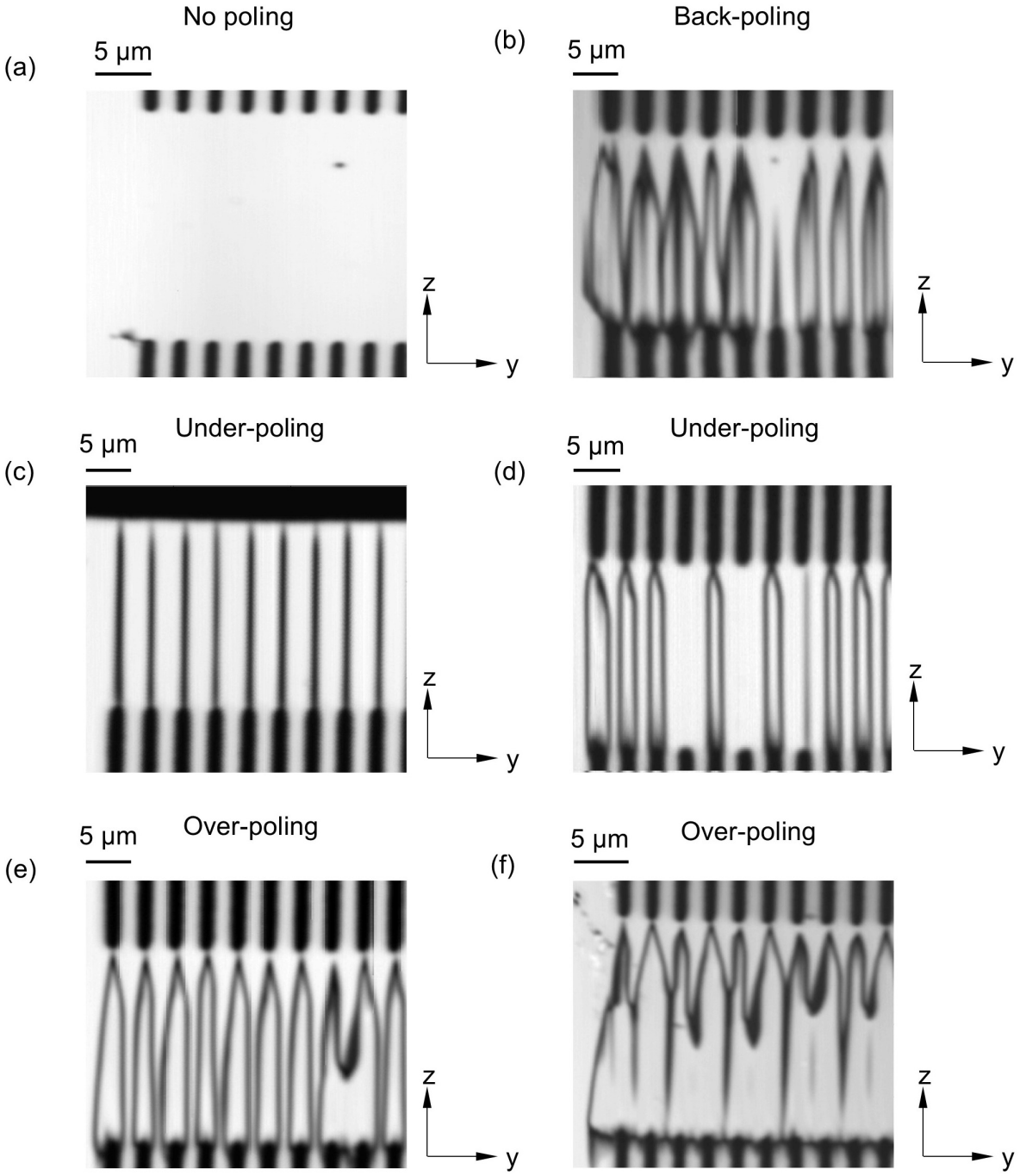

Figure 3.12: Measured SH images over non-poled (a), back-poled (b), under-poled (c)-(d) and over-poled (e)-(f) areas.

on nucleation site density, and sputtered nichrome was found to produce the most nuclei per unit area compared to other material, e.g., evaporated aluminum, sputtered chrome, etc. [75]. Shape

of the poling electrode could influence the domain growth, and tapered finger electrodes were found to be more appropriate than the standard rectangular finger electrodes to achieve more uniform domain structures. According to Ref. [108], for domain structures written by SPM tips, both the temperature and environment humidity could modify the created domain patterns. In our experiment, we observed a clear correlation between duty cycles of the fabricated domain grid and the poling electrodes. For the optimization process, we used gold electrodes (with a thin chrome adhesion layer), with a standard rectangular shape (the actual fabricated electrode finger was rounded), and the duty cycle was fixed at 35%. All samples were poled at room temperature, in open air, without active control of environment temperature and humidity. We mainly investigated influence of the poling waveform on poling fidelity.

To achieve optimal poling, for each poling period, multiple electrodes were fabricated to optimize the poling waveform. The most critical parameters found in our experiments are the pulse height (V_{max}) and the effective pulse length (t_{eff}), or the time duration of the stabilization phase, as is shown in Fig. 3.10. In this experiment, the pulse height was adjusted iteratively with a step of 5 V, and the effective pulse length was optimized with a step of 0.1 ms and less with the total pulse length (t_{total}) fixed at 30 ms. Through trials and errors, ideal poling is achieved and the corresponding SH image is shown in Fig. 3.13. In our experiment, the optimal V_{max} varies in the range of 830 V – 850 V, and t_{eff} is around 2 ms. Uniform domains with nearly 50% duty cycle were fabricated. In addition, the measured SH intensity in the inverted and un-poled region are almost the same, indicating not just surface domains but domains inverted toward almost the complete film thickness.

It was observed that the poled domain tapers down over several micrometers toward the negative electrode and only a tip of the domain reaches the electrode. This can be interpreted that the poled domain avoids forming highly charged head-to-head domain walls. However, head-to-head and tail-to-tail domain walls have been observed in bulk LN before [109]. The behavior close to the positive electrode is less clear. Therefore, further investigations are necessary

to thoroughly understand the domain growth and charge transfer dynamics in x-cut LN poled from top electrodes.

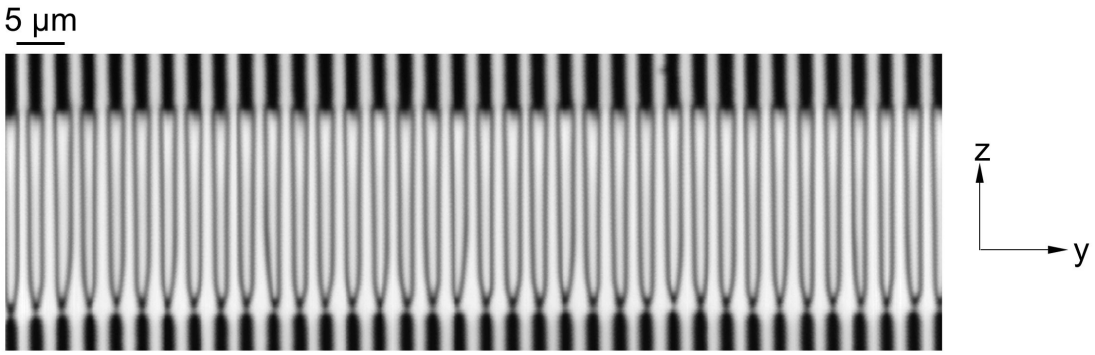

Figure 3.13: Measured SH image from a sample with ideal poling.

3.6 Poling with Sub-Micrometer Periodicity

The ability to achieve QPM between counter-propagating waves is essential to the realization of a mirrorless optical parametric oscillator (OPO), as has been demonstrated in periodically-poled $KTiOPO_4$ (PPKTP) [110], but not yet in periodically-poled lithium niobate (PPLN). In fact, a poling period (Λ) of 600 nm or less has been calculated for first-order phase matching in bulk PPLN waveguides [111]; the fabrication of homogeneous periodic domain structures with such deeply-sub-micron periodicities that penetrate across the complete waveguide modal area has not yet been achieved.

In LN, poling is most commonly achieved by the application of a strong electric field along the ferroelectric z axis of the crystal. During the electric field poling process, new domains nucleate at the poling electrodes and predominantly grow along the z axis (forward growth), while at the same time spread laterally. While sub-micron domain periods have been achieved in bulk LN with this method, the depth of these domain structures are shallow when compared to the usual depth of waveguides formed in bulk LN (5-10 μm) [112, 113, 114]. Furthermore, achieving sub-micron QPM periods in bulk LN often requires sophisticated fabrication protocols [115], while for

larger periods standard lithography process is appropriate. The realization of domain structures with sub-micron periodicity which is shown in LN is also achievable in KTP [116, 117, 118, 119].

Depending on the wavelength of interest, LN has higher nonlinear optical coefficients [37] and is available in larger wafer sizes (up to 6 inches) which may benefit the development of practical photonic devices. Moreover, LN is of considerable interest for device development because it is also widely used for optical modulators, acoustic wave filters, and memory devices [120, 121, 122, 123, 124]. Over the last decade, single crystalline thin films of LN (TFLN) have become available on common handle wafers (quartz, silicon or lithium niobate). The small thickness and the high index contrast of LN on an oxide buffer layer enable the formation of waveguides with sub-wavelength modal area and tight bending radius, compared to the traditional Ti in-diffused or proton exchanged waveguides in bulk LN. Such waveguides can support modes with similar cross-sectional profiles at widely separated wavelengths, which results in a highly efficient wavelength conversion device [125, 9, 13, 10, 126, 127]. For periodic poling of z-cut TFLN, the thin-film structure promises much smaller domain periods, since the inverted domains might have a width as small as the film thickness, which is similar to the penetration depth of typical sub-micron domain structures that have been formed in bulk LN [112, 113, 114]. However, poling z-cut TFLN often requires buried electrodes [70], which is not favorable for low-loss optical waveguide applications due to the resulting presence of buried metal electrodes in the vicinity of the optical mode. Alternatively, the poling ground electrode can be formed at the backside of the chip handle, yet elevated poling temperature is needed to reduce the coercive field of LN and thus the poling voltage [15]. In contrast, x-cut (and y-cut) TFLN can be poled easily at room temperature using surface electrodes which can be removed after poling [72]. The electrodes can also be retained, if placed at a sufficient distance away from the waveguide region. Nevertheless, sub-micron poling of x-cut TFLN remains challenging at the present time, since narrow domains will spread and may merge before being completely inverted in depth.

3.6.1 Method

Again, based on the type of wafer that is useful for optical waveguide devices [128], we studied poling of 5 mol% magnesium oxide (MgO) doped, x-cut lithium niobate on insulator (LNOI), acquired from NanoLN (Jinan Jingzheng Electronics Co., Ltd.). The material stack for the LNOI chip is shown in Fig. 3.14(a), which consists of a 300 nm-thick top functional layer (TFLN) and a 1.8 μm-thick buried oxide layer on a silicon handle. Test structures were fabricated with poling electrodes of 50 μm length and various periods ranging from 2 μm down to 600 nm [see Fig. 3.14(b)]. The separation gap between the two opposing electrode "teeth" facing each other was designed to be 20 μm, based on an estimate of the critical field required for initiating poling. The duty cycle of the patterned electrodes was fixed at 20%, to pre-compensate for the lateral spreading of the inverted domains; thus, photolithography provides insufficient resolution for defining the electrode structure accurately. On the other hand, electron-beam lithography alone is a relatively slow and serial-write process, not well suited to write large contact pads and long electrode structures that will eventually be needed. Thus, we developed a two-step lithography process using both photolithography and e-beam lithography. The latter was used first, to define the poling electrode "teeth" with high resolution, followed by the metal deposition (15 nm Cr/80 nm Au, deposited by electron-beam evaporation) and lift-off process. The probe contact pads were then aligned and structured by photolithography, together with a second metallization step and lift-off process. In cross-section, the contact pads consist of a 15 nm Cr adhesion layer and a 300 nm Au layer. As an example, the inset of Fig. 3.14(b) shows the microscope image of a set of fabricated poling electrodes with a period of 800 nm. A schematic illustration of the sample geometry is shown in Fig. 3.14(a). It should be noted that only the positive electrodes have been structured periodically, while the negative counter electrode is represented by a flat rectangle with no "teeth". During our experiments we found no significant differences when using either a flat or a structured ground electrode. Poling was performed by applying a single voltage pulse, with transformer oil surrounding the probe-pad contact point and the immediate vicinity of the

electrodes, which helped prevent arcing and breakdown. The poling pulse waveform, i.e., the length of the pulse or stabilization phase and the pulse height, was iteratively optimized for each period by imaging and re-poling. Details about the poling setup as well as waveform optimization have been discussed in the previous section.

3.6.2 Simulated Second-Harmonic Signatures

As we have demonstrated in previous sections, SH microscopy is sensitive to the depth of an inverted domain [107]. Although in SH images for structures with sub-micrometer periods, a periodic pattern can still be seen, the diffraction-limited resolution of SH microscopy ($\approx$ 310 nm for 800 nm pump wavelength and a numerical aperture of 0.9) masks further details of the poled domain structures. In this section, we have investigate domain structures with poling periods smaller than 1 μm. To determine the influence of optical resolution on the expected signatures, we have simulated the SH signals when scanning across domains of different width as shown in Figs. 3.15(a) and (b). For a domain width of 1 μm, which corresponds to a poling period of 2 μm, the simulated SH signal reaches minimum at the domain walls and recovers back close to 1 in the fully inverted (in depth) region. This is consistent with the simulation results shown in Figs. 3.11(a) and (b). Figure 3.15(b) shows results for a 500 nm-wide domain. Due to the diffraction-limited resolution of SH microscopy ($\approx$ 310 nm for 800 nm pump wavelength and a numerical aperture of 0.9), the two adjacent valleys in the SH signal at the domain walls overlap with each other and thus even though the domain is inverted fully in depth, the simulated SH intensity will not recover to 1 in between the two domain walls. Therefore, in this case we can not get detailed depth information of the inverted domains based on the SH images. In our experiment, the structures with periods of 1 μm and less have been analyzed with PFM. The PFM measurement was performed using a Cypher AFM (Asylum Research - Oxford instruments) in the built-in Vector-PFM mode, which allows recording of the lateral (torsion motion of the cantilever) and normal (deflection) PFM signals during the same scan, as is depicted in Fig. 3.14(b).

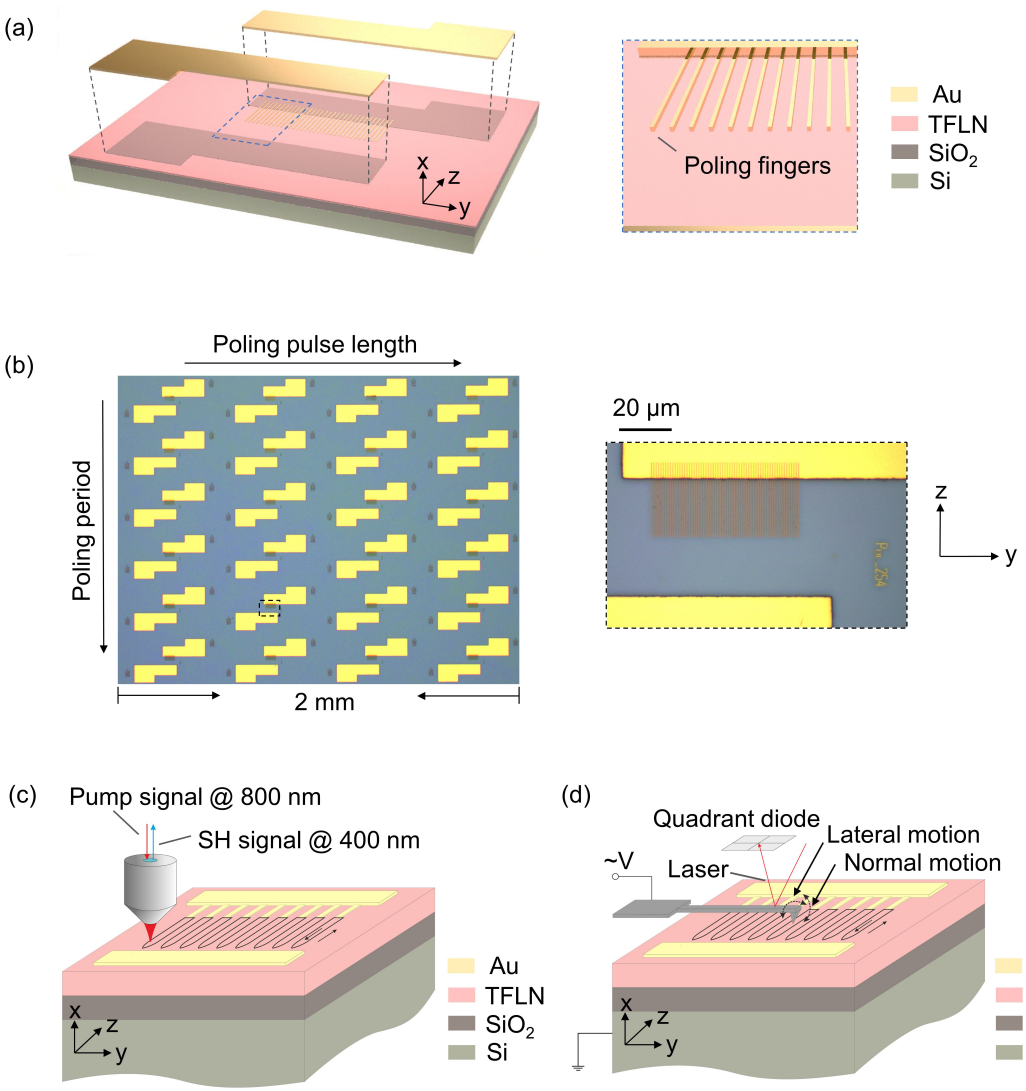

Figure 3.14: (a) Exploded representation of the x-cut TFLN with surface electrodes for poling, where the thin poling finger electrodes were first fabricated using electron-beam lithography, and the thick probe contact pads were formed by photolithography subsequently. Inset shows the poling finger electrodes. (b) Microscope images of the fabricated device. As an example, inset shows one set of poling electrodes with a period of 800 nm. (c) and (d) Schematic illustrations of second-harmonic (SH) microscopy (c) and piezoresponse force microscopy (PFM) (d) imaging of the poled sample.

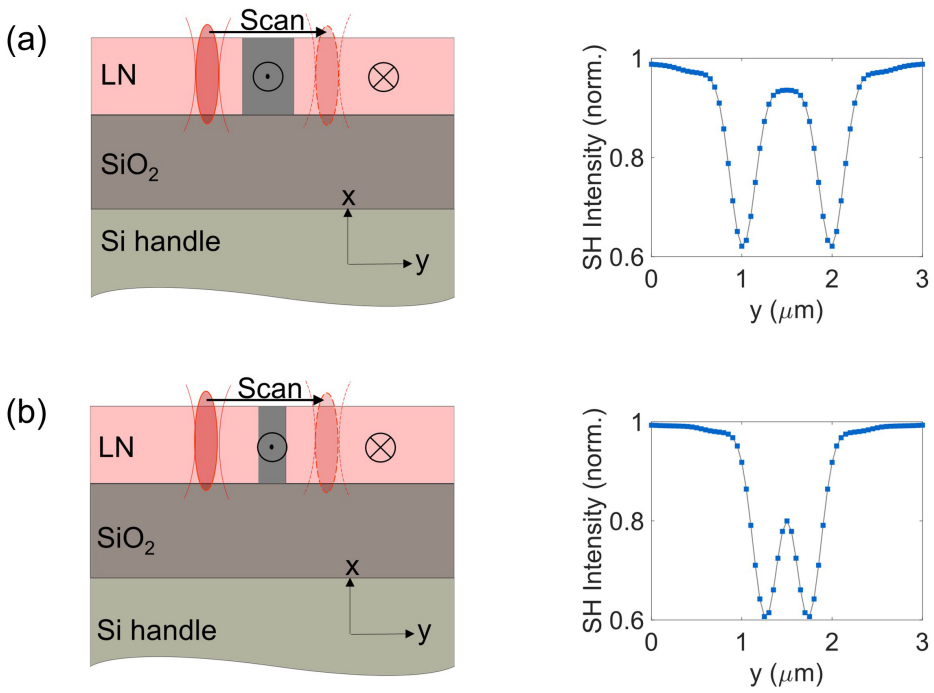

Figure 3.15: Simulated line scans over 1 μm (c) and 500 nm (d) wide domains.

3.6.3 Results

Figure 3.16 shows SH microscope images of domain structures with poling periods of 2.8 μm (a), 2 μm (b) and 1.5 μm (c). In order to create a typical 2D image, a selected region was scanned with 50 nm and 150 nm step width along the y and z axis of the TFLN respectively, and 5 ms signal integration time per acquisition point. The poling electrodes are visible as dark stripes and rectangles at the top and bottom of the image, because the electrode material (gold) features no second order nonlinearity in the optical band. The domain walls (DWs) appear as dark lines stretching from the positive to the negative electrodes and the bright regions surrounded by the DWs correspond to the inverted regions. The calculated duty cycles are $48.8\% \pm 1.5\%$, $44.3\% \pm 3.3\%$ and $51.2\% \pm 4.2\%$ for $\Lambda = 2.8$ μm, 2 μm and 1.5 μm respectively. This estimation is based on line-scans of the SH signal through the middle of the poling region over 20 periods. Down to the 1.5 μm period, as shown in Fig. 3.16, we observe a SH signal of similar levels in the inverted and unpoled regions nearby indicating not just surface domains, but domains inverted

towards almost the complete film thickness.

The structures with periods of 1 μm down to 600 nm were analyzed with PFM (the corresponding SH images are provided in the supplementary material). For scanning a full metal Ir/Pt tip (Rocky Mountain Nanotechnology, LLC) with a tip apex of about 30 nm was used. The measurement was performed in resonance-enhanced PFM with an AC signal with an amplitude of up to $\pm$ 4 V. For the measurement the long axis of the PFM tip was mounted orthogonal with respect to the z-axis of the crystal as indicated by Fig. 3.14(d). The measurements of the 1 μm period electrodes show the results obtained in the normal signal channel (buckling motion) driven at an AC frequency of 234 kHz. The signals of the 800 nm and 600 nm period structures were obtained after a change of the cantilever and also show the normal signal channel driven at an AC frequency of 82 kHz. The scan direction was parallel to y-axis of the crystal and the scan speed for all scans was smaller than 1 Hz with step sizes less than 30 nm.

Figure 3.17 shows the PFM and SH images of a 1 μm period electrode structure. Figure 3.17(a) depicts the measured SH signal, while (b)-(d) show the surface topography (b), PFM amplitude (c) and phase signals (d), respectively. The topography record in Fig. 3.17(b) shows an otherwise flat surface with only the poling electrodes at the top and the bottom of the image being visible. During the measurement it was noted that the Pt/Ir tip removes the gold layer of the thin poling electrode fingers, so here only a $\sim$ 10 nm surface topography can be seen from Fig. 3.17(b). This is in agreement with the thickness of the Cr adhesion layer, which appears not to be affected by the scan. In contrast, the 300 nm thick gold probe contact pad is not removed by the tip. The removed gold was pushed by the tip outside of the image frame and did not interfere with the measurement. The PFM phase signal (d) shows a $\sim 180^\circ$ phase shift of the piezoresponse in domains with opposing directions due to the inversion of the piezoelectric tensor in poled regions [80], where color orange and purple represents the unpoled areas and the inverted domains respectively. In contrast, the amplitude signal (c) only shows a contrast sensitive to the domain transitions. This behavior of the PFM amplitude signal is expected [80].

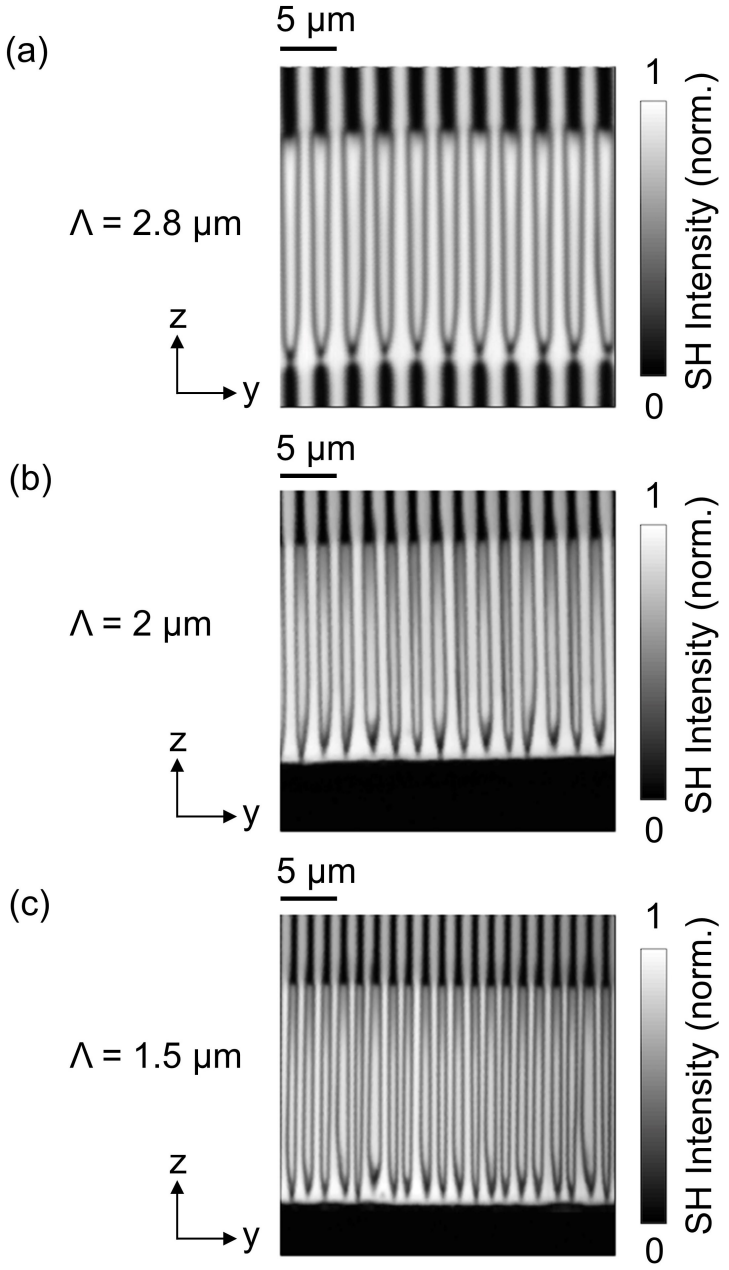

Figure 3.16: Typical SH images of poled samples with 2.8 μm (a), 2 μm (b), and 1.5 μm (c) poling period.

Because when the tip is placed above a domain wall, the piezoresponse signal of two adjacent domains will partly cancel, due to the inversion of the piezoelectric tensor. Further, the measured PFM amplitude signals in the poled and unpoled regions are quite similar [see Fig. 3.17(c)]. In analogy to the SH contrast mechanism, the PFM amplitude is expected to be reduced if domains

of different polarity are stacked vertically[80, 81]. From experiments and theory, it has been reported that the PFM amplitude signal can provide a domain depth sensitivity of up to 1.7 μm independent of the ferroelectric material [80, 81], which is significantly larger than our film thickness (300 nm). Therefore, the observation of a DW contrast rather than a domain polarity indicates—in agreement with the SH results—that the inverted domains completely extend over the film thickness. Hence, the SH image (a) and PFM amplitude image (c) match well with each other as can be seen by several identical details. (The scanned area in the SH image is shifted by 2 periods to the left, compared to the PFM images, as a result of the manual positioning of samples in different instruments.) It should be noted that our results augment previously-reported PFM results on x-cut LNOI samples, where no PFM phase images were reported, while the PFM amplitude images did show a domain polarity contrast rather than a DW contrast [129, 130].

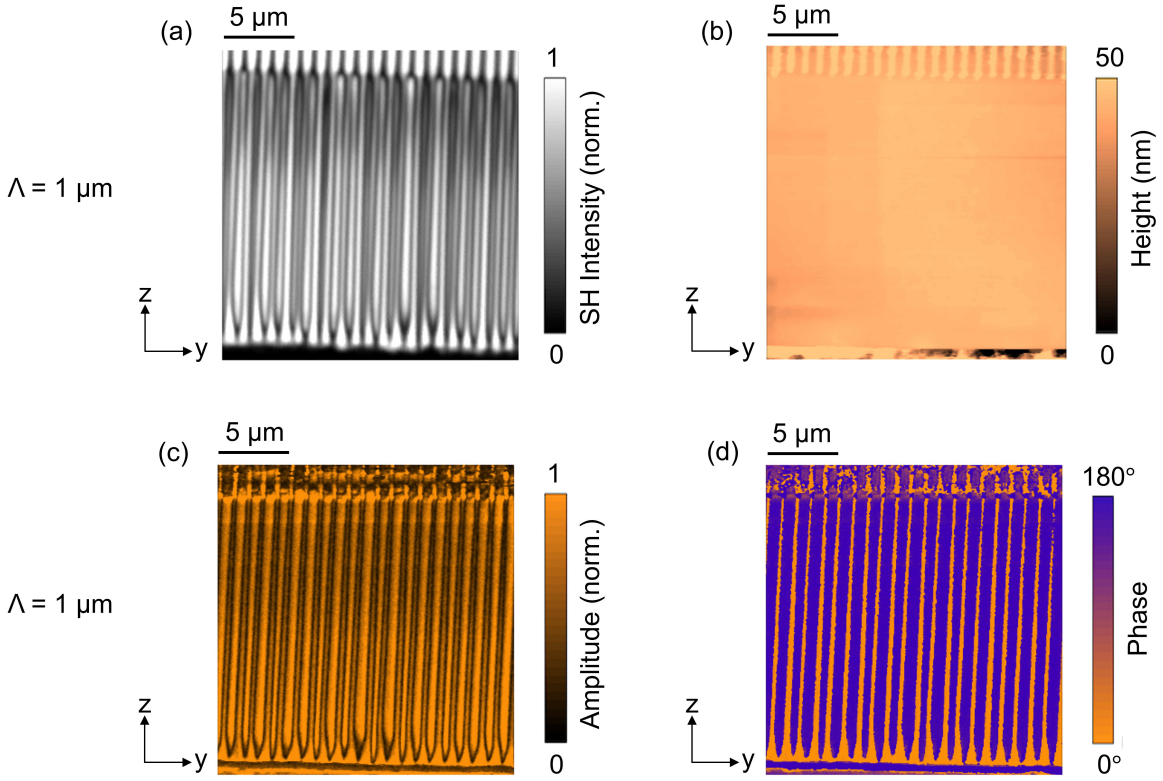

Figure 3.17: SH image (a), surface topography (b), PFM amplitude (c) and phase (d) images of a poled sample with 1 μm period.

Figure 3.18 shows the PFM images from electrodes with periods of 800 nm (column on the left) and 600 nm (column on the right), where Figs. 3.18(e) and (f) are the zoomed-in images generated from the areas enclosed by the white dashed lines in Figs. 3.18(a) and (b), respectively. As observed before, the phase images [panels (c)-(d)] show a $\sim 180^\circ$ phase shift of the piezoresponse in domains of different polarity, while in the amplitude images [panels (a)-(b)], it is mainly the domain transitions that can be seen. For the 800 nm period structures, we observe a mostly similar PFM amplitude in poled domains as in the unpoled areas. This indicates that the inverted domains do penetrate most of the film thickness as discussed above. For the 600 nm period structures, the amplitude signal of the wide domains is similar to that from the unpoled region, but in the narrow domains only a partly recovered amplitude is observed. While the relatively low amplitude signal measured here may indicate partly inverted domains, on closer inspection, the zoomed-in amplitude image in Fig. 3.18(e) shows not-completely-recovered signal in the unpoled area compared to the wide inverted domains as well. This can be interpreted as that the width of these narrow structures (< 100 nm) is at the limit of the PFM resolution, which is correlated with the radius of the scanning tip. For bulk single crystalline LN, the estimated lateral resolution for the metallic tip used here (radius ≈ 30 nm) is around 36 nm [80]. The images of the 800 nm electrode show domain structures of the targeted period, with each domain reaching the ground electrode. The domain structures with 600 nm period show an interesting behavior, where every second domain only propagate to about the middle of the poling gap, leading to a pattern with an effectively doubled period (compared to the designed period) in the area near the ground electrode. A closer inspection of the 1 μm and 800 nm period structures already indicates that approximately every second domain is slightly narrower than the two respective neighboring domains. This behavior is observed in all our poling experiments of the submicron-period structures, and is progressively more pronounced with smaller periods, which could only be partly compensated by optimizing the poling pulse form. Therefore, a systematic interaction of domains is indicated for further study from a physics perspective.

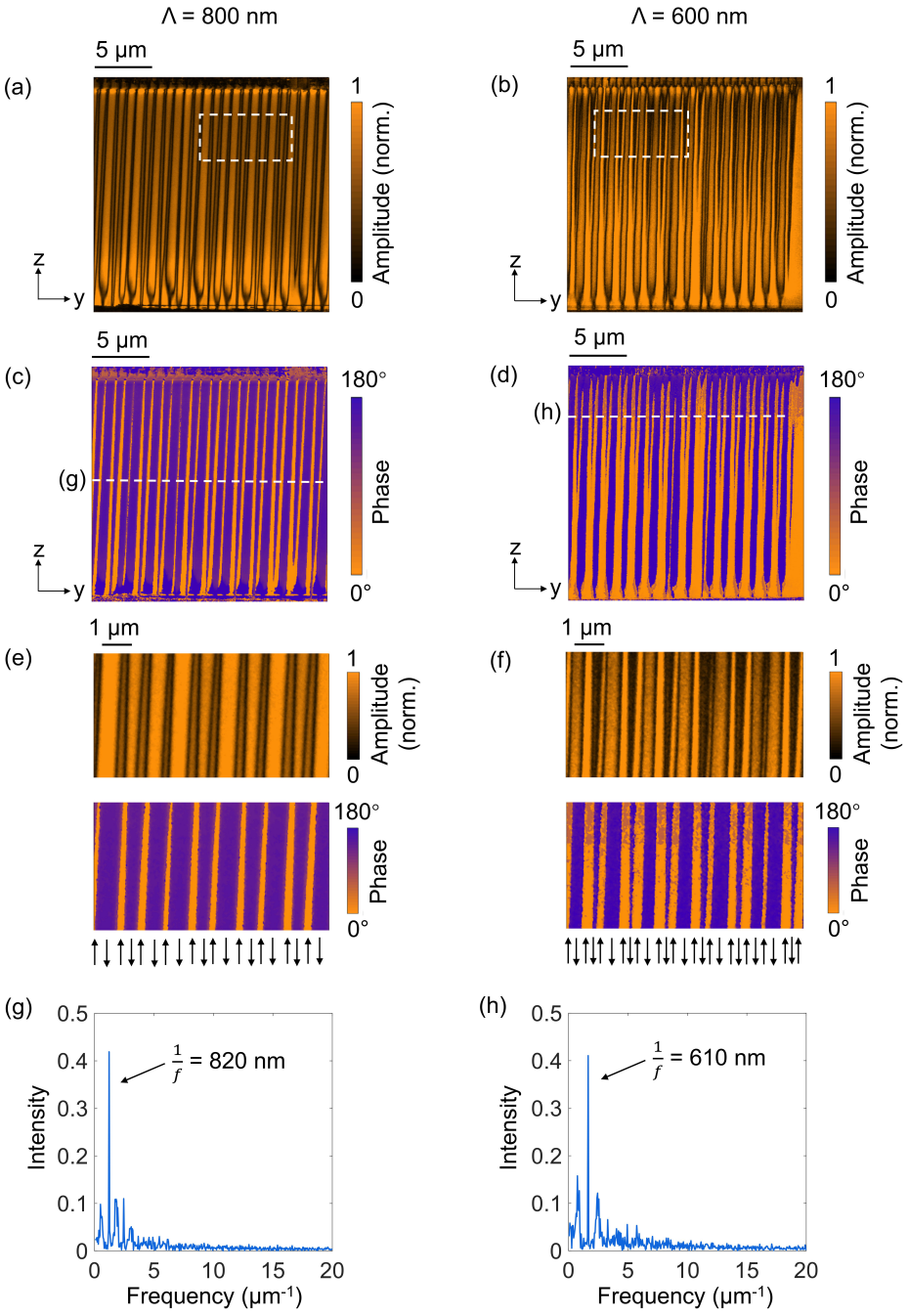

Figure 3.18: (a)-(d) PFM amplitude and phase images of structures with a poling period of 800 nm (column on the left) and 600 nm (column on the right). (e) and (f) Zoomed-in PFM amplitude (top panel) and phase (bottom panel) images for the 800 nm and 600 nm period structures obtained from the areas enclosed by the white dashed lines shown in panels (a) and (b); Arrows on the bottom indicate the orientation of spontaneous polarization of TFLN, where upward and downward arrows represent the un-inverted and inverted domains, respectively. (g) and (h) Fourier spectrum of the PFM phase data acquired from the region shown with the white dashed lines in panels (c) and (d); f is the spatial frequency, in unit of μm^{-1}.

3.6.4 Discussion

From literature, it is well established that DWs in LN, as well as other ferroelectrics, are accompanied with various effects[131, 78], such as strain [132, 133], charges and electric fields [134, 135]. While the length scale of domain transition (defined as the change of sign of spontaneous polarization) is measured and predicted to be on the order of a few unit cells [136, 137, 138, 131, 139, 140], the accompanying effects, such as strain fields and electric fields, have been observed to expand over a wide range varying from a nanometer to several microns around the DWs [131, 78, 141]. In agreement with these length scales, we observe an interaction of neighboring domains with periods of 1 μm and less. Interestingly, we do not just observe a random pattern of domains, but rather structures with a double periodicity, where every second domain grows at the cost of its two neighbors. Recently, periodic and quasi-periodic patterns on sub-micron scales have been observed in domains written by biased scanning probe microscopy (SPM) tips in polar (z-cut) and non-polar cuts (x- and y-cut) of bulk LN [108, 142]. In a similar manner to our experiment, for large domain spacing, uniform domain chains were formed with SPM writing, while as the distance between the adjacent bias application locations gets smaller, domains of non-equal sizes with a double periodicity were observed. By further decreasing the domain spacing, domains with a triple periodicity and eventually quasi-periodic and non-periodic patterns were formed [108]. The origin of these behaviors is believed to be domain-domain interactions through electrostatic and strain fields, and a theoretical model was developed to generate the phase diagram of the domain switching behaviors [108]. More importantly, according to Ref. [108], transitions of these domain patterns from uniform chains to period doubling structures, and then to quasi-periodic structures can be achieved by varying the poling temperature or the relative humidity at the sample surface. As is shown in Figs. 3.18(b) and (f), domains with DW-DW distances less than 200 nm have already been fabricated by simply adjusting the poling pulse height and length. This suggests that uniform domain structures with even smaller periodicities could be formed with improved control of the poling pulse as well as the poling environment.

Other possible approaches to further improve the poling uniformity include using multiple poling pulses [143, 129], poling differently doped LN to support the pinning of domain structures, and UV light-assisted poling[144, 145]. Indeed, the domain to domain interactions are not yet very well understood in TFLN and require further investigation, in which Kelvin probe force microscopy could be used to image and visualize space charge distributions around the DWs [142].

It should be noted that while for the 600 nm period electrodes only every second domain reaches the ground electrode, periodic structures with the designed parameters are still present close to the positive electrode, as is shown in Figs. 3.18(f) and (h). To obtain a quantitative estimate of the achieved periodicity, we calculated the Fourier transform of the PFM phase data line scan, acquired from the slices indicated by the white dashed lines shown in Figs. 3.18(c) and (d); similar studies have been performed in Ref. [31], for example. The Fourier spectra from the two line-scans are shown in Figs. 3.18(g) and (h), which show a main period of 820 nm and 610 nm with the peak amplitude being 0.42 and 0.41 respectively. The calculated peak amplitude here is slightly reduced from the ideal value of 0.64 $[(2/\pi)\sin(\pi/2)]$, which is the leading coefficient in the Fourier series for a periodic square-wave function with 50% duty cycle. The period doubling behavior of the switched domains appears as the side lobes in the Fourier spectra. The calculated duty cycle from these two line-scans are $67.7\% \pm 9.1\%$ and $54.3\% \pm 12.4\%$ respectively. Though the uniformity of the domain structures here is not as good as that of the larger periods, due to the speculated domain interactions, the results still demonstrate a fairly uniform domain grid comparable to structures used in the reported efficient nonlinear devices [125]. Note that the width of the poling region here is 20 μm, while typical fundamental TE mode in TFLN waveguides only extends to less than 5 μm (in the z direction) [9, 10, 13]. Even for the 600 nm period structures poled here, there still appears to be adequate space to fabricate optical waveguides where the period is well reproduced, as is shown in Figs. 3.18(f) and (h).

All the fabricated domain structures have been stable for at least eight months between the initial poling, SH imaging and the subsequent PFM analysis. Using a 2.8 μm QPM periodicity, we have fabricated 5 mm long periodically-poled waveguides which were used as sources of entangled photon pairs at telecommunications wavelengths [128]. Because the test chips reported here contained a large number of poled structures of relatively short length in order to explore the parameter space, we have not yet fabricated optical waveguide structures with the shorter QPM dimensions. However, we do not see a fundamental limitation in the development of optical waveguides that are at least several millimeters in length using the same poling protocol.

3.7 Conclusion

In this chapter, we have discussed poling of x-cut TFLN, including current challenges, diagnostic methods and our strategies for poling waveform optimization. Poling of LN can be affected by various factors, including poling electrode duty cycle, shape [146], material [75], poling waveform, as well as pulse numbers [106]. Here, we have shown successful poling of x-cut MgO doped TFLN with periods varying from 2.8 μm to 800 nm, using the lithographically-structured gold electrodes, with 35% duty cycle and single voltage pulses. All the reported poling processes here were conducted at room temperature. SH microscopy and PFM were used to inspect the domain structures, which show domain grids with periods down to 600 nm, and features with sizes less than 200 nm. We observed period doubling behaviors in the sub-micron period structures formed by domain interactions, which is progressively more pronounced with smaller periods. These period-doubled structures might be formed by the electrostatic fields surrounding the adjacent domain walls (distance less than 500 nm) [108]. Further improvements in the domain uniformity with even smaller periods can be expected by optimizing the poling temperature and environment humidity, or by adapting a different poling strategy. For example, poling with multiple bipolar preconditioning pulses could potentially improve the poling yield

and quality [106]. Nevertheless, our work presented in this chapter shows that the same poling protocol can be used to fabricate domain grids with periods over a wide range, through only slight modifications in the poling waveform, which provides one key step towards the realization of thin-film PPLN based nonlinear devices, such as mirrorless OPO.

3.8 Acknowledgments

Chapter 3, contains the material as it appears in the following: Jie Zhao, Michael Rüsing, and Shayan Mookherjea, "Optical diagnostic methods for monitoring the poling of thin-film lithium niobate waveguides", Optics Express 27 (9), 12025 (2019) and Jie Zhao, Michael Rüsing, Matthias Roeper, Lukas M. Eng, and Shayan Mookherjea, "Poling thin-film x-cut lithium niobate for quasi-phase matching with sub-micrometer periodicity", Journal of Applied Physics 127, 193104 (2020). The dissertation author, together with her adviser, led the research efforts for this work and co-authored the paper.

Chapter 4

Design of PPLN Waveguides

4.1 SHG Theory

In an SHG process, two photons with the same frequency (ω_1) are combined and interact with the nonlinear material, and then generate a new photon with a doubled frequency of the initial photons ($\omega_2 = 2\omega_1$), obeying the law of energy conservation. SHG was first demonstrated by Franken et al. [147] in 1961, shortly after demonstration of the first laser [148], where a ruby laser with a wavelength of 694 nm is focused on a quartz sample and generated a 347 nm SH light. Since then, SHG has been widely used to create sources of coherent radiation at hitherto unattainable wavelengths.

4.1.1 Quasi-Phase Matching

For efficient SHG, the momentum conservation or phase matching condition also has to be satisfied, allowing the harmonic fields generated in different areas along the crystal to interfere constructively at the output. This requires that the refractive indices of the fundamental and SH wave are equal, i.e., $n_{FH} = n_{SH}$. However, due to material dispersion, the phase matching condition often cannot be achieved, leading to phase mismatch. As is shown in Fig. 4.1(b), for

the non-phase-matched scenario, a small fraction of the launched optical power oscillates back and forth between the fundamental and SH waves. In the first coherence length, the pump wave at ω_1 will produce an SH wave at ω_2, but at the second coherence length the SH wave will generate a difference frequency wave at ω_1. For example, if the crystal length is exactly two coherence length, no SH light will be created, and also no pump power will be lost. The concept of QPM was first proposed in 1962 by Armstrong et al. [149], to realize efficient energy transfer between the interacting waves in nonlinear crystals. The momentum is conserved through an additional momentum contribution from a periodic structure, which is fabricated by periodically reversing the orientation of the spontaneous polarization (P_s) and also the sign of the second-order susceptibility ($\chi^{(2)}$) of the crystal. The period of this domain grid satisfies $\Lambda = 2\pi/\Delta k$. As is shown in Fig. 4.1(b), in each coherence length, the interacting waves still propagate with different phase velocities in the material, but when the accumulated phase mismatch get to π (at one coherence length), the sign of $\chi^{(2)}$ is reversed. This allows the energy to continue to positively flow from the pump to the SH waves, and generate a step-wise growth in the SH power along the length of the crystal.

4.1.2 Normalized Nonlinear Conversion Efficiency

In TFLN waveguides, one of the most commonly-used figure of merit to evaluate the efficiency of a SHG device is normalized nonlinear efficiency (η_{norm}). It is defined as follows:

$$\eta_{norm} = \frac{P_{SH}}{P_{FH}^2 L_{NL}^2} \times 100\%, \tag{4.1}$$

where P_{FH} and P_{FH} represent pump and SH power, and L_{NL} is the length of the nonlinear interaction region, which is also the length of the poled region. Assuming the interacting waves are propagating along the y axis of the TFLN, and there is no waveguide loss, the coupled-mode

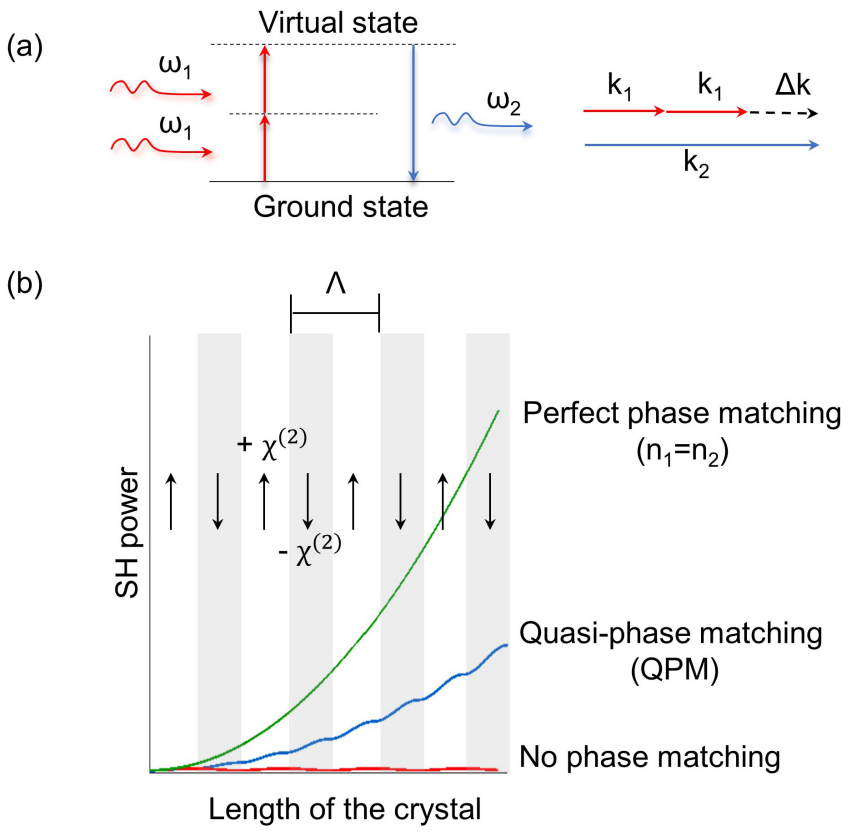

Figure 4.1: Schematic illustration of the SHG (a) process and QPM (b).

equations describing the interaction between the pump and SH waves are [37, 150]:

$$\frac{dA_{\mathrm{SH}}(y)}{dy} = -j\frac{4\pi}{n_{\mathrm{SH}}\lambda_{\mathrm{SH}}}A_{\mathrm{FH}}^{2}(y)\Gamma(x,y,z)e^{j\Delta ky}, \tag{4.2}$$

$$\frac{dA_{\mathrm{FH}}(y)}{dy} = -j\frac{4\pi}{n_{\mathrm{FH}}\lambda_{\mathrm{FH}}}A_{\mathrm{FH}}^{*}(y)A_{\mathrm{SH}}(y)\Gamma(x,y,z)e^{-j\Delta ky}, \tag{4.3}$$

where $\Delta k = k_{\mathrm{SH}} - 2k_{\mathrm{FH}} - 2\pi/\Lambda$, and Λ is the poling period of the TFLN. $\lambda_{\{\mathrm{FH,\ SH}\}}$, $n_{\{\mathrm{FH,\ SH}\}}$ and $k_{\{\mathrm{FH,\ SH}\}}$ are the wavelength, mode index, and wavevector of the fundamental TE mode for the pump and SH waves, respectively, c is the speed of light in vacuum, ε_0 is the vacuum permittivity, and L_{NL} is the length of the nonlinear interaction region. Γ is the nonlinear mode overlap between the pump and SH waves, and is defined as:

$$\Gamma = \iint_A \varepsilon^*_{\mathrm{SH}}(x,z)\boldsymbol{d}(x,y,z)\varepsilon_{\mathrm{FH}}(x,z)\varepsilon_{\mathrm{FH}}(x,z)\,dx\,dz, \tag{4.4}$$

where $\varepsilon_{\{\mathrm{FH,\ SH}\}}$ is the transverse mode profile at the pump and SH wavelength respectively. $\boldsymbol{d}(x,y,z)$ is a function of d_{33}, which is only nonzero in the area where the TFLN sits:

$$\begin{aligned} \boldsymbol{d}(x,y,z) &= \frac{2}{\pi} d_{\mathrm{eff}}(x,z) e^{i2\pi y/\Lambda}\hat{z}, \\ d_{\mathrm{eff}}(x,z) &= \begin{cases} d_{33}, & \mathrm{LN} \\ 0, & \text{Other region} \end{cases} \end{aligned} \tag{4.5}$$

For non-depleted pump approximation, the expression for P_{SH} can be derived as:

$$P_{\mathrm{SH}} = (\frac{2}{\pi})^2 \frac{8\pi^2|\Gamma|^2 P^2_{\mathrm{FH}} L^2_{\mathrm{NL}}}{n_{\mathrm{SH}} n^2_{\mathrm{FH}} c\varepsilon_0 \lambda^2_{\mathrm{FH}}} sinc^2(\frac{\Delta k L_{\mathrm{NL}}}{2}), \tag{4.6}$$

If we consider propagation loss in the waveguide, then the derived P_{SH} is:

$$\begin{aligned} P_{\mathrm{SH}} = (\frac{2}{\pi})^2 &\frac{8\pi^2|\Gamma|^2 P^2_{\mathrm{FH}} L^2_{\mathrm{NL}}}{n_{\mathrm{SH}} n^2_{\mathrm{FH}} c\varepsilon_0 \lambda^2_{\mathrm{FH}}} e^{-(\alpha_{\mathrm{FH}}+\alpha_{\mathrm{SH}}/2)L_{\mathrm{NL}}} \\ &\times [\frac{\sin^2(\frac{\Delta k L_{\mathrm{NL}}}{2}) + \sinh^2(\frac{(\alpha_{\mathrm{FH}}-\alpha_{\mathrm{SH}}/2)L_{\mathrm{NL}}}{2})}{(\frac{\Delta k L_{\mathrm{NL}}}{2})^2 + (\frac{(\alpha_{\mathrm{FH}}-\alpha_{\mathrm{SH}}/2)L_{\mathrm{NL}}}{2})^2}], \end{aligned} \tag{4.7}$$

where $\alpha_{\{\mathrm{FH,\ SH}\}}$ represents the waveguide propagation loss of the fundamental TE mode for the pump and SH waves. More details can be found in Ref. [150].

Though η_{norm} is a quantity that reflects the enhancement of nonlinear optical properties due to, e.g., transverse modal confinement and a high value of the transverse mode overlap integral, it does not necessarily result in high overall conversion unless long waveguides can be fabricated with uniformly-good QPM properties, and eventually, a significant amount of pump power can be handled. To complement this, another important consideration is the nonlinear

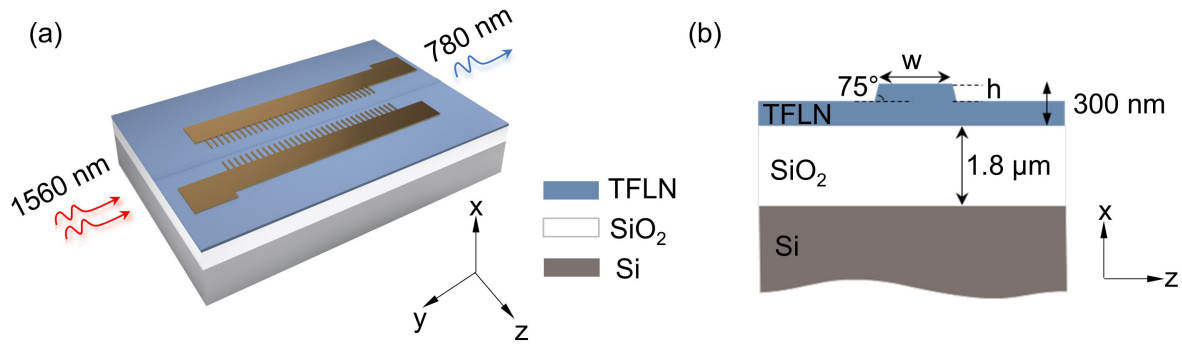

Figure 4.2: Schematic illustration of the PPLN waveguide with poling electrodes (a), and the waveguide cross-section (b).

conversion efficiency (η), which is defined as output power divided by the square of the input power (units: $\%W^{-1}$). This figure of merit is useful and insightful because it includes the scaling with the device length; not all devices, especially in the nano-photonic regime, can be poled uniformly over long waveguide lengths.

4.2 Waveguide Design Considerations

In our experiment, we consider SHG from 1560 nm to 780 nm [see Fig. 4.2(a)]. This process is particular interest for applications in laser cooling and manipulation of Rb atoms [151], because 780 nm matches the D2 line transition in Rb. As has been mentioned in the previous chapter, the material used here is 300 nm thick, 5 mol% MgO-doped TFLN, acquired from NanoLN (Jinan Jingzheng Electronics Co., Ltd.). We use Lumerical MODE Solutions to simulate the mode profiles and refractive indices of the fundamental TE mode at the pump and SH wavelengths. Based on the simulations, we can calculate η_{norm} and the required poling period (Λ).

As is shows in Fig. 4.2(b), in our simulations the thickness of TFLN and buried oxide layer is fixed at 300 nm and 1.8 μm respectively, while width (w) and etching depth (h) of the waveguide ridge are swept to find the optimal waveguiding structure. In the simulation, we used

$d_{33} = 25$ pm/V, which is the same as reported in the previous publications [10]. In terms of fabrication process tolerance, Figs. 4.3(a) show that shallow-etched waveguides ($h = 50$ nm) are less sensitive to waveguide width variations. In general, TFLN waveguides are formed by physically structuring (e.g., etching or dicing) LN, or by rib-loading the LN film with a second material, e.g., silicon nitride. The etched TFLN waveguides can provide a higher degree of mode confinement and higher conversion efficiency than the hybrid waveguides. However, a long-standing and unresolved concern, as is mentioned recently by Boes *et al.* [12], is that the QPM wavelength (λ_p) is highly sensitive to the waveguide dimensions, e.g., width (w), which is exacerbated in TFLN structures, compared to bulk LN devices. Here, the shallow-etched waveguides can improve the tolerance to fabrication non-uniformities, achieving similar width-sensitivity as that of the rib-loaded (unetched LN) waveguide structure (see next chapter), but also has the higher conversion efficiency as that of the etched waveguide. Furthermore, shallow-etched waveguides may incur less propagation loss due to edge roughness. As Fig. 4.3(a) shows, we can use a larger poling period for shallow-etched structures, which leads to easier fabrication and a better fidelity to design. As has been discussed in the previous chapter, domain structure with a larger period suffers less from the domain-spreading effect. In addition, because here the long poling electrodes (several milimeters) are fabricated using standard photolithography process, width of the electrode fingers is limited by the lithography resolution, which is about 1 μm in our experiment. To precompensate for the domain spreading in the poling process, duty cycle of the electrodes are often designed to be 35%, setting an upper limit on poling period of about 2.86 μm. Figure 4.3(a) indicates that a more deeply etched, narrow-ridge waveguide could achieve about a factor of two higher SHG efficiency, but would require a substantial reduction of the poling period to about 2 μm, and has less tolerance to variations as shown by the steep curvature of the contours. Therefore, we chose this shallow-etched waveguiding structure for our SHG device.

This type of waveguides have an optimal width; Fig. 4.3(b) shows that the nonlinear conversion efficiency for the shallow-etched waveguide is maximized when $w = 1.2$ μm. Figure 4.4

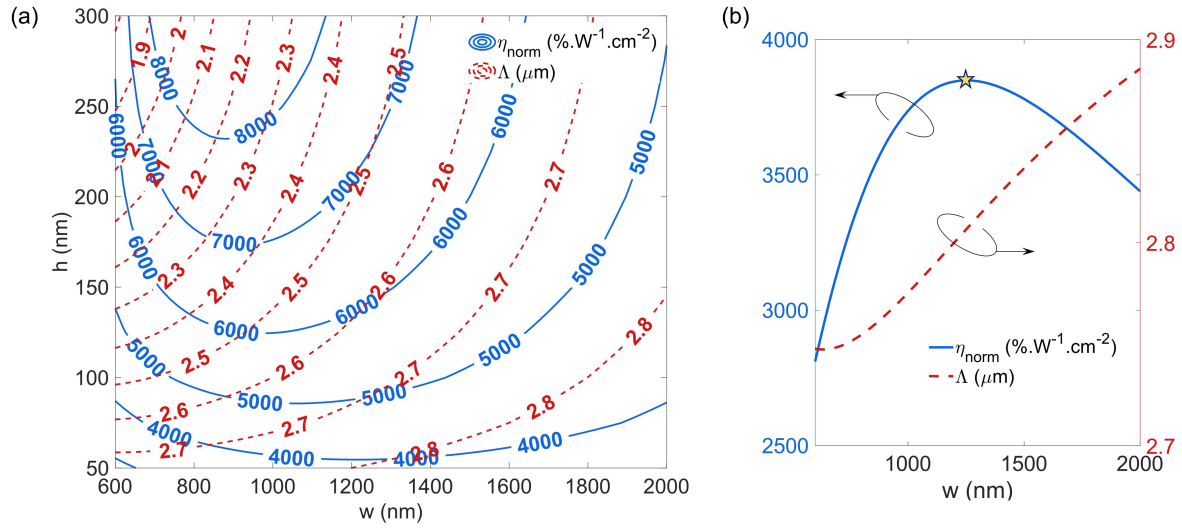

Figure 4.3: (a) Simulated η_{norm} (solid blue lines) and the required poling period (dashed red lines) as a function of w and h. (b) Simulated η_{norm} (solid blue lines) and the required poling period (dashed red lines) as a function of w, with h fixed at 50 nm.

shows the simulated mode profiles of the fundamental TE mode at both 1560 nm and 780 nm, for $w = 1.2$ μm and $h = 50$ nm. The calculated effective mode areas are 1.1 μm^2 at 1560 nm and 0.4 μm^2 at 780 nm. Such waveguide structures provide for a good overlap between the quasi-TE-polarized fundamental modes at the widely-separated pump [Fig. 4.4(a)] and the SH [Fig. 4.4(b)] wavelengths, calculated to be O =78% based on the standard equation below:

$$O \equiv \left|\mathrm{Re}\left[\frac{(\int \vec{E}_1 \times \vec{H}_2^* \cdot \mathrm{d}\vec{S})(\int \vec{E}_2 \times \vec{H}_1^* \cdot \mathrm{d}\vec{S})}{\int \vec{E}_1 \times \vec{H}_1^* \cdot \mathrm{d}\vec{S}}\right] \times \frac{1}{\mathrm{Re}(\int \vec{E}_2 \times \vec{H}_2^* \cdot \mathrm{d}\vec{S})}\right|, \tag{4.8}$$

where $\vec{E}_{\{1,\,2\}}$ and $\vec{H}_{\{1,\,2\}}$ represents the electric and magnetic fields at the pump and SH wavelength respectively. Based on these considerations, our optimum waveguide width was 1.2 μm, etching depth was 50 nm, and poling period was 2.8 μm.

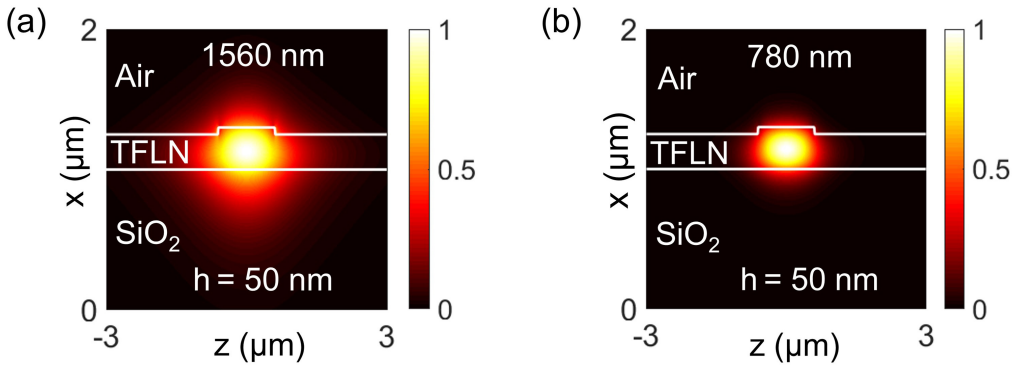

Figure 4.4: Simulated mode profiles (intensity of the electric field) of the fundamental TE mode at 1560 nm (a) and 780 nm (b).

4.3 Acknowledgments

Chapter 4, contains the material as it appears in the following: Jie Zhao, Michael Rüsing, Usman A. Javid, Jingwei Ling, Mingxiao Li, Qiang Lin, and Shayan Mookherjea, "Shallow-etched thin-film lithium niobate waveguides for highly-efficient second-harmonic generation", Optics Express 28(13), 19669 (2020). The dissertation author, together with her adviser, led the research efforts for this work and co-authored the paper.

Chapter 5

Second-Harmonic Generation Measurements

5.1 Fabricated Device

Poling electrodes with a uniform 2.8 μm period were first defined on the x-cut LNOI surface using the standard photolithography process. In cross-section, the electrodes consist of a 10 nm Cr adhesion layer deposited on TFLN, followed by a 300 nm Au layer. The separation gap between the two opposing electrode ”teeth” facing each other was designed to be 20 μm, based on an estimate of the critical field required to initiate poling. Transformer oil was used to surround the probe-pad contact point and the immediate vicinity of the electrodes along the entire length of the waveguide, which helped prevent arcing and electrode breakdown. The voltages required for poling are generally less than 1 kV. Here, A single high voltage pulse was applied to the poling circuit through a high-voltage amplifier, using a voltage waveform described in the previous chapter. Next, a sequence of shallow ridges to define the waveguide centers were then etched using Ar-ion milling, using an electron-beam resist as the mask as described in Ref. [64]. The upper cladding of the waveguides was left as air after etching. Since the electrodes are far

from the waveguide, they were not removed after the poling process was completed. Twenty-four waveguides were fabricated on this chip, with varying waveguide widths. (The actual etching depth was ∼48 nm, and the resist shrinkage was estimated to be about 100 nm. These values will be taken into account in the theoretical calculations discussed below.) The waveguide propagation losses at the pump and SH wavelengths are less than −1 dB/cm and −3.2 dB/cm respectively, estimated by measuring the insertion loss of waveguides with different lengths (the cutback method), performed on five waveguides for each length. In this study, we did not observe a clear correlation between the total insertion loss and waveguide dimension. The length of the etched waveguide is 7 mm, without taper formation, while the poled region is 5 mm, as is illustrated in Fig. 5.1(a).

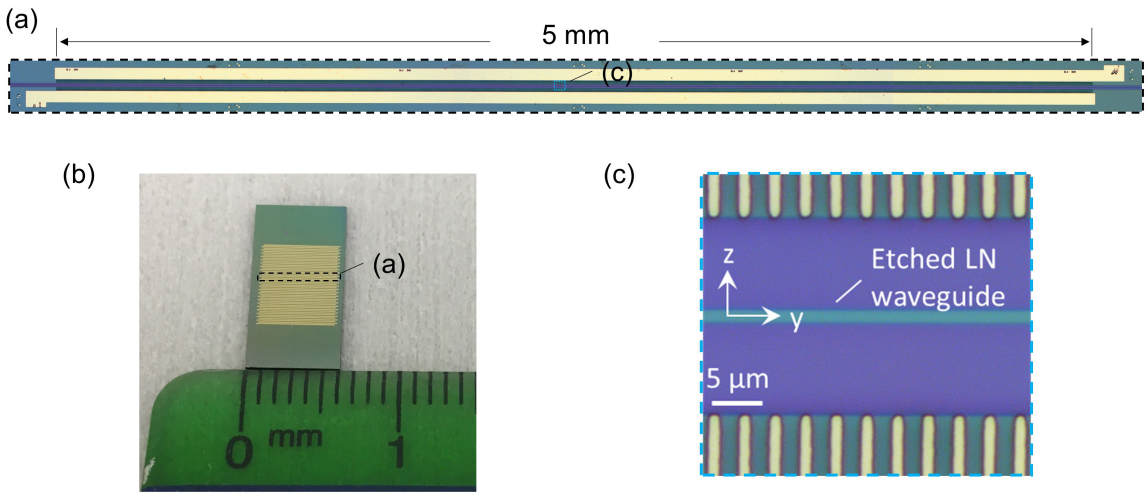

Figure 5.1: (a) Optical microscope image of one fabricated waveguide with poling electrodes. (b) Camera image of the fabricated chip with multiple waveguides and poling electrodes. (c) Optical microscope image of a selected region in the fabricated waveguide.

5.1.1 Poling Quality

Uniform and accurately-sized periodically-inverted domains are the sign of high poling quality. Second-harmonic microscopy is used here to image the inverted domains. Typical domain structures are shown in Figs. 5.2(b)-(f), in which the dark stripes at the top and bottom of the

images are the poling electrodes, the bright rectangle in the middle of the images represents the etched waveguide, and the black straight lines that start from the top (positive) electrodes and terminate at the bottom (ground) electrodes are the domain walls. In between the opposing poling electrodes, the orientation of P_s is reversed, which is indicated by the red arrows in Fig. 5.2(d). The inverted and uninverted regions are separated by the domain walls. Details of the SH measurement technique and analysis are reported elsewhere [152, 107]. To calculate the poling duty cycle, five SH images were generated over several segments along the waveguide, each with an area of 100 μm $\times$ 30 μm, as is shown in Figs. 5.2(b)-(f). For this test chip, the poling duty cycle varied from 45% to 60%. For the three waveguides reported below, the waveguide widths were 1.14 μm, 1.24 μm and 1.32 μm respectively. Based on the SH images, the poling duty cycles mean value and one standard deviation were: 57.2% $\pm$ 3.5%, 55.2% $\pm$ 3.0% and 46.4% $\pm$ 4.4%, respectively. The quantification method is described in the Appendix.

In order to determine whether the thin film was poled adequately in depth, we performed a quantitative analysis of the line scans of images such as shown in Fig. 5.3. In contrast to our technique, traditional depth-resolved poling diagnostic methods such as etching waveguides using acid to reveal the domain orientation [14] are destructive in nature, typically only revealing data of a poled structure that is no longer useful as a working optical device. Physics-based modeling and key differences with regard to traditional SH microscopy of domain walls (e.g., Ref. [153]), are discussed in detail in Ref. [107]; in particular, we are able to estimate the depth of poling with a resolution that is not dependent on the diffraction-limited focus size, but on the (much shorter) coherence length of the surface-pumped SHG process [85]. Thus, as shown in the exemplar case of Fig. 5.3(b), when studying the cross-section indicated using a red line in Fig. 5.3(a), we inferred that the poling depth was closer to 245 nm than either 240 nm or 250 nm, i.e., achieving about 5 nm depth resolution. Using such non-destructive, high-resolution 3D diagnostic images, we verified that, after the poling recipe was optimized, the achieved poling duty cycle over the waveguide region was nearly ideal in both lateral and vertical dimensions,

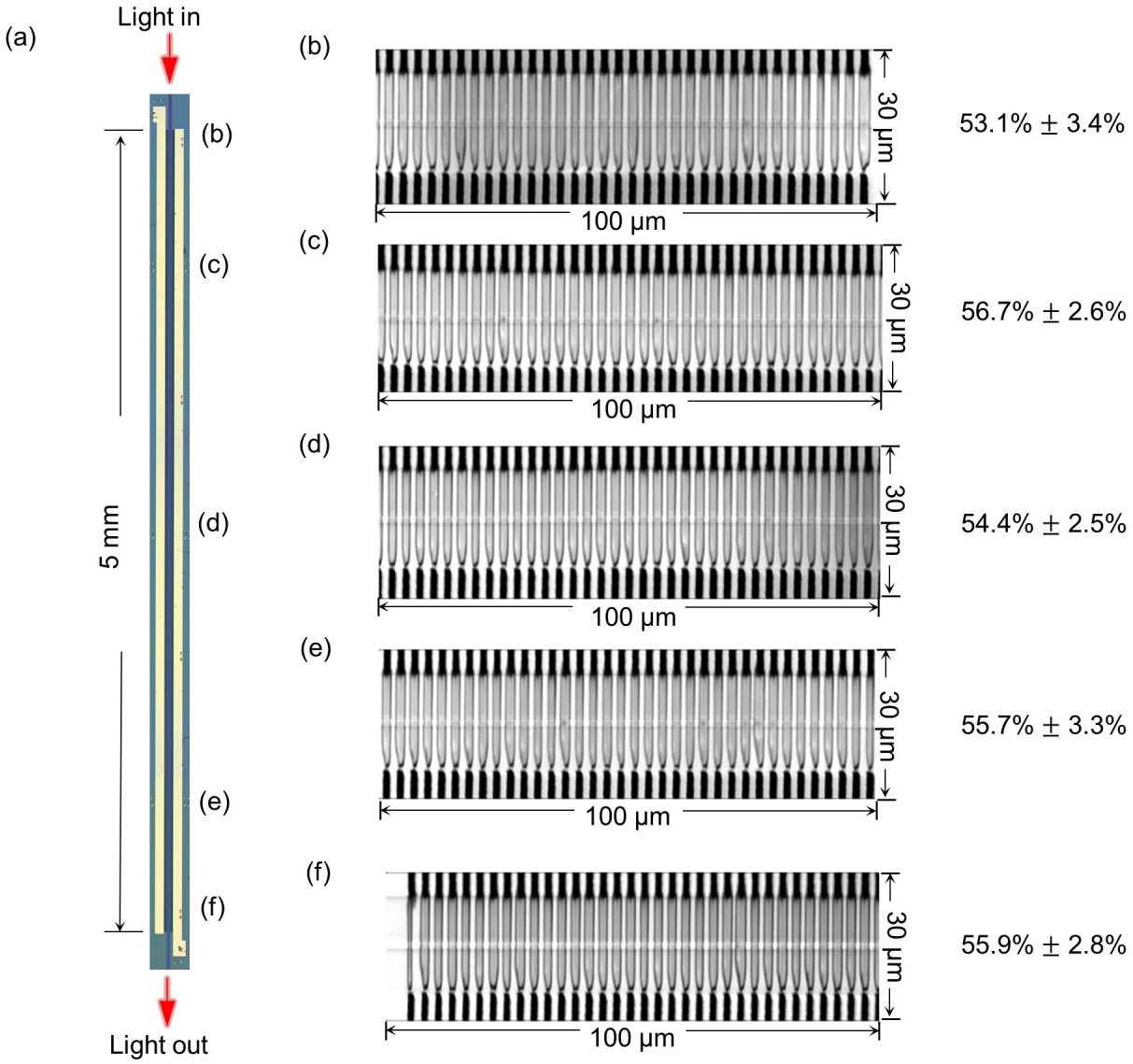

Figure 5.2: (a) Image of the waveguide with poling electrodes. (b)-(f) Second-harmonic images of the inverted domains at the locations indicated in (a), with the calculated poling duty cycles listed on the side. The light gray left-to-right stripe visible in each of the panels is the ridge structure of the waveguide that is formed by shallow etching [see Fig. 5.2(b)]. The image of each panel is rotated clockwise by 90 degrees from the orientation of panel (a).

without either distributed or local errors over the wavelength length that could, for example, cause phase flips in the nonlinear interaction and result in poor SHG performance.

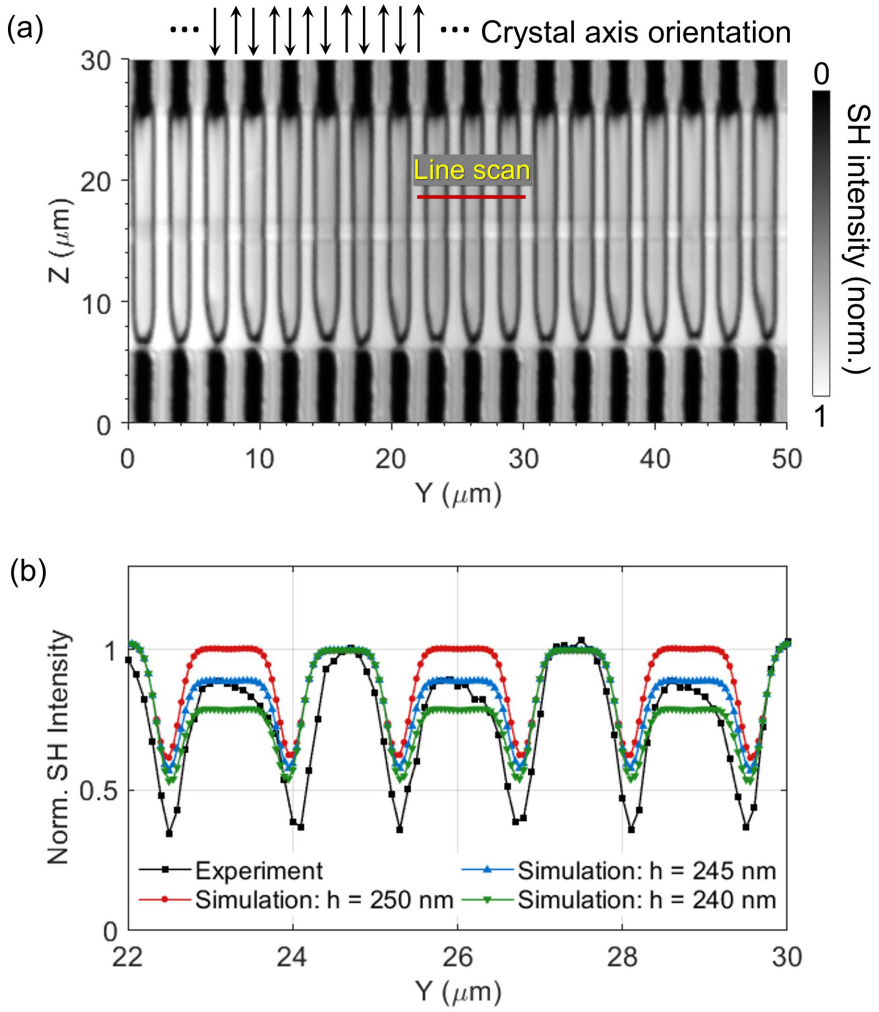

Figure 5.3: (a) High-resolution confocal second-harmonic microscopy of the poled domains from a selected region along the waveguide. (b) Analysis of a typical optical line scan and best-fit comparison with calculated models (three different assumptions about the poling depth h) provides three-dimensional information about the poling profile, with height discrimination of about 5 nm.

5.2 SHG Measurements

As is shown in Fig. 5.4, a continuous-wave telecom-wavelength tunable laser (ANDO AQ4320D) was used as the pump source along with a polarization controller to ensure that the pump light was TE-polarized. Light was coupled in and out of the chip with polarization-maintaining tapered lensed fibers. A 780 nm power sensor together with a power meter was connected to the output tapered lensed fiber to detect and record the generated SH power. The

chip was mounted on a temperature-controlled stage with a thermo-electric controller (TEC) in feedback with a thermistor on the stage mount. The generated off-chip SH power was measured and recorded by a power meter, and the on-chip SH power was calculated using the recorded off-chip power divided by the coupling efficiency. The conversion efficiency was then calculated using Eq. 4.1.

5.2.1 SHG Spectrum

To study the stability of these waveguides as well as the repeatability of the measurements, we measured SHG from this chip over a time period of more than six months. In the initial experiments, the chip was simply diced for measurement, without edge polishing, and thus incurred somewhat high, un-optimized coupling losses to standard, telecom-wavelength, lensed tapered fibers (no index-matching fluid) of -7.7 dB/facet at 1560 nm, and -13.9 dB/facet at 780 nm, estimated based on a $\sim$1.32 μm wide waveguide. In addition to the edge roughness, the high coupling loss at the SH wavelength is dominated by the mode mismatch between the focused fiber mode (mode field diameter: 2.5 μm) and the waveguide mode (effective mode area: $\sim$0.4 μm^2), as well as the propagation loss in the telecom-wavelength fibers. This issue is not uncommon for TFLN waveguides, and can be addressed by edge polishing, adding tapers and edge couplers, and using 780 nm fibers for output coupling [8, 9, 65]. After edge polishing, the coupling loss was -6.7 dB/facet at 1560 nm, and -12.5 dB/facet at 780 nm.

Figure 5.4(b) shows measured SHG spectrum from a 1.14 μm wide waveguide, with a peak η_{norm} of 3757 ± 39 %.W^{-1}.cm^{-2} (peak $\eta = 939 \pm 10$ %.W^{-1}.cm^{-2}). The measured spectrum is overlaid with the calculated curves, using the simulated mode indices and profiles from Lumerical MODE Solutions and Eq. 4.7. The green dashed lines represent the ideal SHG spectra from a lossless waveguide, while the red solid lines plot the corrected spectra considering the measured waveguide propagation losses at both the pump and SH wavelengths. By assuming $\Lambda = 2.81$ μm (compared to the design target of 2.80 μm), the simulated peak wavelength accurately matches

the measured value of the peak wavelength, as shown in Fig. 5.4(b). The measured SHG spectrum of this 1.14 μm wide waveguide shows an otherwise higher peak efficiency than the predicted value, which can be partly attributed to the enhanced pump power in the cavity by the Fabry-Perot resonances, as has been discussed in Ref. [12]. The uncertainty in the measured η_{norm} arises from the fluctuations in the optical power levels from multiple measurements. Note that each SHG spectrum shown below is an averaged result of several measurements. The oscillations in the SHG spectrum are from the Fabry-Perot resonances at both the pump and SH wavelengths, caused by the reflections at the polished waveguide facets. Based on our FDTD simulation, the reflectivity at the pump and SH wavelength is 12.7% and 16.8% respectively, for perfectly smooth waveguide facets. For a lightly polished (with a non-zero roughness) facet fabricated here, the reflectivity should be lower than the theoretical value [154]. Figure 5.4(c) is an image captured by a CCD camera at the output waveguide facet of the 1.14 μm wide waveguide, while the waveguide was pumped with about 0.53 mW power at 1576 nm. The generated on-chip SH power, as is indicated in Fig. 5.4(c) was 2.66 μW (measured power: 150 nW). Comparison of the measured SHG spectrum before and after edge polishing is shown in section A4 in the Appendix.

5.2.2 Second-Harmonic-Pump Power Dependence

Figure 5.5(a) shows the measured and calculated nonlinear conversion efficiency as a function of the pump wavelength from another 1.32 μm wide waveguide at 20 °C. The extracted on-chip normalized conversion efficiency has a peak value of 2658 %.W^{-1}.cm^{-2} at 1553.6 nm. Here, the measured peak efficiency is slightly lower than the theoretical value, which is probably due to the undesired sidelobe at around 1550.7 nm. Poling period (i.e., period of the poling electrodes) and film thickness variations, as well as the un-optimized pump light polarization can result in such sidelobes as seen here. Previously, this has been studied for bulk PPLN [155, 156, 157], and comparable inferences can be made for TFLN as well. For example, the calculated poling period for the highest side peak in Fig. 5.5(a) at 1550.7 nm is 2.805 μm, while that for the

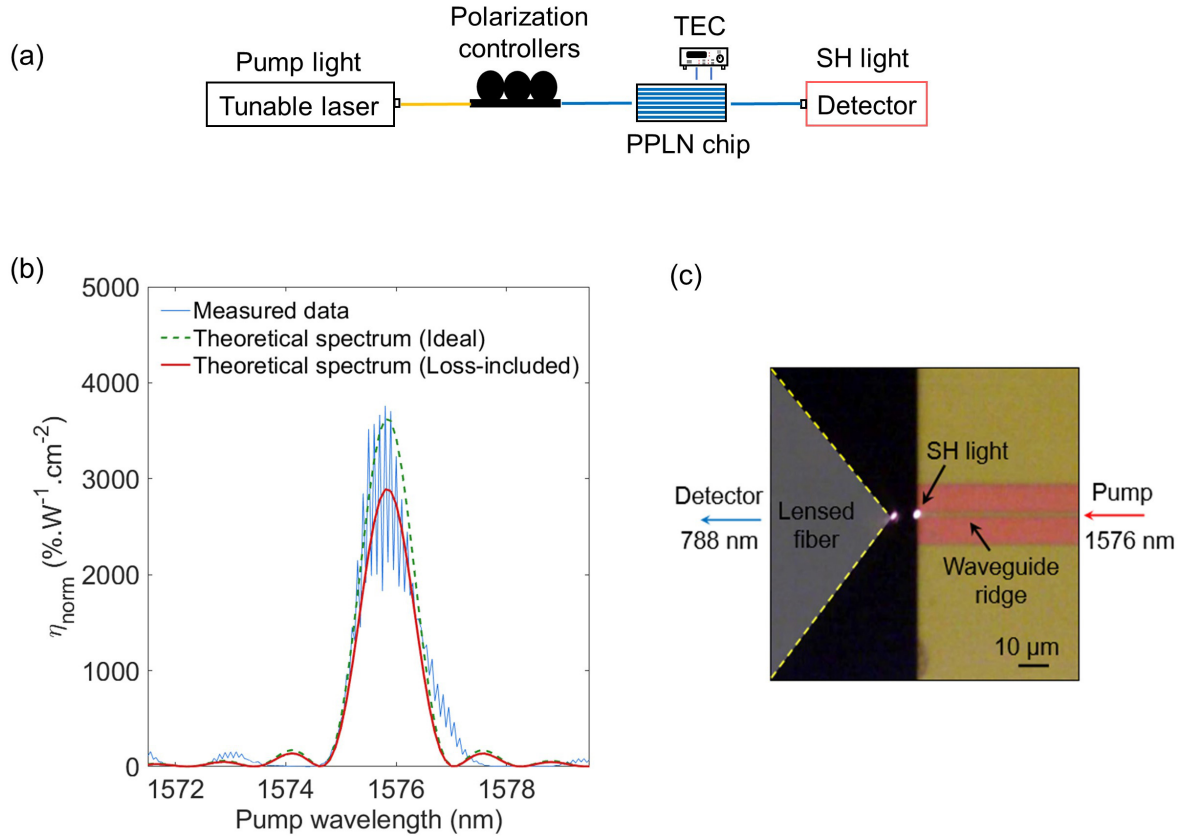

Figure 5.4: (a) Schematic of the experiment for SHG measurement. (b) Measured η (left y-axis) and η_{norm} (right y-axis) as a function of the pump wavelength for a 1.14 μm wide waveguide, after chip edge polishing, overlaid with the theoretical curves. (c) Image captured by a CCD camera at the output waveguide facet, showing the scattered SH light, waveguide and the lensed fiber. The on-chip SH power was 2.66 μW (measured power: 150 nW) at 788 nm, with ∼0.53 mW on-chip pump power at 1576 nm.

central lobe at 1553.6 nm is 2.808 μm, i.e., a shift of only 3 nm. Nevertheless, the full-width at half-maximum (FWHM) spectral bandwidth of the measured spectra are 1.04 nm (1.32 μm) and 1.01 nm (1.14 μm) for the two waveguides, which is almost the same as the theoretical value. This good agreement proves the excellent uniformity of the periodically poled waveguide over the entire poling region. Figure 5.5(b) shows the measured on-chip pump power versus the generated SH power, where the power conversion efficiency reaches 9.4% with the on-chip pump power being 16.7 mW. The black solid line follows $\eta_{norm} L_{NL}^2 P_{pump}^2$, with η_{norm} being 2658 %.W^{-1}.cm^{-2}, while the red dashed line plots the calculated input pump and output SH

power based on the coupled mode equations. Based on Fig. 5.5(b), we see evidence of sub-quadratic scaling at an (on-chip) launched pump power of about 10 mW. At higher pump power, the measured SH power is lower than the quadratic curve, which suggests the onset of pump depletion.

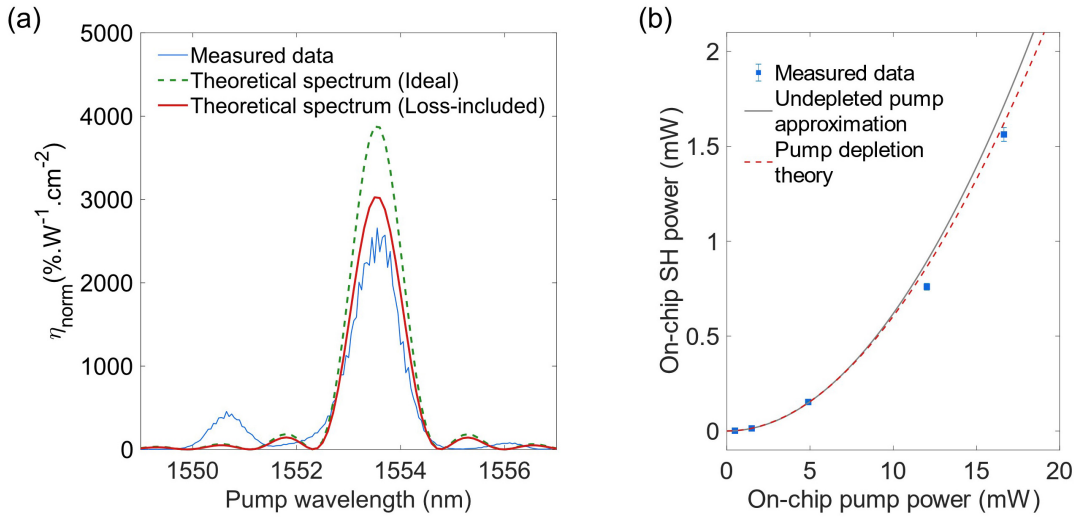

Figure 5.5: (a) Measured η (left y-axis) and η_{norm} (right y-axis) as a function of the pump wavelength for a 1.32 μm wide waveguide, in comparison with the theoretical curves. (b) Measured on-chip pump power versus on-chip SH power at the peak pump wavelength. Errorbars represent one standard deviation in the calculated on-chip SH power from multiple measurements. The solid black line follows $\eta_{norm} L_{NL}^2 P_{pump}^2$ ($\eta_{norm} = 2658$ %.W^{-1}.cm^{-2}). The dashed red line plots the calculated on-chip pump and SH power based on the coupled-mode equations (Eqs. 4.2 and 4.3).

5.3 SHG Spectrum Tuning

To evaluate the tolerance of this shallow-etched waveguide to fabrication errors, we measured the SHG spectra from different waveguides with the width varying from 1060 nm to 1340 nm. Figure 5.6(a) shows the simulated poling period (Λ) versus pump wavelength for waveguides with different widths. In the fabricated device, Λ is fixed at 2.8 μm, which is indicated as a black dashed line in Fig. 5.6(a). Wider waveguides are phase matched at shorter wavelengths. Taking the intersections of the dashed line with the curves shown in Fig. 5.6(a), we

obtained the simulated λ_p as a function of waveguide width, which is shown in Fig. 5.6(b) as blue squares. On the other hand, from the recorded SHG spectra, we can acquire the measured λ_p, which are plotted as the red circles in Fig. 5.6(b). The fitted tuning slope from the measured $[(d\lambda_p).(dw)^{-1} = -0.064]$ and simulated $[(d\lambda_p).(dw)^{-1} = -0.088]$ data agrees well with each other. The measured tuning slope is only -0.064, which is similar to the silicon nitride loaded, unetched TFLN waveguides [12]. This suggests that the shallow-etched waveguides fabricated here manage to have a very high tolerance to fabrication errors that is comparable to the unetched hybrid SiN-TFLN waveguides, and at the same time achieve a higher nonlinear conversion efficiency, taking the advantage of better mode confinement in the etched structures. For this study, the etching depth (h), or the waveguide ridge height is fixed at 50 nm. But we have simulated the peak wavelength shift versus etching depth variation for a 1.2 μm wide waveguide. As is shown in Fig. 5.6(c), the simulated $(d\lambda_p).(dh)^{-1}$ is 2.59.

We have also studied the thermal tuning characteristic of the shallow-etched waveguide by varying the TEC temperature from 20 °C to 60 °C and recorded the SHG spectra, which are plotted in Fig. 5.6(c). As is shown in Fig. 5.6(d), the measured λ_p scales almost linearly with the TEC temperature, and the fitted $(d\lambda_p).(dT)^{-1}$ is about 0.1 nm/°C, which is similar to that of the bulk LN waveguides [158, 156]. The simulated $(d\lambda_p).(dT)^{-1}$ (not shown here) is 0.43 nm/°C, taking into account the temperature and wavelength dependence of the material indices of LN and SiO_2 [159, 160, 161]. This discrepancy may come from the differences in the actual temperature-dependent material properties compared to the assumptions made in the simulation. Same measurements have been performed on this waveguide before edge polishing, more than six months apart, which presented the same tuning slope as shown in Fig. 5.6(d).

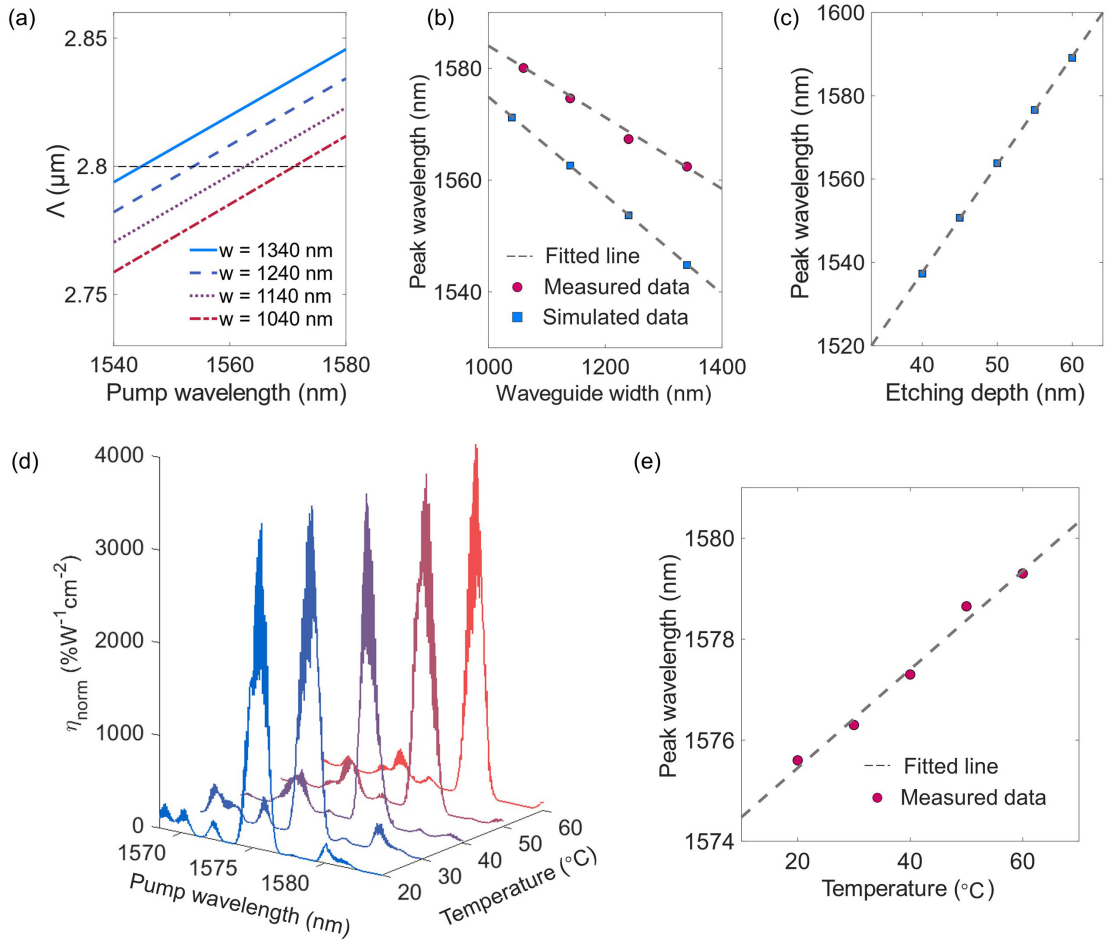

Figure 5.6: (a) Simulated poling period (Λ) as a function of pump wavelength for waveguides with different widths. (b) Measured (red circles) and simulated (blue squares) peak pump wavelength (phase-matched pump wavelength λ_p) versus the waveguide width. (c) Simulated peak pump wavelength (phase-matched pump wavelength λ_p) versus the etching depth. (d)-(e) Measured SHG spectra (d) and λ_p (e) with different TEC temperatures.

5.4 Conclusion

In this chapter, we demonstrate a shallow-etched thin-film MgO:PPLN waveguide structure that achieves the highest (non-length-normalized) conversion efficiency for SHG from telecommunications wavelengths between 1550 nm and 1580 nm to the near-infrared wavelength range of wavelengths between 775 nm and 790 nm. The main achievement is the improvement (see Table 5.1) in non-length-normalized conversion efficiency of periodically-poled TFLN waveguides, which may be considered more promising for making the case for practical and

Table 5.1: Existing works of SHG from LN waveguides, in comparison with the results reported here. λ_p: phase matched pump wavelength. APE: annealed proton exchange. N/A: can not get this information in the paper.

Ref.	Waveguide Type	η_{nor} (%.W^{-1}.cm^{-2})	η (%.W^{-1})	Length (mm)
[57]	APE LN waveguide	150	1634 $^{(a)}$	33
[102]	SiN-TFLN (x-cut)	160	37 $^{(a)}$	4.8
[9]	SiN-TFLN (y-cut)	N/A	N/A	4
[10]	Etched TFLN (x-cut)	2600	416 $^{(a)}$	4
[10]	Etched TFLN (x-cut)	2300	368 $^{(a)}$	4
[12]	SiN-TFLN (x-cut)	1160	267 $^{(a)}$	4.8
[13]	Etched TFLN (x-cut)	4600	4 $^{(a)}$	0.3
[13]	Etched TFLN (x-cut)	2800	10 $^{(a)}$	0.6
This work	Etched TFLN (x-cut)	3757	939	5
This work	Etched TFLN (x-cut)	2658	664	5

Ref.	FWHM (nm)	Maximum output power (on-chip, measured)	Λ (μm)	λ_p (nm)
[57]	0.26 $^{(c)}$	N/A	15.5	1537
[102]	3 $^{(d)}$	0.1 mW	6.6	1530
[9]	N/A	N/A	5	1580
[10]	6.7 $^{(e)}$	117 mW	4.1	1510
[10]	11 $^{(e)}$	N/A	4.1	1620
[12]	2.1	N/A	4.98	1574
[13]	14 $^{(f)}$	0.5 μW $^{(g)}$	2.67	1540
[13]	10 $^{(f)}$	0.6 mW (pulsed) $^{(g)}$	2.67	1540
This work	1.0	2.66 μW	2.8	1575
This work	1.0	1.6 mW	2.8	1554

$^{(a)}$ Calculated by $\eta_{nor}\times$ Length (cm)^2. $^{(b)}$ Information from covesion.com. $^{(c)}$ Estimated from Fig. 2 in the paper. $^{(d)}$ Estimated from Fig. 4(a) in the paper. $^{(e)}$ Estimated from Fig. 3(c) and Fig. 3(b) in the paper respectively. $^{(f)}$ Estimated from Fig. 2(f) and Fig. 2(c) in the paper respectively. $^{(g)}$ Estimated from Fig. 2(g) and Fig. 4(d) in the paper respectively.

realistic device applications of TFLN than high values of only the length-normalized figure of merit. Using confocal scanning second-harmonic microscopy as a non-invasive diagnostic method, we demonstrate successful fabrication of uniformly-inverted domains with a 2.8 μm

period and nearly ideal duty cycle over a 5 mm long region. The efficient and narrow linewidth SHG spectrum can be useful for direct conversion of telecommunications-band signals, which are typically on a 100 GHz (0.8 nm) grid. The thermal-tuning characteristics demonstrated a linear tuning sensitivity of $(d\lambda_p).(dT)^{-1}$ is 0.1 nm/°C, and showed that efficiency was maintained over a temperature swing of up to 40 °C. The shallow-etched waveguide possesses a high tolerance to fabrication errors in width, with a measured $(d\lambda_p).(dw)^{-1}$ being -0.064, which is comparable to what was reported from an unetched hybrid SiN-TFLN waveguide. The results demonstrated here indicate promising applications for robust and efficient waveguide TFLN devices in nonlinear optics in the telecommunications regime. For future potential high power applications, edge couplers could be designed and added to the input and output edges of the chip, to reduce pump power requirements and also to enhance off-chip SH power.

5.5 Acknowledgments

Chapter 5, contains the material as it appears in the following: Jie Zhao, Michael Rüsing, Usman A. Javid, Jingwei Ling, Mingxiao Li, Qiang Lin, and Shayan Mookherjea, "Shallow-etched thin-film lithium niobate waveguides for highly-efficient second-harmonic generation", Optics Express 28(13), 19669 (2020). The dissertation author, together with her adviser, led the research efforts for this work and co-authored the paper.

Chapter 6

Entangled Photon-Pair Generation

6.1 Spontaneous Parametric Down Conversion

Integrated photonics can be useful in generating, manipulating and detecting non-classical light, including photon pairs and heralded single photons as resources for quantum optical communications and information processing. Compared to bulk nonlinear optical crystals, the use of waveguides and periodic poling has led to significant improvements in brightness, quality and simplicity of near-infrared wavelength photon pair sources [162]. For photon pair generation using nonlinear optical processes (e.g., SPDC, or spontaneous four-wave mixing, SFWM), the intrinsic rate of nonlinear optical processes increases as the cross-sectional area of the waveguide mode decreases. Generally, sub-micron modal area (i.e., $A_{\text{eff}} \leq 1\ \mu\text{m}^2$) waveguides are associated with high-index contrast silicon photonics, in which SFWM generates a reasonably high rate of photon pair generation at sub-milliwatt pump power levels [163].

The performance of LNOI based devices can be superior to that of traditional LN waveguide devices; one notable example is that of $>$100 GHz bandwidth electro-optic modulators [56, 61]. However, the reported SPDC performance of LNOI [164, 165, 166, 11] in terms of the usual metrics such as Coincidences-to-Accidentals Ratio (CAR) and condi-

tional self-correlation [$g^{(2)}(0)$] has yet to catch up to SPDC in traditional LN waveguides, where coincidences-to-accidentals ratio CAR $> 10,000$, heralded two-photon auto-correlation $g^{(2)}(0) < 0.01$, and two-photon interferometric visibility $V \approx 99\%$ are common.

The objective of this chapter is to report good performance achieved using SPDC in a periodically-poled thin-film lithium niobate (LN) waveguide. As is shown in Fig. 6.1(a), SPDC can be seen as the reverse process as SHG, where one photon with higher energy (about 785 nm in our experiment) spontaneously splits into two daughter photons with lower energy (about 1570 nm), conforming the laws of energy and momentum conservation. Measurements shown in the following sections are from a 1.24 μm wide shallow-etched PPLN waveguide, whose fabrication method has been discussed in detail in the previous chapter. The quasi-TE-polarized fundamental modes, shown in Figs. 6.1(b) and 6.1(c), were calculated using Lumerical MODE Solutions to have modal effective area $A_{\text{eff}} = 1.1\ \mu\text{m}^2$ at 1570 nm wavelength, and $A_{\text{eff}} = 0.4\ \mu\text{m}^2$ at 785 nm wavelength. The poling duty cycle is estimated as $55.2\% \pm 3.0\%$, based on the SH images generated from five different positions along the waveguide, each with an area of 100 μm (along the y-axis) $\times$ 30 μm (along the z-axis), as is shown in Fig. 5.2.

6.2 SPDC Measurements

Typical characterization measurements for SPDC report pair generation rates and two-photon correlation measurements, quantifying the pair generation and heralding properties of the source. Since the purpose of this paper is to demonstrate that high-quality pairs can be experimentally generated using LNOI waveguides, we focus mainly on the low pump-power case; nevertheless, an appreciable rate of pairs and single photons was measured because of the high brightness of the source.

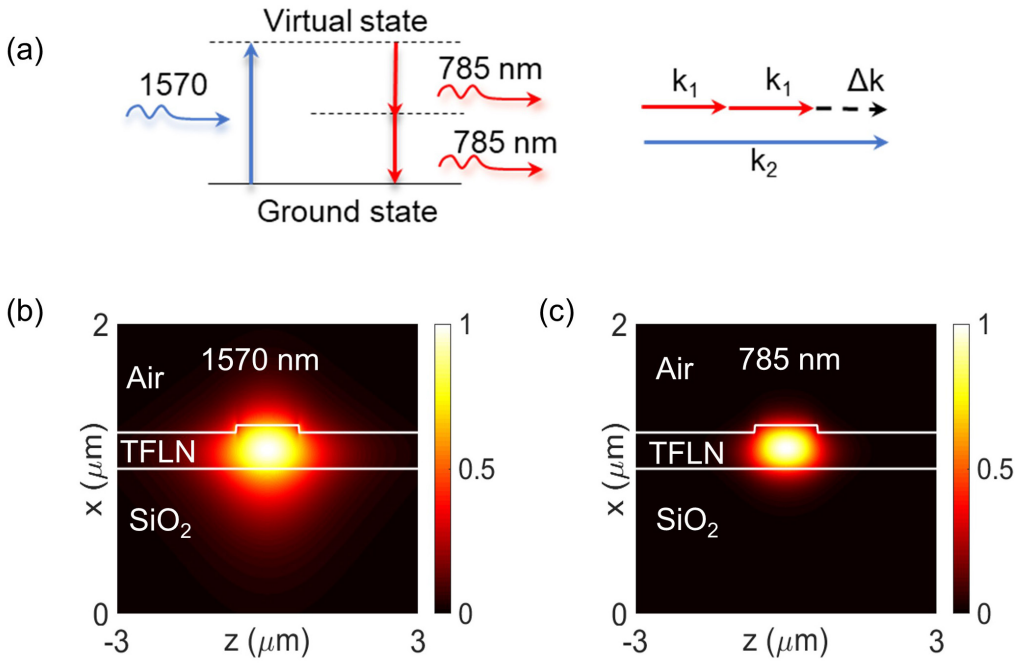

Figure 6.1: (a) Schematic illustration of the SPDC process. (b) Calculated profile (magnitude of the major electric-field component) of the quasi-TE-polarized fundamental mode at 1570 nm for the down-converted photons. (c) Calculated profile of the quasi-TE-polarized mode at 785 nm for the pump of the SPDC process.

6.2.1 Optical Characterization

Confirmation of the QPM grating was poled correctly was obtained from a conventional waveguide SHG experiment, using as input a tunable-wavelength, continuous-wave pump around 1569 nm. The converted power around 784.5 nm was measured when tuning the wavelength of the pump light, with the chip temperature maintained at 63 °C. By fitting the central lobe of the measured SHG spectrum to a sinc-squared functional form, we measured a high SHG conversion efficiency of 425 $\%.\mathrm{W}^{-1}$, with a full-width at half-maximum (FWHM) spectral bandwidth of 1.13 nm. Calculations of the SHG spectrum considering the measured propagation losses indicate that the predicted FWHM bandwidth is 1.14 nm. This relatively narrow bandwidth (e.g., compared to Refs. [8, 10]) enables the main peak to be filtered out by a standard telecommunications grade filter for SPDC. From the measured classical SHG results, the quantum SPDC properties can be estimated, upon making an assumption of the filter bandwidth (here, taken as 100 GHz, as

representative of the experiment) and the pump power (taken as 0.1 mW). Assuming quadratic scaling with length, the predicted pair generation rate is about 5.2 MHz. In practice, the SPDC length scaling may be closer to $L^{3/2}$ because of dispersion [167] and result in a slightly lower pair rate, as seen in Fig. 6.2.

The bare-die chip was mounted on a temperature-controlled stage with a thermo-electric controller (TEC) in feedback with a thermistor on the stage mount. The chip was maintained at a temperature of 63 °C in order to tune the QPM peak to the input laser wavelength. Light was coupled to and from the chip using lensed tapered polarization-maintaining fibers designed for 1550 nm. The chip was simply diced for measurement, without polishing of the end facets, and thus incurred high, un-optimized coupling losses of -7 dB/facet at 1570 nm and -15 dB/facet at 785 nm. Loss values of -3 dB/facet at 1570 nm and -6.6 dB/facet at 785 nm can be simply attributed to mode-overlap mismatch between the tapered fiber and the waveguide modes as calculated by optical simulation software, with the rest attributed to excess loss due to roughness or launch at 785 nm into an higher-order waveguide mode that is not phase-matched. The propagation loss of the waveguides was estimated to be -0.54 dB/cm at around 1569 nm, and -3.21 dB/cm at around 785 nm using the cutback method performed on several waveguides with different lengths.

Output light from the chip was routed through a cascade of two filters, where the first was a pump-reject filter, consisting of a tabletop assembly of a long-pass, free-space filter with two fiber collimators, and the second was a fiber-coupled, off-the-shelf, telecommunications-grade optical filter centered around 1568.9 nm with bandwidth 0.8 nm. The insertion loss of the filter cascade at the wavelengths of interest was less than -4 dB and the pump rejection should be greater than 150 dB. The filter assembly was followed by a 50%-50% splitter. For frequency-degenerate photon pairs incident on the splitter, both photons end up in the same detector one-half of the time, and would not be counted as a coincidence by the TDC. An imperfect splitting ratio resulted in a slight difference in the measured singles rates of the signal and idler channels. The spectral width of the QPM curve was approximately similar to the pass-band width of the filter; thus,

filtering does not reduce the flux rate or brightness of the photon pairs by much.

Photons were detected using fiber-coupled superconducting nanowire single photon detectors (SNSPD), cooled to 0.8 K in a closed-cycle Helium-4 cryostat equipped with a sorption stage. The detection efficiencies of two of the SNSPD's were about 68% and, for one of the detectors, was about 90%; these detectors were not gated and were operated in a simple dc-biased mode with an RF-amplified readout. Detected signals were processed using a time-to-digital converter (TDC) instrument, with coincidence window of 15 ns or 10 ns. The CAR metric can be inflated by un-naturally narrowing the coincidence window, e.g., less than the timing jitter of the detectors [168]. This is clearly not the case here. The coincidence window is much wider than the values of typical timing jitters for both SNSPD and InGaAs SPAD detectors at 1550 nm. Singles and coincidences due to dark counts were measured separately, but since their contribution was seen to be negligible, they were not subtracted from the measurements. Each histogram peak was fitted by a Gaussian function, whose FWHM was measured to be typically 27 ps.

6.2.2 Pair Coincidence Rate

The fabricated waveguide was tested for its properties as a source of optically-pumped entangled photon pairs and heralded single photon generation. The experimental apparatus is described in and in Fig. 6.2(a). The on-chip pair flux or coincidence rate, which is abbreviated in the figure labels as the pair coincidence rate (PCR), was calculated by dividing the time-averaged value of the measured coincidence rate, N_{SI}, by the edge coupling efficiency of the chip, the transmission of the filters, and the detector efficiencies. These quantities were measured by separate calibration measurements. As a check, this value of PCR is equal, within the limits of experimental accuracy, to the value calculated as $\mathrm{PCR} = \langle (N_{\mathrm{S}} N_{\mathrm{I}})/(2N_{\mathrm{SI}}) \rangle$, where $N_{\mathrm{S,I}}$ are the as-measured, time-varying singles rates of the signal and idler photon detection events, respectively, and N_{SI} is the rate of the signal-idler coincidence detection events, and $\langle\rangle$ denotes a time-average over the entire acquisition period. The factor of 2 in the denominator is because of the beam

splitter in the experimental configuration. We calculated PCR for several different values of the input pump power and Figure 4(a) plots the result and the fitted line. The slope of PCR with pump power is 45 MHz.mW^{-1}, which is higher than that of a typical value for a state-of-the-art traditional PPLN waveguide of 14 MHz.mW^{-1} [169].

Dividing further by the FWHM of the filter used before the single-photon detectors, $\Delta\lambda = 0.8$ nm (100 GHz), we calculate the brightness of our pair source to be $B = 2.9 \times 10^7$ pairs.s^{-1}.nm^{-1}.mW^{-1}, or $B = 3 \times 10^5$ pairs.s^{-1}.GHz^{-1}.mW^{-1}, depending on the units used for the bandwidth. It is interesting to compare the performance with SFWM devices: because of the weaker third-order nonlinearity of SFWM compared to SPDC, the high-brightness results are achieved using micro-resonators, for which a list of recent results is tabulated in Ref. [170]. Among record results, a silicon microring SFWM pair source [30] achieved a brightness of $B = 1.5 \times 10^8$ pairs.s^{-1}.GHz^{-1}.mW^{-2} and a similar value, within a factor of two, was achieved in a silicon microdisk resonator [171]. Note that although the brightness of these SFWM sources is about three orders of magnitude higher than that of the SPDC source reported here, a significant factor is because the FWHM of the silicon microresonator's resonance (2.1 GHz) is much narrower than the FWHM of the LN waveguide's QPM peak (approximately 160 GHz), and plays a significant role in determining the brightness. An example of resonant enhancement for bright SPDC pair generation is provided by Ref. [172], for PPKTP rather than PPLN, which achieved a singles-rate brightness of $B = 1.4 \times 10^7$ counts.s^{-1}.GHz^{-1}.mW^{-1}. However, an efficient waveguide device is typically easier to use in practice than a high-Q resonant device, as long as the PGR and metrics describing the quality of the generated photons are high.

6.2.3 Coincidences to Accidentals Ratio

Achieving high CAR depends on low detector noise, suppression of pump and scattering noise, improvement of the stability of pair generation, and improving factors such as loss in the device and the experimental setup, which lead to broken pairs and increase the rate of accidental

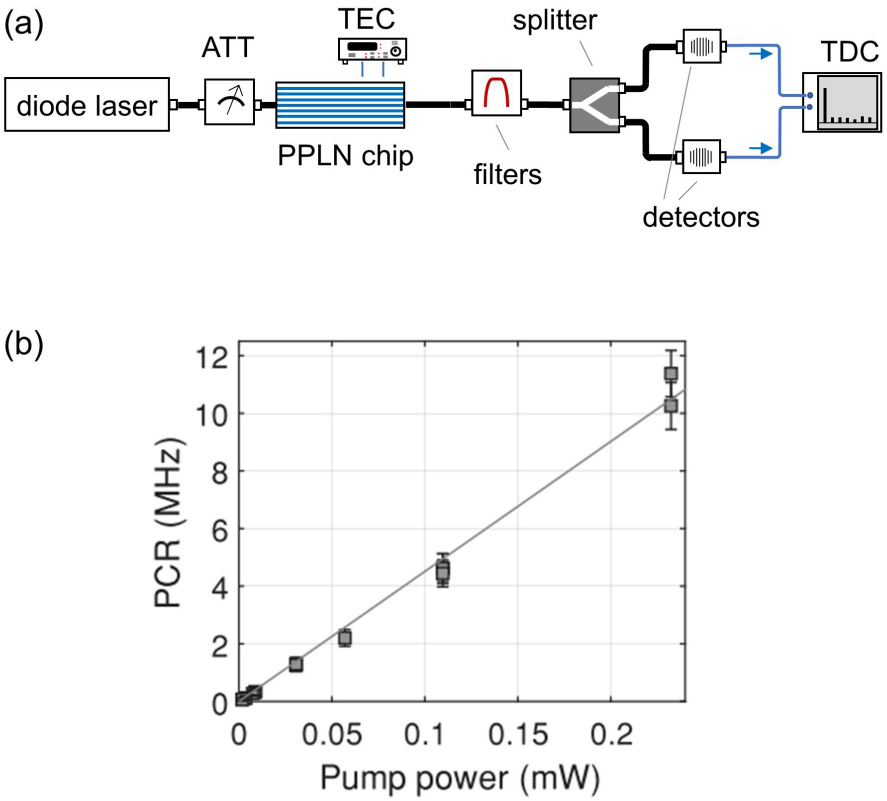

Figure 6.2: (a) Schematic of the experiment to characterize frequency-degenerate photon-pair generation, and measure the coincidences to accidentals ratio. ATT: Variable attenuator. TEC: Thermo-electric controller. TDC: time to digital converter. DLI: Delay line interferometer. (b) Measured pair coincidence rate (PCR, units: MHz) versus pump power (units: mW) in the waveguide.

coincidences. Figure 6.3(a) shows the measurements of the CAR versus the (on-chip) coincidence rate. The CAR was calculated as $\mathrm{CAR} = \max[g^{(2)}_{\mathrm{SI}}(t)] - 1$ from the normalized signal-idler cross-correlation, $g^{(2)}_{\mathrm{SI}}(t)$, which was obtained from the histogram of signal-idler coincidences that was measured by the TDC instrument as a function of the delay t between the two channels. The histograms were acquired in start-stop mode for a measurement time T that varied between 120 s and 480 s (at lower power), and a coincidence window $W = 15$ ns. It was verified that each coincidence peak was well fit by a Gaussian function, whose FWHM was 25.2 ± 0.4 ps across all the datasets reported in Fig. 6.3(b). The value of CAR reported here is obtained from the amplitude of the fitted peak, which is slightly less than the raw measured value of $\max[g^{(2)}_{\mathrm{SI}}(t)]$.

The highest CAR was $67,224 \pm 714$ measured when the PCR was $7.6 \pm 2.6 \times 10^4$ pairs.s^{-1} (detected pair flux: 24 ± 8 pairs.s^{-1}). At the highest power values used here, CAR = 668 ± 1.7, at PCR = $11.4 \pm 0.4 \times 10^6$ pairs.s^{-1} (detected pair flux: $3.6 \pm 0.3 \times 10^3$ pairs.s^{-1}). CAR decreased at higher pump powers and thus, at higher PGR, as expected, following the trend line CAR $\propto$ PGR^{-1}, as shown in Fig. 6.3(a).

These numbers are significantly higher than those achieved other integrated photonics platform at 1550 nm wavelengths, including silicon [30] and silicon nitride [173], measured using similar experiments and apparatus. Compared to traditional PPLN waveguides, the highest reported value (to our knowledge) of CAR is 8×10^5 measured, however, at PCR of only 5 pairs.s^{-1} [174]; in comparison, the product of CAR and pair flux is about three orders-of-magnitude higher in our LNOI waveguides, highlighting the efficiency of nanoscale LN waveguides with good QPM properties in generating high-quality photon pairs.

6.2.4 Heralded Single-Photon Generation

Detecting one photon of the pair results in a heralded single-photon source, since the other photon is expected to show non-classical anti-bunching behavior. This waveguide supports a single propagating mode at the down-converted wavelengths near 1.57 μm wavelengths, and, after filtering, the central QPM peak is fairly narrow. Therefore, in contrast to SPDC in bulk crystals, the signal and idler photons are emitted into a pair of discrete, well-defined modes which propagate collinearly. Here, as stated earlier, the width of the QPM peak is approximately the same as that of the passband of the filter for the signal and idler photons. We have not yet measured the two-photon joint spectrum, and thus cannot conclude that the heralded photon is actually in a pure single-photon Fock state. Accordingly, the discussion for the present is restricted to the measurement of the second-order correlation function of the heralded photon, i.e., a characterization of anti-bunching.

Figure 6.4 shows the heralded (i.e., conditional) single-photon second-order self-correlation

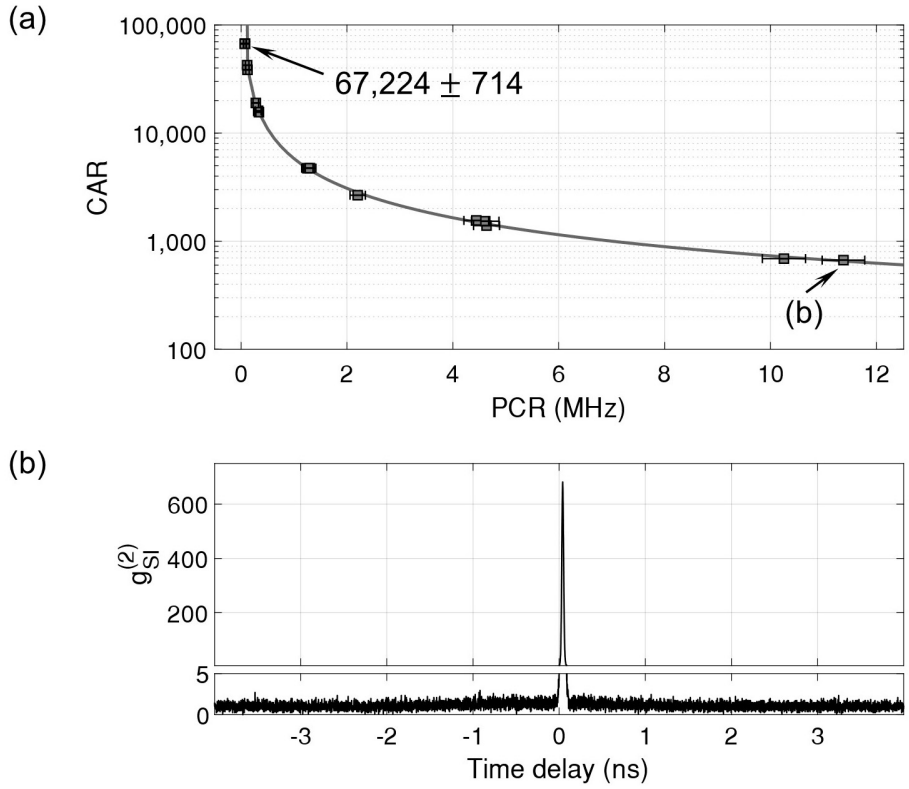

Figure 6.3: (a) Coincidences-to-Accidentals Ratio (CAR) versus PCR. The highest measured value is indicated. The error bars are one standard deviation in each direction (vertical error bars are too small to visualize at this scale). (b) The signal-idler cross-correlation counting histogram for the lowest CAR value. The full-width at half-maximum of the central peak was 27 ps.

function, $g_H^{(2)}(0)$, obtained by detecting one of the generated photon pair as a herald, and measuring the self-correlation of the other photon in the presence of the herald. The normalized value of the photon correlation measurement on the heralded single photons at zero time delay was calculated using the formula [175] $g_H^{(2)}(0) = N_{ABC}N_A.(2N_{AB}N_{AC})^{-1}$, where N_A is the average photon detection rate on the heralding SNSPD detector [labels are shown in Fig. 6.4(a)], double coincidences N_{AB} and N_{AC} correspond to average rates of simultaneous events on one of the detectors (B or C) and the heralding SNSPD detector (A), and triple coincidences N_{ABC} correspond to average rates of simultaneous events on all three detectors. This parameter has also been called the anti-correlation parameter.[176] Note that $g_H^{(2)}(0)$ can also be written in terms of the probability of observing a single photon in the signal arm and the probability of observing

two photons in the signal arm, $g_H^{(2)}(0) = 2N_A N_{ABC}.(N_{AB}+N_{AC})^{-2}$, where the factor of 2 in the numerator comes from the splitting ratio of the beamsplitter [177].

Double and triple coincidences were defined as simultaneous detections within a 10 ns time window, measured directly by the TDC hardware (calculating coincidences between combinations of input channels without software post-selection). Counting times were 200 seconds (with 1000 seconds for one point as a check).

Even at the highest power values used in this sequence of measurements, $g_H^{(2)}(0) = 0.183 \pm 0.03$, well below the classical threshold, at an on-chip (i.e., inferred) heralding rate of $N_A = 4.2$ MHz (raw measured herald rate 107 kHz). At lower pump powers, values as low as $g_H^{(2)}(0) = 0.022 \pm 0.004$ were directly measured (the errorbar is one standard deviation uncertainty), for an on-chip heralding rate of $N_A = 0.7$ MHz (raw measured herald rate 15 kHz). There have not been previous reports of heralded single-photon generation using LNOI waveguides or resonant devices. For comparison with traditional PPLN devices, $g_{\mathrm{H}}^{(2)}(0) = 0.023$ has been measured at $N_{\mathrm{H}} = 2.1$ MHz [178], and $g_{\mathrm{H}}^{(2)}(0) = 0.005$ has been measured at (detected) $N_{\mathrm{H}} = 10$ kHz [179].

The heralding (Klyshko) efficiency, defined as $N_{AB}/(N_A \times D)$ where D is the detection efficiency of the heralded photon, was calculated to be between 1.3% and 2% for raw (off-chip) values of the rates. The main reason for the low efficiency of the off-chip efficiency is loss: the sum of the fiber-to-waveguide loss and the insertion loss of the filters is about -14 dB for each of the SPDC-generated photons in the current device and experimental configuration, whereas, for example, the coupling efficiency to fiber in Ref. [178] was estimated to be about 60% and the equivalent transmission efficiency through free space was above 90% in Ref. [180]. Since the ratio of the on-chip pair rate to the on-chip singles rate (averaged between the signal and the idler) exceeds 52%, we expect heralding efficiencies comparable to established PPLN technology upon improvements in the coupling from these LNOI waveguides to detectors through fibers or free space.

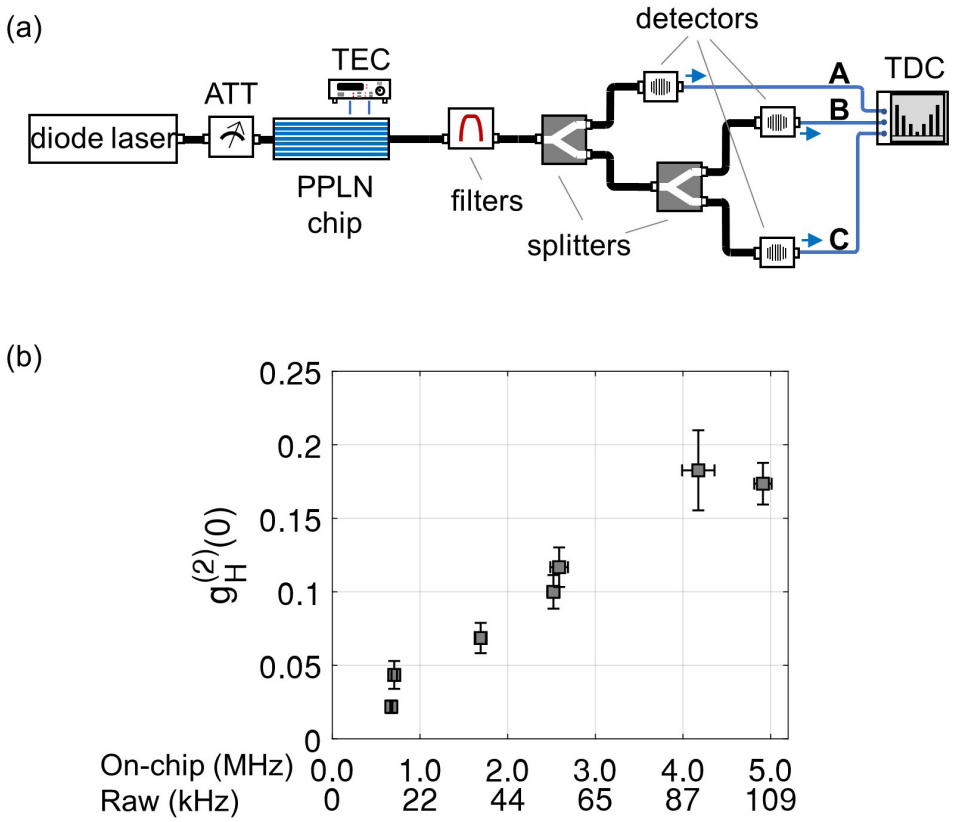

Figure 6.4: (a) Schematic of the experiment to measure heralded single photon detection. (b) Heralded single photon generation. Conditional self-correlation (heralded auto-correlation) $g^{(2)}_{\mathrm{H}}(0)$. The horizontal axis shows both the raw herald rate (kHz) and on-chip singles rate (MHz); the latter is obtained by dividing by the measured losses between the chip and the detector. The error bars are one standard deviation. The lowest measured $g^{(2)}_{\mathrm{H}}(0)$ was 0.022 ± 0.004.

6.2.5 Energy-Time Entanglement

The generated photon pair is expected to demonstrate energy-time entanglement which can be investigated through a Franson-type two-photon interference experiment, by violating Bell's inequality [181, 182]. Figure 6.5 shows the measurement of visibility fringes using an unfolded Franson interferometer configuration, whose schematic is shown in Fig. 6.5(a). Down-converted photons are split and input into two separate delay line interferometers (DLI's) in which the phase (delay) can be controlled, and the outputs of the DLI's are sent to single-photon detectors. In each DLI, a photon (labeled '1' or '2') can take two equally-probable paths, short

(S) or long (L), leading to four possible scenarios for the coincidence events measured at the TCSPC: $|S_1L_2\rangle$, $|S_1S_2\rangle$, $|L_1L_2\rangle$, and $|L_1S_2\rangle$. In the case of $|S_1L_2\rangle$ and $|L_1S_2\rangle$, since the two photons have acquired a relative time lag larger than the two-photon correlation time, they are distinguishable from each other as well as from $|S_1S_2\rangle$ and $|L_1L_2\rangle$; thus, there are three distinct peaks in the histogram of counts. For the remaining two processes, the intrinsic uncertainty in the emission time of a photon pair makes them indistinguishable from each other. The bi-photon state $|\Psi\rangle$ reaching the detectors is therefore $|\Psi\rangle = \frac{1}{\sqrt{2}}\left(|S_1S_2\rangle + |L_1L_2\rangle\right) = \frac{1}{\sqrt{2}}\left(|S_1S_2\rangle + e^{i\Phi}|S_1S_2\rangle\right)$, where $\Phi = \phi_1 + \phi_2$, with ϕ_1 and ϕ_2 being the phases of the two DLI's. During the measurements of visibility, one of the DLI's is scanned, whereas the other DLI is held stationary. The associated coincidence rate should exhibit an interference pattern, which should go from constructive to destructive for a phase change $\Delta\Phi = \pi$, as verified in Fig. 5 for two different static settings of the second DLI.

Two fiber-coupled, polarization-maintaining, piezo-controlled delay-line interferometers (DLI's), each with an FSR of 2.5 GHz and peak-to-valley extinction ratio approximately 25 dB were used in these measurements. Data scatter in the fringes was caused by fluctuations of photon pair flux coupled to the DLI's, which was mainly a result of a drift in the state of polarization or variations in fiber-to-chip alignment. However, this effect is minor and negligible compared to the expected variations, with relative phase, in the two-photon coincidence counts. The raw measured coincidences showed three peaks, as shown in typical data plotted in Fig. 6.5(b). In each case, a Gaussian function was seen to be a good fit to the raw data, and the peaks were clearly separated, leading to a simple and robust fit. The fitting uncertainty (one standard deviation) is shown as the errorbar in the plotted points and is too small to be visible. The phase of one of the DLI's (i.e., the phase delay between the short arm and the long arm of that DLI) was held constant at two different settings, and the phase of the other DLI was swept over approximately one free spectral range, tuned by voltage. In Fig. 6.5(c), the normalized coincidence counts were calculated by dividing the raw measured counts (which varied from about 0.37 to 189 counts in

the measurement time) by the product of the singles counts during the same time; this normalized quantity factors out the minor variations in the singles counts with time also shown in Fig. 6.5(c). The flat singles rates (versus phase) show the absence of single-photon interference, as desired.

Proof of photon pair entanglement requires a two-photon interference pattern fringe visibility $V \geq 70.7\%$ (without necessarily providing a test of local realism) [183]. The fitted measurements showed V clearly in excess of this threshold value, measured when the on-chip PGR was about 235 kHz, as inferred from the recorded singles rates and the coupling losses. Previously, a CAR measurement was performed at a similar PGR, and this is recorded in Table 6.1 alongside the V values. From the raw data, i.e., the highest and lowest value in Fig. 6.5(c), we calculated $V_{\text{data}} = 99.3 \pm 1.9\%$ (data points shown in blue) and $V_{\text{data}} = 99.5 \pm 1.8\%$ (data points shown in black) for the two phase settings of the unfolded Franson configuration. The indicated errorbar is the uncertainty which arises from the goodness-of-fit of the parameters of the Gaussian function used to fit the central peak; in many cases, the size of the errorbar is too small to be visible. From a fit to the entire ensemble of measurements based on the non-linear least-square curve fitting algorithm in Matlab, we obtained $V_{\text{fit}} = 98.4\%$ and $V_{\text{fit}} = 96.4\%$ for the two cases. These measurements confirmed the energy-time entanglement properties of the pairs, as shown by the sinusoidal variation of coincidences with phase.

6.3 Generation of Heralded Single-Photon States

The bi-photon state $|1\rangle_1|1\rangle_2$ generated by SPDC in a waveguide of length L is [28]

$$|\psi\rangle \propto \iint d\omega_1\, d\omega_2\, \Phi(\omega_1+\omega_2)\phi_{\text{PM}}(\omega_1,\omega_2)\; |1\rangle_1|1\rangle_2 \tag{6.1}$$

where Φ is the pump spectral envelope (typically taken as a Gaussian function) and ϕ_{PM} is the phase matching function which can be written as $\phi_{\text{PM}} = \text{sinc}(\Delta kL/2)$ where L is the length of the waveguide and Δk is the effective wave-vector mismatch, i.e., the residual deviation from

Table 6.1: Recent results of entangled photon-pair and heralded single-photon generation near 1.55 μm wavelengths using optically-pumped SPDC in TFLN photonic devices, in comparison with our results. Values indicated in **bold** are record values reported for thin-film LN SPDC devices. The quality is defined by the pair flux or pair coincidence rate (PCR), coincidences-to-accidentals ratio (CAR), heralded second-order autocorrelation at zero-time difference [$g_H^{(2)}(0)$] for a heralded single photon, and the two-photon interference visibility of the photon pair [V].

Ref.	Structure	PCR	CAR	$g_H^{(2)}(0)$	Visibility
[184]	waveguide	[theory]	-	-	-
[164]	microdisk	450 kHz	$6^{(a)}$	-	-
[165]	microdisk	0.5 Hz$^{(b)}$	43	-	-
[166]	waveguide	7 kHz$^{(c)}$	15	-	-
”	”	28 kHz$^{(c)}$	6	-	-
[11]	waveguide	0.8 MHz$^{(d)}$	631 ± 210	-	-
”	”	7.2 MHz$^{(e)}$	$23^{(f)}$	-	-
[185]	waveguide	36 kHz$^{(g)}$	$6,900 \pm 200$	-	
This work	waveguide	60 kHz	**67,224 ± 714**	-	-
”	”	598 kHz$^{(h)}$	7,501$^{(i)}$	**0.022 ± 0.004**	-
”	”	890 kHz$^{(h)}$	5,210$^{(i)}$	-	**99.3 ± 1.9** % **99.5 ± 1.8** %
”	”	3.7 MHz$^{(h)}$	1,427$^{(i)}$	0.183 ± 0.03	-
”	”	**9.0 MHz**	668 ± 1.7	-	-

$^{(a)}$Estimated from the peak-to-side-lobe (± 0.5 ns) ratio of coincidence counts. $^{(b)}$Peak value of the raw coincidence counts divided by the measurement time, and further divided by the detection efficiency and detector gating duty cycle. $^{(c)}$From the stated pump power and on-chip pair generation rate. $^{(d)}$From the stated pair generation rate. $^{(e),(f)}$Estimated from Figs. 5(a) and 5(b) in Ref. [11]. $^{(g)}$Estimated from the product of the stated values of the loss-corrected normalized brightness, bandwidth, waveguide length and the loss-corrected pump power. $^{(h)}$Estimated from the measured singles rate. $^{(i)}$From the fitted line in Fig. 6.3(b) at the estimated PCR.

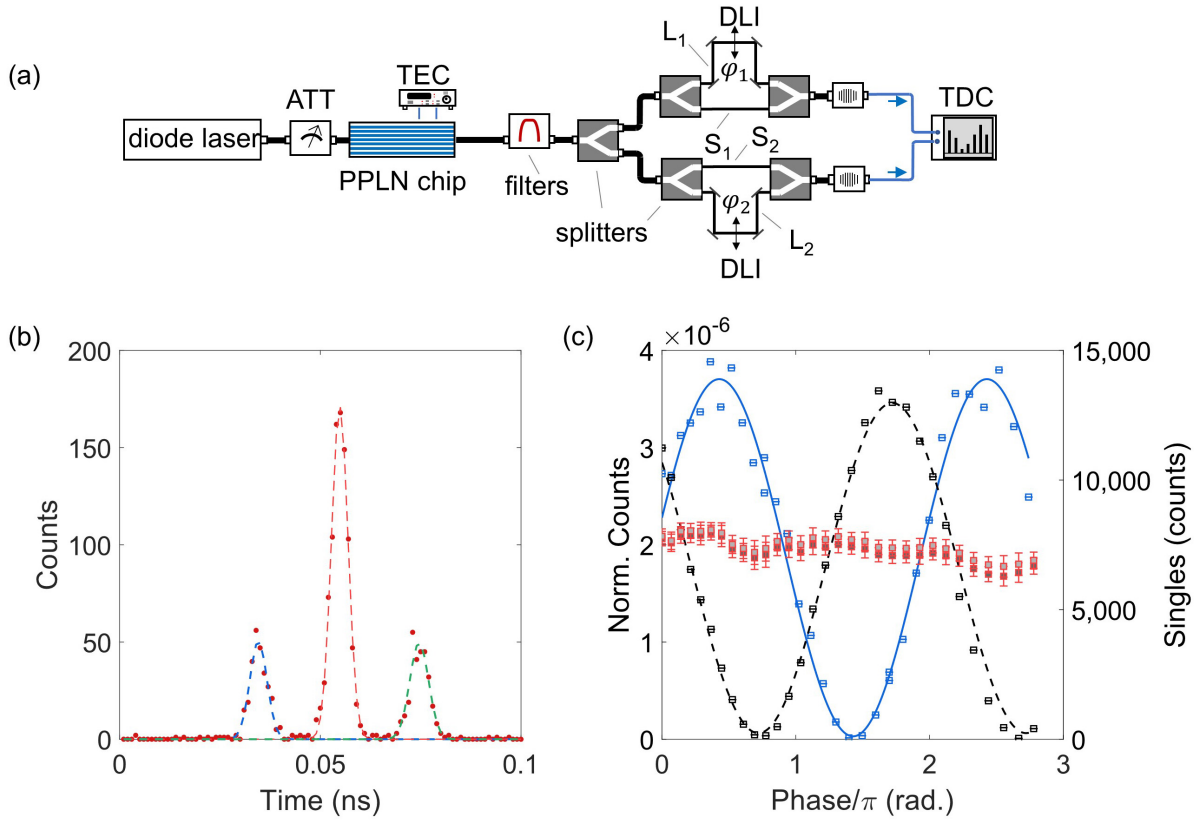

Figure 6.5: (a) Schematic of the experiment to measure energy-time entanglement using a Franson interferometer. (b) Representative histogram for the measurement of energy-time entanglement, at a particular phase setting of the delay line interferometers (DLI's). (c) Two-photon interference pattern measured as the phase of one DLI is swept. The interference pattern for two different phase settings on the second DLI are shown. Black and blue dots (with errorbars): experimental data, black solid and dashed lines: sinusoidal fit. The right-hand side axis shows the singles counts averaged over the acquisition time, measured at the same time as the two-photon coincidences.

perfect phase matching, $\Delta k = k_P - k_1 - k_2 - (2\pi/\Lambda)$, in terms of the wavenumbers at the pump wavelength (k_P), the wavelengths of the generated photons (k_1 and k_2) and the period of the first-order QPM grating, Λ. The normalization constants include factors of L and $(2/\pi)$ to account, respectively, for the integral defining the phase matching function and the reduction in the efficiency of QPM versus perfect phase matching.

The functions Φ and ϕ_{PM}, and the resulting joint spectral intensity (JSI) are shown in Fig. 6.6 as functions of the optical frequency $\nu = \omega/(2\pi)$ around the phase-matched point. The

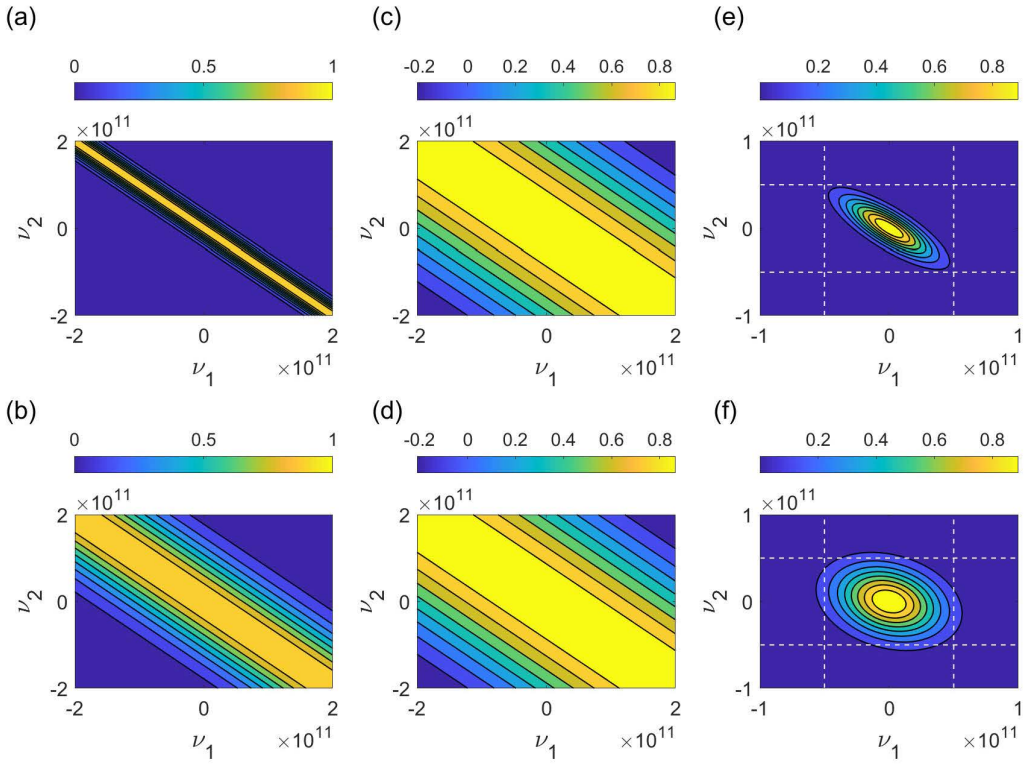

Figure 6.6: (a)-(b) Examples of a Gaussian-shaped pump spectrum $\Phi(\nu_1+\nu_2)$, for spectral bandwidths of 50 GHz [panel(a)] and 200 GHz [panel (b)]. The value of frequencies along the axes are in Hertz. (c),(d) Phase-matching functions, ϕ_{PM}, based on the numerically-calculated waveguide dispersion. (e),(f) The joint spectral intensity (JSI) of the photon-pair states, obtained as the product of panels (a) and (c) for the 50 GHz case, whose result is shown in panel (e), and as the product of panels (b) and (d) for the 200 GHz case, whose result is shown in panel (f). The dashed white lines indicate the passbands of the optical filters.

phase-matching function was calculated using the numerically-simulated dispersion relationship for the waveguides, as shown in Fig. 1, and using a resolution of 1001 $\times$ 1001 points in the frequency space. In traditional SPDC waveguides, phase-matching bandwidths on the order of terahertz are usually achieved, and narrowband spectral filtering in the heralded arm may be used to create heralded single photon states [186]. In the experiments reported here, the filters were composite instruments, assembled from several individually-programmable modules, and had a flat-top shape, with bandwidth about 0.8 nm.

The detection of one photon heralds the generation of the other. In general, the heralded

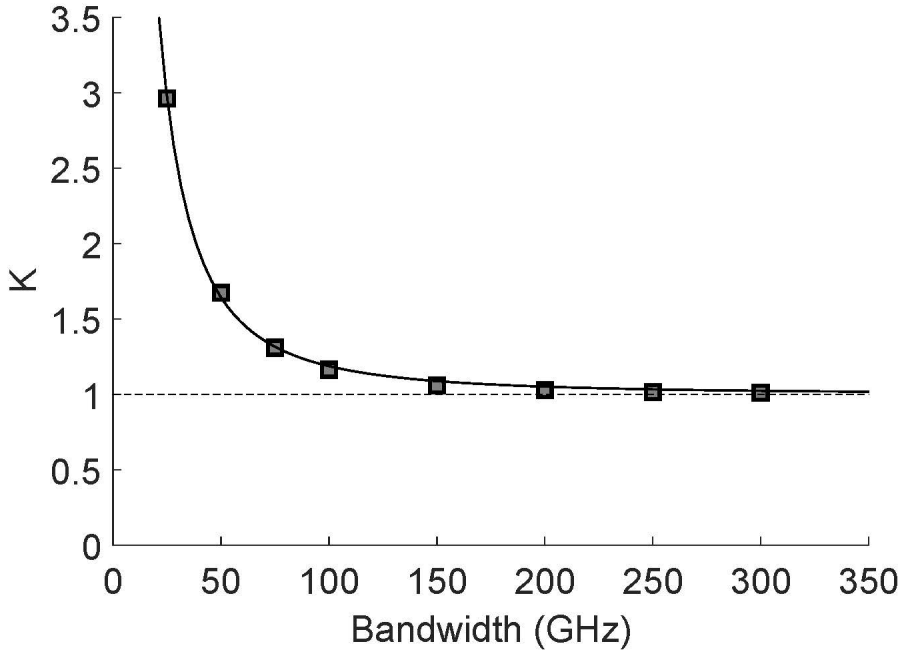

Figure 6.7: The cooperativity, K, calculated as a function of the pump bandwidth. The solid line is a visual guide, using the functional form as described in the text.

single photon is emitted into a statistical mixture of multi-frequency modes. The Schmidt decomposition of the (appropriately normalized) two-photon state [187] writes the two photon state in Eq. (6.1) as

$$|\psi\rangle = |0\rangle + c\sum_k \kappa_k \hat{A}_k^\dagger \hat{B}_k^\dagger |0\rangle \tag{6.2}$$

where $\hat{A}_k^\dagger$ and $\hat{B}_k^\dagger$ are multi-frequency modes (defined by integrals over the spectral bandwidth of the SPDC photons), κ_k are the expansion coefficients (also called Schmidt coefficients), and c is a normalizing constant. Although the term "broadband" is sometimes used, the frequency support of such modes is limited to less than 100 GHz, as imposed by the filters. Because of the non-Gaussian shape of the filters, several Schmidt modes may be transmitted with little loss. The values of κ_k are not the same for all k, i.e., the modes are not uniformly excited. This makes the detailed analysis of such a system more complicated than current models [186]. The single-photon detectors used in these experiments do not distinguish between the modes transmitted by the

filters, but do not have unity efficiency, in practice.

The cooperativity, $K = [\sum_k \kappa_k{}^4]^{-1}$, also known as the Schmidt rank, can be used to quantify the degree of purity (purity $P = K^{-1}$). Examples of calculated values of K based on the JSI, such as shown in two cases out of several in Fig. 6.6, are shown in Fig. 6.7. Depending on the pump pulse bandwidth, one may obtain separable states ($K = 1$) and entangled states ($K > 1$) during the SPDC process in these waveguides. The solid line is a visual guide using the functional form $y = 1 + (x+a)^{-2}$. Although the focus of this paper is on highly-entangled states, the possibility of nearly-separable states is indicated by Fig. 6.7 for pump pulses shorter than about 4 ps, which can be delivered by frequency-doubled fiber mode-locked lasers.

6.4 Conclusion

In conclusion, as shown in Table 6.1, high values of CAR, as well as the first reports of low values of $g_H^{(2)}(0)$ and high values of V have been made for entangled photon pairs at telecommunications wavelengths generated using poled nanoscale thin-film LN waveguides. The ability to perform high resolution in-situ imaging and analysis of the poled domain structure in 3D helped in identifying the best-poled thin-film regions from which high-performance SPDC devices were realized. Since this diagnostic technique is non-destructive, it could be useful for the future development of more complex and multi-component quantum photonic circuits using poled TFLN. We have demonstrated that such waveguides can generate several million photon pairs per second at telecommunications wavelengths with high quality using much less than a milliwatt of pump power. This significant power reduction, by two or more orders of magnitude, compared to bulk crystals and traditional SPDC waveguides without sacrificing the high figures-of-merit (CAR, Visibility, etc.) that is expected from traditional LN pair sources, is beneficial both for future scale-up of on-chip quantum circuits, and for the possible colocation of sources with cooled detectors, which is under development [188]. Taken together, these results suggest that thin-film

LN is an attractive integrated photonics platform for low-power, but high signal-to-noise ratio quantum optical applications.

6.5 Acknowledgments

Chapter 6, contains the material as it appears in the following: Jie Zhao, Chaoxuan Ma, Michael Rüsing, and Shayan Mookherjea, “High-quality entangled photon-pair generation in periodically-poled thin-film lithium niobate waveguides”, Physical Review Letters 124, 163603 (2020). The dissertation author, together with her adviser, led the research efforts for this work and co-authored the paper.

Appendix A

Second Harmonic Images after Multiple Poling Pulses

Figure A.1 presents all the measured SH images after poling pulse 1-7, 10 and 16, each with an area of 70 $\mu m \times 20\ \mu m$, which show the gradual domain spread along both z and y axes of the LN thin film. Growth along the x axis can be seen from the increase of SH signal in the inverted regions. As has been discussed in Sec. 3.2, while the domains are propagating along the z axis from poling electrodes that carry the positive voltage, they also spread in the y axis of the crystal. Therefore, the formed domain structures are narrower towards the ground electrodes. This is also one of the reasons why we chose single-pulse poling in the subsequent studies, which produces more uniform domains along z axis of the thin film. Alternatively, one may add a thin oxide insulation layer under the poling electrodes, which has been shown to improve the domain uniformity [130].

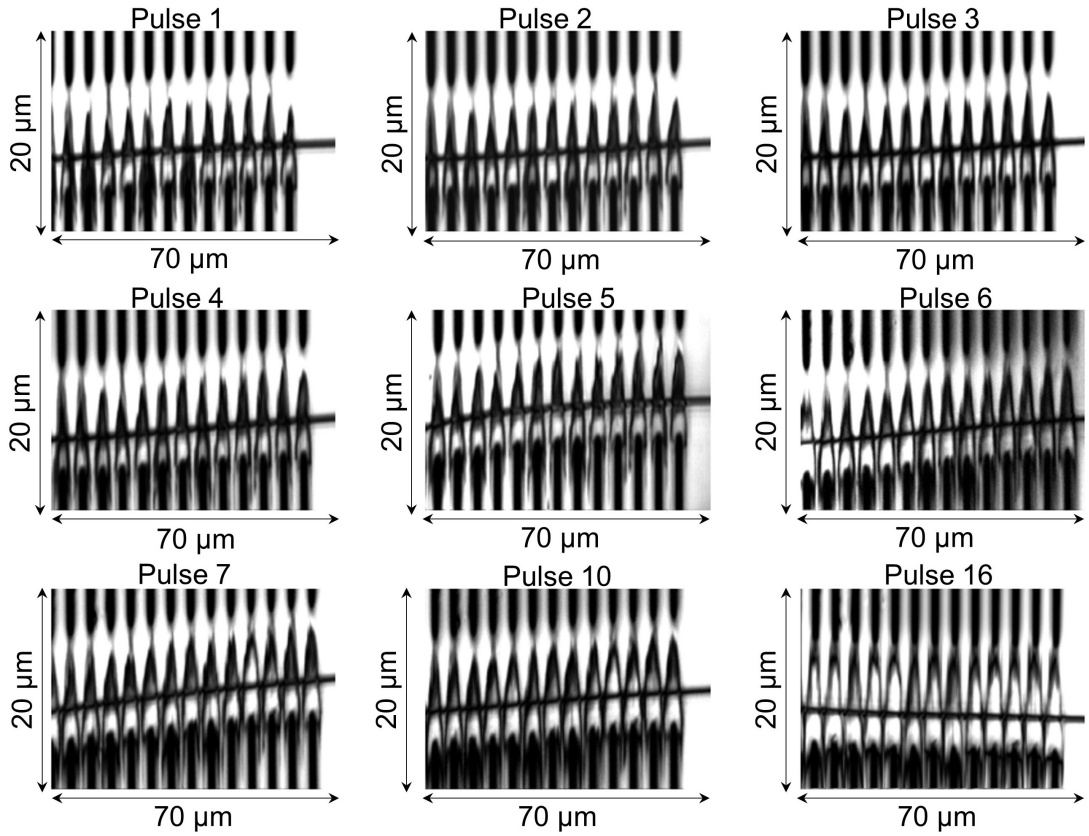

Figure A.1: Measured SH images after multiple poling pulses, showing the inverted domains gradually propagate along the z axis and spread towards the y axis of TFLN. Domain growth along the x axis can be seen as the measured SH signals gradually increase from the minimum (black/dark areas in the image) to maximum values (white/bright areas in the image), which as our simulation results suggest, correspond to partly inverted domains and completely inverted domains in depth. Note that during these experiments, the chip was removed and replaced, in order to image the gradual growth of the inverted domains after each poling pulse, while the scanned area was kept the same. Exact re-positioning of the sample was not achieved, resulting in some mis-alignment in the visual appearance of successive traces. These do not significantly affect either the results or the interpretation.

Appendix B

Second Harmonic Image of Domains with Sub-Micrometer Periodicity

As has been mentioned in the previous section, for narrow domains, i.e., for sub-micron period structures here, the diffraction-limited resolution of SH microscopy masks further details of the poled domain structures. Therefore, for sub-micron structures, only PFM images are shown in the manuscript. But we have imaged these structures using SH microscopy as well in the experiments.

Here, Fig. S3 shows measured SH images of the structures with poling periods of 1 μm, 900 nm, 800 nm and 600 nm, each with an area of 15 μm $\times$ 25 μm. The scanning step size along the y (perpendicular to the domain walls) and z (parallel to the domain walls) axis of TFLN here is 50 nm and 150 nm respectively, and the signal integration time per acquisition point is 5 ms. The dark strips on the top of the images are the poling electrode that carries the positive voltage, and the black rectangle at the bottom corresponds to the ground electrode. The black lines in between the electrodes are the domain walls, which agrees with the simulated signatures in Fig. 3.15(a). The area that is enclosed by the domain walls are the inverted domains. Similar to what the PFM images show, these SH images suggest that every second domain is slightly

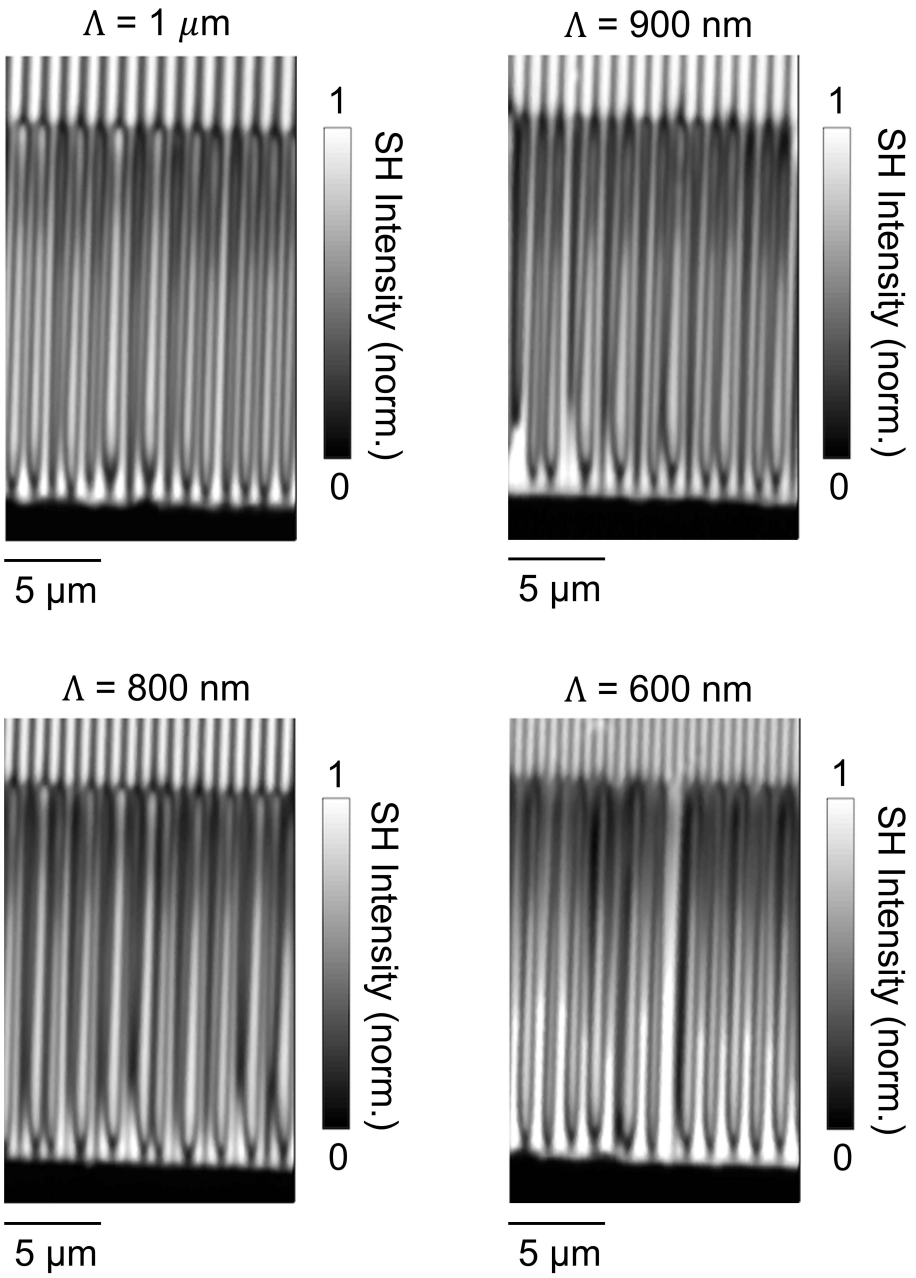

Figure B.1: Measured SH images for structures with poling periods of 1 μm, 900 nm, 800 nm and 600 nm.

narrower than the two respective neighboring domains. As the poling period gets smaller, i.e., the domain becomes narrower, this behavior is more pronounced. For $\Lambda = 600$ nm, every second domain only reaches to about one half of the gap, respectively. As suggested by the simulation results in Fig. 3.15(d), the measured SH signal in the narrow domains are much lower than that

from the wide ones. For the 600 nm period structures, only the wide domains can be seen clearly in the SH image, while according to Fig. 3.18 in the manuscript both the PFM amplitude and phase images show narrow domains with width less than 200 nm.

B.1 Acknowledgements

Appendix B, contains the material as it appears in the following: Jie Zhao, Michael Rüsing, Matthias Roeper, Lukas M. Eng, and Shayan Mookherjea, "Poling thin-film x-cut lithium niobate for quasi-phase matching with sub-micrometer periodicity", Journal of Applied Physics 127, 193104 (2020). The dissertation author, together with her adviser, led the research efforts for this work and co-authored the paper.

Appendix C

Poling Duty Cycle Calculation

The poling duty cycle is defined as $\xi = w_{\mathrm{D}}/\Lambda \times 100\%$, where w_{D} is the width of the inverted domain, and Λ is the poling period. As shown in Fig. 2 in the manuscript, the width of the inverted domains was seen to remain the same across most of the 20 μm wide gap between the electrodes, except for the region close to the ground electrode. The waveguide occupies a relatively small portion of the distance. The domain width w_{D} is calculated from two line-scans in the poling region separated by a distance of 6 μm, which is large enough to cover the optical mode [see Figs. 1(c)-(d)], with the waveguide sitting in the center. To calculate the poling duty cycle, five SH images were obtained along the entire 5 mm-long waveguide, each covering an area of 100 μm $\times$ 30 μm, as is shown in Fig. 2; Fig. C.1 shows one of the SH images from a 1.32 μm wide waveguide as an example. The width of each individual domain is calculated based on the two line-scans, from which we can get a distribution of the poling duty cycle for this 5 mm long waveguide. For each waveguide, the mean value and the standard deviation of ξ was calculated from an analysis of about 180 domains. As is shown in Fig. C.1(b), the duty cycles calculated from the two line-scans agree with each other, with the mean value and standard deviation being 50.6% and 6.4% respectively.

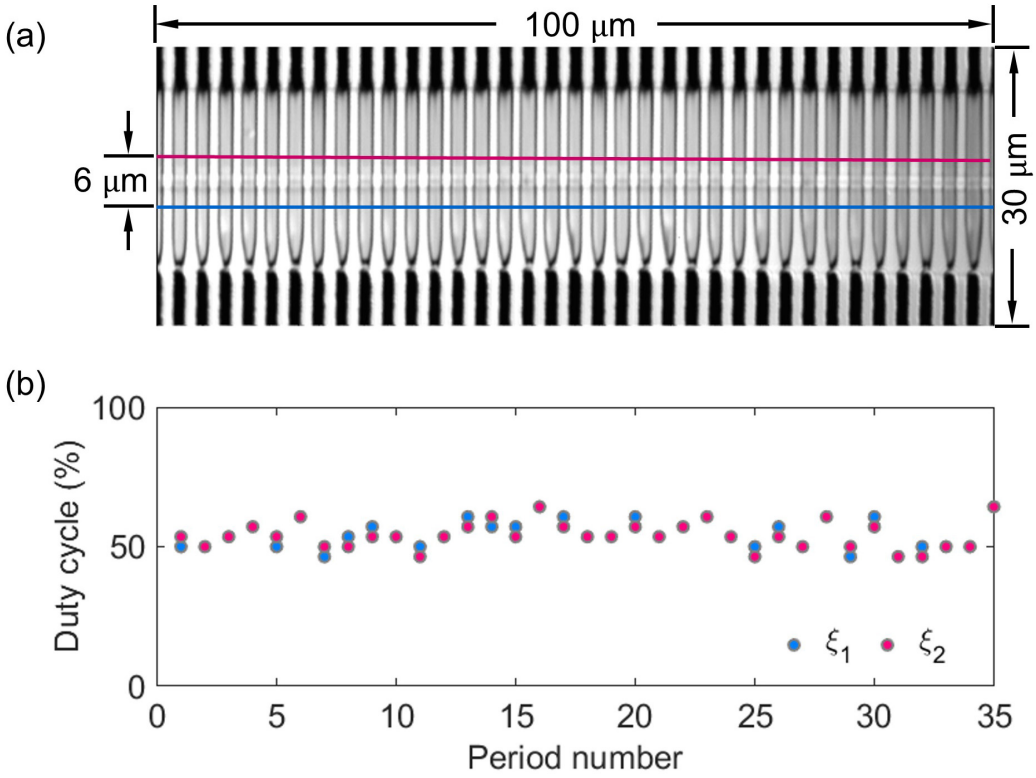

Figure C.1: (a) SH image of the inverted domains from a 1.32 μm wide waveguide. (b) Calculated duty cycles of each inverted domain based on the line-scans taken from the blue and red lines indicated in (a). The lateral spacing between the line scans is sufficient to capture the full extent of the optical mode. Other line scans within this range yield the same results.

C.1 Acknowledgements

Appendix C, contains the material as it appears in the following: Jie Zhao, Michael Rüsing, Usman A. Javid, Jingwei Ling, Mingxiao Li, Qiang Lin, and Shayan Mookherjea, "Shallow-etched thin-film lithium niobate waveguides for highly-efficient second-harmonic generation", Optics Express 28(13), 19669 (2020). The dissertation author, together with her adviser, led the research efforts for this work and co-authored the paper.

Appendix D

Repeatability of the SHG Spectrum

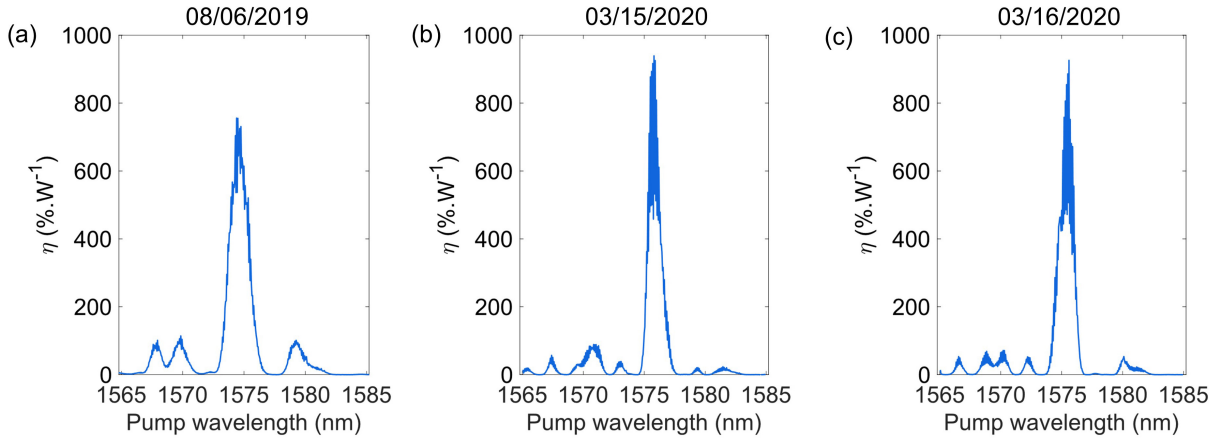

Figure D.1: Measured SHG spectra from the same waveguide on different dates.

The measured SHG spectra of the 1.14 μm wide waveguide on different dates (indicated at the top of each plot) are shown in Fig. D.1, each curve is an averaged result of several measurements on the same day. The spectrum measured before edge polishing [i.e., in Fig. D.1(a)] is a bit broader and with slightly higher sidelobes, which is probably due to the un-optimized polarization of the input pump light that can be altered by rough edges of the earlier chip, and thus has a slightly lower peak η compared to those measured after edge polishing. The slight shift of the phase-matched pump wavelength (1574.6 nm on 08/06/2019, 1575.8 nm on 03/15/2020, and 1575.6 nm on 03/16/2020) probably comes from the environment fluctuations (e.g., the humidity),

because the waveguides were directly exposed to the air without any top cladding material.

In a wet medium, on the surface of a solid will form an absorbed water layer, whose thickness depends on the humidity of the medium (air) and properties of the material surface at a constant temperature. As is shown in Ref. [189], for a LN crystal with an optically polished YZ-cut working surface, thickness of the absorbed surface water layer can reach up to 17 nm, at a humidity of 100%. Here as an example, we simulated mode indices of a 1.24 μm wide shallow-etched waveguide, with the surface water layer thickness varies from 0 nm to 15 nm at 20 °C. The calculated required poling periods for SHG from 1560 nm to 780 nm are plotted in Fig. D.2. Note that as is discussed in Sec. 5.2.2, a 3 nm difference in poling period can cause a 3 nm shift in the QPM wavelength. Though being highly tolerant to the waveguide width and environment temperature variation, this shallow-etched waveguide structure is quite sensitive to etching depth, i.e., waveguide ridge height fluctuation, as can be seen from Fig. 5.6. As the surface water layer thickness changes, we should expect a relatively evident variation in the QPM wavelength. Therefore, slight variations in the environment humidity, and thus fluctuations in the surface water layer thickness on the waveguide could account for the measured shift in QPM wavelengths on different dates.

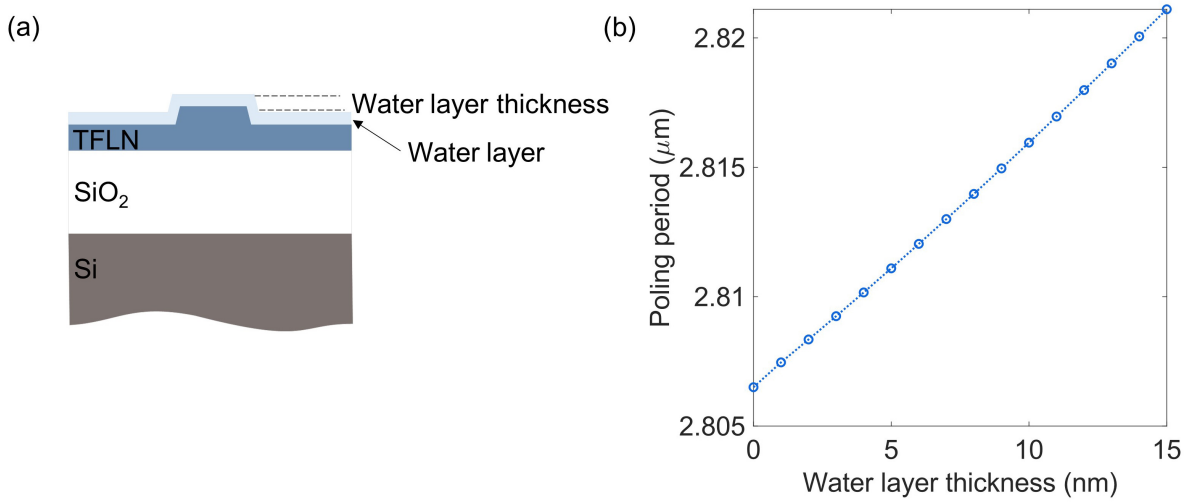

Figure D.2: (a) Cross section of the waveguiding structure. (b) Calculated poling period as a function of the surface water layer thickness.

In the future, to improve the stability of this device, the chip can be encapsulated and packaged, as is generally performed for traditional PPLN waveguides [190]. Alternatively, an oxide cladding layer could be added to the waveguide in future design, which can not only improve the repeatability of the measured QPM tuning spectrum, but also enhance the edge coupling efficiency to standard tapered lensed fibers by introducing a more symmetrical optical mode. Nevertheless, the multiple SHG spectra presented here prove that the high performance of this device can be maintained up to at least six months.

D.1 Acknowledgements

Appendix D, contains the material as it appears in the following: Jie Zhao, Michael Rüsing, Usman A. Javid, Jingwei Ling, Mingxiao Li, Qiang Lin, and Shayan Mookherjea, "Shallow-etched thin-film lithium niobate waveguides for highly-efficient second-harmonic generation", Optics Express 28(13), 19669 (2020). The dissertation author, together with her adviser, led the research efforts for this work and co-authored the paper.

Bibliography

[1] S. Tanzilli, W. Tittel, H. De Riedmatten, H. Zbinden, P. Baldi, M. Demicheli, D. B. Ostrowsky, and N. Gisin, "PPLN waveguide for quantum communication," European Physical Journal D, vol. 18, no. 2, pp. 155–160, 2002.

[2] S. Tanzilli, W. Tittel, M. Halder, O. Alibart, P. Baldi, N. Gisin, and H. Zbinden, "A photonic quantum information interface," Nature, vol. 437, no. 7055, pp. 116–120, 2005.

[3] L. E. Myers, R. C. Eckardt, M. M. Fejer, R. L. Byer, W. R. Bosenberg, and J. W. Pierce, "Quasi-phase-matched optical parametric oscillators in bulk periodically poled $LiNbO_3$," J. Opt. Soc. Am. B, vol. 12, p. 2102, 1995.

[4] S. D. Butterworth, V. Pruneri, and D. C. Hanna, "Optical parametric oscillation in periodically poled lithium niobate based on continuous-wave synchronous pumping at 1.047 microm.," Opt. Lett., vol. 21, no. 17, pp. 1345–1347, 1996.

[5] L. Lefort, K. Puech, S. D. Butterworth, G. W. Ross, P. G. Smith, D. C. Hanna, and D. H. Jundt, "Efficient, low-threshold synchronously-pumped parametric oscillation in periodically-poled lithium niobate over the 1.3 μm to 5.3 μm range," Opt. Commun., vol. 152, pp. 55–58, 1998.

[6] K. R. Parameswaran, J. R. Kurz, R. V. Roussev, and M. M. Fejer, "Observation of 99% pump depletion in single-pass second-harmonic generation in a periodically poled lithium niobate waveguide," Optics Letters, vol. 27, no. 1, pp. 43–45, 2002.

[7] R. V. Roussev, C. Langrock, J. R. Kurz, and M. M. Fejer, "Periodically poled lithium niobate waveguide sum-frequency generator for efficient single-photon detection at communication wavelengths," Opt. Lett., vol. 29, no. 13, pp. 1518–1520, 2004.

[8] L. Chang, Y. Li, N. Volet, L. Wang, J. Peters, and J. E. Bowers, "Thin film wavelength converters for photonic integrated circuits," Optica, vol. 3, no. 5, pp. 531–535, 2016.

[9] A. Rao, M. Malinowski, A. Honardoost, J. R. Talukder, P. Rabiei, P. Delfyett, and S. Fathpour, "Second-harmonic generation in periodically-poled thin film lithium niobate wafer-bonded on silicon," Opt. Express, vol. 24, no. 26, pp. 29941–29947, 2016.

[10] C. Wang, C. Langrock, A. Marandi, M. Jankowski, M. Zhang, B. Desiatov, M. M. Fejer, and M. Lončar, "Ultrahigh-efficiency wavelength conversion in nanophotonic periodically poled lithium niobate waveguides," Optica, vol. 5, no. 11, pp. 1438–1441, 2018.

[11] J.-y. Chen, Y. Meng Sua, Z.-h. Ma, C. Tang, Z. Li, and Y.-p. Huang, "Efficient parametric frequency conversion in lithium niobate nanophotonic chips," OSA Continuum, vol. 2, no. 10, pp. 2914–2924, 2019.

[12] A. Boes, L. Chang, M. Knoerzer, T. G. Nguyen, J. D. Peters, J. E. Bowers, and A. Mitchell, "Improved second harmonic performance in periodically poled LNOI waveguides through engineering of lateral leakage," Opt. Express, vol. 27, no. 17, pp. 23919–23928, 2019.

[13] A. Rao, K. Abdelsalam, T. Sjaardema, A. Honardoost, G. F. Camacho-Gonzalez, and S. Fathpour, "Actively-monitored periodic-poling in thin-film lithium niobate photonic waveguides with ultrahigh nonlinear conversion efficiency of 4600 $\%W^{-1}cm^{-2}$," Opt. Express, vol. 27, no. 18, pp. 25920–25930, 2019.

[14] K. Nassau, H. J. Levinstein, and G. M. Loiacono, "The domain structure and etching of ferroelectric lithium niobate," Appl. Phys. Lett., vol. 6, no. 11, pp. 228–229, 1965.

[15] J. Lu, J. B. Surya, X. Liu, A. W. Bruch, Z. Gong, Y. Xu, and H. X. Tang, "Periodically poled thin film lithium niobate microring resonators with a second-harmonic generation efficiency of 250,000%/W," Optica, vol. 6, no. 12, p. 1455, 2019.

[16] D. Bouwmeester, J.-W. Pan, K. Mattle, M. Eibl, H. Weinfurter, and A. Zeilinger, "Experimental quantum teleportation," Nature, vol. 390, no. 6660, pp. 575–579, 1997.

[17] W. Tittel, J. Brendel, H. Zbinden, and N. Gisin, "Violation of bell inequalities by photons more than 10 km apart," Phys. Rev. Lett., vol. 81, no. 17, pp. 3563–3566, 1998.

[18] D. Bouwmeester, J. W. Pan, M. Bongaerts, and A. Zeilinger, "Observation of three-photon greenberger-horne-zeilinger entanglement," Phys. Rev. Lett., vol. 82, no. 7, pp. 1345–1349, 1999.

[19] T. Jennewein, C. Simon, G. Weihs, H. Weinfurter, and A. Zeilinger, "Quantum Cryptography with Entangled Photons," Phys. Rev. Lett., vol. 84, no. 20, pp. 4729–4732, 2000.

[20] P. Walther, K. J. Resch, T. Rudolph, E. Schenck, H. Weinfurter, V. Vedral, M. Aspelmeyer, and A. Zeilinger, "Experimental one-way quantum computing," Nature, vol. 434, pp. 169–176, 2005.

[21] L. K. Shalm, E. Meyer-Scott, B. G. Christensen, P. Bierhorst, M. A. Wayne, M. J. Stevens, T. Gerrits, S. Glancy, D. R. Hamel, M. S. Allman, K. J. Coakley, S. D. Dyer, C. Hodge, A. E. Lita, V. B. Verma, C. Lambrocco, E. Tortorici, A. L. Migdall, Y. Zhang, D. R. Kumor, W. H. Farr, F. Marsili, M. D. Shaw, J. A. Stern, C. Abellán, W. Amaya, V. Pruneri,

T. Jennewein, M. W. Mitchell, P. G. Kwiat, J. C. Bienfang, R. P. Mirin, E. Knill, and S. W. Nam, "Strong Loophole-Free Test of Local Realism," Phys. Rev. Lett., vol. 115, p. 250402, 2015.

[22] M. Giustina, M. A. Versteegh, S. Wengerowsky, J. Handsteiner, A. Hochrainer, K. Phelan, F. Steinlechner, J. Kofler, J. Å. Larsson, C. Abellán, W. Amaya, V. Pruneri, M. W. Mitchell, J. Beyer, T. Gerrits, A. E. Lita, L. K. Shalm, S. W. Nam, T. Scheidl, R. Ursin, B. Wittmann, and A. Zeilinger, "Significant-Loophole-Free Test of Bell's Theorem with Entangled Photons," Phys. Rev. Lett., vol. 115, no. 25, p. 250401, 2015.

[23] J.-G. Ren, P. Xu, H.-L. Yong, L. Zhang, S.-K. Liao, J. Yin, W.-Y. Liu, W.-Q. Cai, M. Yang, L. Li, K.-X. Yang, X. Han, Y.-Q. Yao, J. Li, H.-Y. Wu, S. Wan, L. Liu, D.-Q. Liu, Y.-W. Kuang, Z.-P. He, P. Shang, C. Guo, R.-H. Zheng, K. Tian, Z.-C. Zhu, N.-L. Liu, C.-Y. Lu, R. Shu, Y.-A. Chen, C.-Z. Peng, J.-Y. Wang, and J.-W. Pan, "Ground-to-satellite quantum teleportation," Nature, vol. 549, pp. 70–73, 2017.

[24] A. L. Migdall, D. Branning, and S. Castelletto, "Tailoring single-photon and multiphoton probabilities of a single-photon on-demand source," Phys. Rev. A, vol. 66, p. 053805, 2002.

[25] J. L. O'Brien, A. Furusawa, and J. Vučković, "Photonic quantum technologies," Nat. Photonics, vol. 3, no. 12, pp. 687–695, 2009.

[26] X. S. Ma, S. Zotter, J. Kofler, T. Jennewein, and A. Zeilinger, "Experimental generation of single photons via active multiplexing," Phys. Rev. A, vol. 83, no. 4, p. 43814, 2011.

[27] T. Suhara, "Generation of quantum-entangled twin photons by waveguide nonlinear-optic devices," Laser & Photon. Rev., vol. 3, no. 4, pp. 370–393, 2009.

[28] A. Christ, A. Fedrizzi, H. Hübel, T. Jennewein, and C. Silberhorn, Single-Photon Generation and Detection, ch. Parametric, pp. 351–410, Elsevier Inc., 2013.

[29] E. Engin, D. Bonneau, C. M. Natarajan, A. S. Clark, M. G. Tanner, R. H. Hadfield, S. N. Dorenbos, V. Zwiller, K. Ohira, N. Suzuki, H. Yoshida, N. Iizuka, M. Ezaki, J. L. O'Brien, and M. G. Thompson, "Photon pair generation in a silicon micro-ring resonator with reverse bias enhancement," Opt. Express, vol. 21, pp. 27826–27834, 2013.

[30] C. Ma, X. Wang, V. Anant, A. D. Beyer, M. D. Shaw, and S. Mookherjea, "Silicon photonic entangled photon-pair and heralded single photon generation with CAR $>$ 12,000 and $g^{(2)}(0) < 0006$," Opt. Express, vol. 25, no. 26, p. 32995, 2017.

[31] A. A. Ballman, "Growth of Piezoelectric and Ferroelectric Materials by the Czochralski Technoque," J. Am. Ceram. Soc., vol. 48, no. 2, pp. 112–113, 1965.

[32] K. Nassau, H. J. Levinstein, and G. M. Loiacono, "Ferroelectric Lithium Nniobate 1. Growth , Domain Lithium Dislocations," J. Phys. Chem. Solids, vol. 27, pp. 983–988, 1966.

[33] K. Nassau, H. J. Levinstein, and G. M. Loiacono, "Ferroelectric lithium niobate. 2. Preparation of single domain crystals," J. Phys. Chem. Solids, vol. 27, pp. 989–996, 1966.

[34] S. C. Abrahams, J. M. Reddy, and J. L. Bernstein, "Ferroelectric lithium niobate. 3. Single crystal X-ray diffraction study at 24°C," J. Phys. Chem. Solids, vol. 27, pp. 997–1012, 1966.

[35] S. C. Abrahams, W. C. Hamilton, and J. M. Reddy, "Ferroelectric lithium niobate. 4. Single crystal neutron diffraction study at 24°C," J. Phys. Chem. Solids, vol. 27, pp. 1013–1018, 1966.

[36] S. C. Abrahams, H. J. Levinstein, and J. M. Reddy, "Ferroelectric lithium niobate. 5. Polycrystal X-ray diffraction study between 24° and 1200°C," J. Phys. Chem. Solids, vol. 27, pp. 1019–1026, 1966.

[37] R. L. Sutherland, Handbook of Nonlinear Optics. CRC Press, 2003.

[38] D. A. Roberts, "Simplified Characterization of Uniaxial and Biaxial Nonlinear Optical Crystals: A Plea for Standardization of Nomenclature and Conventions," IEEE Journal of Quantum Electronics, vol. 28, no. 2, pp. 2057–2074, 1992.

[39] K. K. Wong, Properties of Lithium Niobate. Institution of Engineering and Technology, 2002.

[40] https://www.globenewswire.com/news-release/2020/03/26/2006948/0/en/the-global-market-estimate-for-lithium-niobate-modulators-will-hit-36-711-billion-by-2026-research-dive.html.

[41] M. Bazzan and C. Sada, "Optical waveguides in lithium niobate: Recent developments and applications," Applied Physics Reviews, vol. 2, no. 4, 2015.

[42] M. N. Armenise, "Fabrication Techniques of Lithium Niobate Waveguides.," IEE proceedings. Part J, Optoelectronics, vol. 135, no. 2, pp. 85–91, 1988.

[43] K. Noguchi, O. Mitomi, H. Miyazawa, and S. Seki, "A Broadband Ti:$LiNbO_3$ Optical Modulator with a Ridge Structure," Journal of Lightwave Technology, vol. 13, no. 6, pp. 1164–1168, 1995.

[44] H. Hu, A. P. Milenin, R. B. Wehrspohn, H. Hermann, and W. Sohler, "Plasma etching of proton-exchanged lithium niobate," Journal of Vacuum Science & Technology A: Vacuum, Surfaces, and Films, vol. 24, no. 4, pp. 1012–1015, 2006.

[45] R. Takigawa, E. Higurashi, T. Kawanishi, and T. Asano, "Lithium niobate ridged waveguides with smooth vertical sidewalls fabricated by an ultra-precision cutting method," Opt. Express, vol. 22, no. 22, pp. 27733–27738, 2014.

[46] H. Hu, R. Ricken, W. Sohler, and R. B. Wehrspohn, "Lithium niobate ridge waveguides fabricated by wet etching," IEEE Photonics Technology Letters, vol. 19, no. 6, pp. 417–419, 2007.

[47] M. Rüsing, P. O. Weigel, J. Zhao, and S. Mookherjea, "Toward 3d integrated photonics including lithium niobate thin films: a bridge between electronics, radio frequency, and optical technology," IEEE Nanotechnology Magazine, vol. 13, no. 4, pp. 18–33, 2019.

[48] A. Honardoost, K. Abdelsalam, and S. Fathpour, "Rejuvenating a Versatile Photonic Material: Thin-Film Lithium Niobate," Laser and Photonics Reviews, vol. 14, no. 9, pp. 1–20, 2020.

[49] M. Levy, R. M. Osgood, R. Liu, L. E. Cross, G. S. Cargill, A. Kumar, and H. Bakhru, "Fabrication of single-crystal lithium niobate films by crystal ion slicing," Applied Physics Letters, vol. 73, no. 16, pp. 2293–2295, 1998.

[50] P. Rabiei and P. Gunter, "Optical and electro-optical properties of submicrometer lithium niobate slab waveguides prepared by crystal ion slicing and wafer bonding," Applied Physics Letters, vol. 85, no. 20, pp. 4603–4605, 2004.

[51] H. Hu, L. Gui, R. Ricken, and W. Sohler, "Towards nonlinear photonic wires in lithium niobate," Integrated Optics: Devices, Materials, and Technologies XIV, vol. 7604, p. 76040R, 2010.

[52] "Jinan Jingzheng Electronics Co., Ltd.." https://www.nanoln.com/.

[53] "Partow Technologies LLC." http://www.partow-tech.com/.

[54] "NGK Insulators." https://www.ngk-insulators.com/en/index.html.

[55] K. Noguchi, O. Mitomi, and H. Miyazawa, "Millimeter-wave Ti:$LiNbO_3$ optical modulators," Journal of Lightwave Technology, 1998.

[56] C. Wang, M. Zhang, X. Chen, M. Bertrand, A. Shams-Ansari, S. Chandrasekhar, P. Winzer, and M. Lončar, "Integrated lithium niobate electro-optic modulators operating at CMOS-compatible voltages," Nature, vol. 562, pp. 101–104, 2018.

[57] K. R. Parameswaran, R. K. Route, J. R. Kurz, R. V. Roussev, M. M. Fejer, and M. Fujimura, "Highly efficient second-harmonic generation in buried waveguides formed by annealed and reverse proton exchange in periodically poled lithium niobate," Opt. Lett., vol. 27, no. 3, pp. 179–181, 2002.

[58] J. Zhao, M. Rüsing, U. A. Javid, J. Ling, M. Li, Q. Lin, and S. Mookherjea, "Shallow-etched thin-film lithium niobate waveguides for highly-efficient second-harmonic generation," Opt. Express, vol. 28, no. 13, pp. 19669–19682, 2020.

[59] P. O. Weigel, M. Savanier, C. T. DeRose, A. T. Pomerene, A. L. Starbuck, A. L. Lentine, V. Stenger, and S. Mookherjea, "Lightwave Circuits in Lithium Niobate through Hybrid Waveguides with Silicon Photonics," Scientific Reports, vol. 6, p. 22301, 2016.

[60] C. Vannahme, H. Suche, S. Reza, R. Ricken, V. Quiring, and W. Sohler, "Integrated Optical Ti:$LiNbO_3$ Ring Resonator for Rotation Rate Sensing," Proceedings to the 13th European Conference on Integrated Optics, WE1, IEEE, 2007.

[61] P. O. Weigel, J. Zhao, K. Fang, H. Al-Rubaye, D. Trotter, D. Hood, J. Mudrick, C. Dallo, A. T. Pomerene, A. L. Starbuck, C. T. DeRose, A. L. Lentine, G. Rebeiz, and S. Mookherjea, "Bonded thin film lithium niobate modulator on a silicon photonics platform exceeding 100 GHz 3-dB electrical modulation bandwidth," Optics Express, vol. 26, no. 18, pp. 23728–23739, 2018.

[62] A. Pan, C. Hu, C. Zeng, and J. Xia, "Fundamental mode hybridization in a thin film lithium niobate ridge waveguide," Optics Express, vol. 27, no. 24, pp. 35659-35669, 2019.

[63] E. Saitoh, Y. Kawaguchi, K. Saitoh, and M. Koshiba, "TE/TM-Pass Polarizer Based on Lithium Niobate on Insulator Ridge Waveguide," IEEE Photonics Journal, vol. 5, no. 2, p. 6600610, 2013.

[64] R. Luo, Y. He, H. Liang, M. Li, and Q. Lin, "Highly tunable efficient second-harmonic generation in a lithium niobate nanophotonic waveguide," Optica, vol. 5, no. 8, p. 1006, 2018.

[65] L. He, M. Zhang, A. Shams-Ansari, R. Zhu, C. Wang, and M. Loncar, "Low-loss fiber-to-chip interface for lithium niobate photonic integrated circuits," Opt. Lett., vol. 44, no. 9, pp. 2314–2317, 2019.

[66] I. Krasnokutska, R. J. Chapman, J.-L. J. Tambasco, and A. Peruzzo, "High coupling efficiency grating couplers on lithium niobate on insulator," Opt. Express, vol. 27, no. 13, pp. 17681-17685, 2019.

[67] M. Zhang, C. Wang, R. Cheng, A. Shams-Ansari, and M. Lončar, "Monolithic ultra-high-Q lithium niobate microring resonator," Optica, vol. 4, no. 12, pp. 1536–1537, 2017.

[68] M. F. Volk, S. Suntsov, C. E. Rüter, and D. Kip, "Low loss ridge waveguides in lithium niobate thin films by optical grade diamond blade dicing," Opt. Express, vol. 24, no. 2, pp. 1386–1391, 2016.

[69] P. Rabiei, J. Ma, S. Khan, J. Chiles, and S. Fathpour, "Heterogeneous lithium niobate photonics on silicon substrates," Opt. Express, vol. 21, no. 21, pp. 25573–25581, 2013.

[70] T. R. Volk, R. V. Gainutdinov, and H. H. Zhang, "Domain-wall conduction in AFM-written domain patterns in ion-sliced $LiNbO_3$ films," Appl. Phys. Lett., vol. 110, p. 132905, 2017.

[71] E. Fatuzzo and W. J. Merz, Ferroelectricity. North-Holland, 1967.

[72] P. Mackwitz, M. Rüsing, G. Berth, A. Widhalm, K. Müller, and A. Zrenner, "Periodic domain inversion in x-cut single-crystal lithium niobate thin film," Appl. Phys. Lett., vol. 108, p. 152902, 2016.

[73] L. Gui, H. Hu, M. Garcia-Granda, and W. Sohler, "Local periodic poling of ridges and ridge waveguides on X- and Y-Cut $LiNbO_3$ and its application for second harmonic generation," Optics Express, vol. 17, no. 5, pp. 3923–3928, 2009.

[74] S. Sanna and W. G. Schmidt, "$LiNbO_3$ surfaces from a microscopic perspective," Journal of Physics: Condensed Matter, vol. 29, p. 413001, 2017.

[75] G. D. Miller, Periodically poled lithium niobate: modeling, fabrication, and nonlinear optical performance. PhD thesis, Stanford University, 1998.

[76] J. W. Choi, D. K. Ko, J. H. Ro, and N. E. Yu, "Sidewise domain wall velocity of MgO doped stoichiometric lithium niobate by real-time visualization," Ferroelectrics, vol. 439, no. 1, pp. 13–19, 2012.

[77] M. Rüsing, C. Eigner, P. MacKwitz, G. Berth, C. Silberhorn, and A. Zrenner, "Identification of ferroelectric domain structure sensitive phonon modes in potassium titanyl phosphate: A fundamental study," J. Appl. Phys., vol. 119, p. 044103, 2016.

[78] M. Rüsing, S. Neufeld, J. Brockmeier, C. Eigner, P. Mackwitz, K. Spychala, C. Silberhorn, W. G. Schmidt, G. Berth, A. Zrenner, and S. Sanna, "Imaging of 180 ferroelectric domain walls in uniaxial ferroelectrics by confocal Raman spectroscopy: Unraveling the contrast mechanism," Phys. Rev. Mater., vol. 2, p. 103801, 2018.

[79] V. Y. Shur and P. S. Zelenovskiy, "Micro- and nanodomain imaging in uniaxial ferroelectrics: Joint application of optical, confocal Raman, and piezoelectric force microscopy," J. Appl. Phys., vol. 116, p. 066802, 2014.

[80] E. Soergel, "Piezoresponse force microscopy (PFM)," J. Phys. D: Appl. Phys., vol. 44, p. 464003, 2011.

[81] F. Johann, Y. J. Ying, T. Jungk, Á. Hoffmann, C. L. Sones, R. W. Eason, S. Mailis, and E. Soergel, "Depth resolution of piezoresponse force microscopy," Appl. Phys. Lett., vol. 94, p. 172904, 2009.

[82] S. I. Bozhevolnyi, J. M. Hvam, K. Pedersen, F. Laurell, H. Karlsson, T. Skettrup, and M. Belmonte, "Second-harmonic imaging of ferroelectric domain walls," Appl. Phys. Lett., vol. 73, no. 13, pp. 1814–1816, 1998.

[83] S. Kurimura and Y. Uesu, "Application of the second harmonic generation microscope to nondestructive observation of periodically poled ferroelectric domains in quasi-phase-matched wavelength converters," Journal of Applied Physics, vol. 81, no. 1, pp. 369–375, 1997.

[84] M. Flörsheimer, R. Paschotta, U. Kubitscheck, C. Brillert, D. Hofmann, L. Heuer, G. Schreiber, C. Verbeek, W. Sohler, and H. Fuchs, "Second-harmonic imaging of ferroelectric domains in $LiNbO_3$ with micron resolution in lateral and axial directions," Appl. Phys. B, vol. 67, no. 5, pp. 593–599, 1998.

[85] G. Berth, V. Quiring, W. Sohler, and A. Zrenner, "Depth-resolved analysis of ferroelectric domain structures in Ti:PPLN waveguides by nonlinear confocal laser scanning microscopy," Ferroelectrics, vol. 352, no. 1, pp. 78–85, 2007.

[86] J. Kaneshiro, Y. Uesu, and T. Fukui, "Visibility of inverted domain structures using the second harmonic generation microscope: Comparison of interference and non-interference cases," Journal of the Optical Society of America B, vol. 27, no. 5, pp. 888–894, 2010.

[87] S. Cherifi-Hertel, H. Bulou, R. Hertel, G. Taupier, K. D. H. Dorkenoo, C. Andreas, J. Guyonnet, I. Gaponenko, K. Gallo, and P. Paruch, "Non-Ising and chiral ferroelectric domain walls revealed by nonlinear optical microscopy," Nature Communications, vol. 8, p. 15768, 2017.

[88] S. Hell, G. Reiner, C. Cremer, and E. H. K. Stelzer, "Aberrations in confocal fluorescence microscopy induced by mismatches in refractive index," Journal of Microscopy, vol. 169, pp. 391–405, 1993.

[89] X. Huang, D. Wei, Y. Wang, Y. Zhu, Y. Zhang, X. P. Hu, S. N. Zhu, and M. Xiao, "Second-harmonic interference imaging of ferroelectric domains through a scanning microscope," Journal of Physics D: Applied Physics, vol. 50, p. 485105, 2017.

[90] D. E. Aspnes and A. A. Studna, "Dielectric functions and optical parameters of Si, Ge, GaP, GaAs, GaSb, InP, InAs, and InSb from 1.5 to 6.0 eV," Physical Review B, vol. 27, pp. 985–1009, 1983.

[91] D. Sandkuijl, A. E. Tuer, D. Tokarz, J. E. Sipe, and V. Barzda, "Numerical second- and third-harmonic generation microscopy," J. Opt. Soc. Am. B, vol. 30, pp. 382–395, 2013.

[92] S. E. Baroni, "Dielectric functions and optical parameters of Si, Ge, GaP, GaAs, GaSb, InP, InAs, and InSb from 1.5 to 6.0 eV," Phys. Rev. B, vol. 27, no. 2, pp. 985-1009, 1983.

[93] D. E. Zelmon, D. L. Small, and D. Jundt, "Infrared corrected Sellmeier coefficients for congruently grown lithium niobate and 5 mol% magnesium oxide – doped lithium niobate," Journal of the Optical Society of America B, vol. 14, pp. 3319–3322, 1997.

[94] I. H. Malitson, "Interspecimen Comparison of the Refractive Index of Fused Silica," Journal of the Optical Society of America, vol. 55, no. 10, pp. 1205–1209, 1965.

[95] M. A. Green, "Self-consistent optical parameters of intrinsic silicon at 300 K including temperature coefficients," Solar Energy Materials and Solar Cells, vol. 92, no. 11, pp. 1305–1310, 2008.

[96] M. Rüsing, J. Zhao, and S. Mookherjea, "Second harmonic microscopy of poled x-cut thin film lithium niobate: Understanding the contrast mechanism," Journal of Applied Physics, vol. 126, no. 11, 2019.

[97] M. Missey, S. Russell, V. Dominic, R. Batchko, and K. Schepler, "Real-time visualization of domain formation in periodically poled lithium niobate," Optics Express, vol. 6, no. 10, pp. 186–195, 2000.

[98] S. Grilli, P. Ferraro, M. Paturzo, D. Alfieri, and P. De Natale, "In-situ visualization, monitoring and analysis of electric field domain reversal process in ferroelectric crystals by digital holography," Opt. Express, vol. 12, no. 9, pp. 1832–1842, 2004.

[99] H. Karlsson, F. Laurell, and L. K. Cheng, "Periodic poling of $RbTiOPO_4$ for quasi-phase matched blue light generation," Applied Physics Letters, vol. 74, no. 11, pp. 1519–1521, 1999.

[100] J. Hellström, R. Clemens, V. Pasiskevicius, H. Karlsson, and F. Laurell, "Real-time and in situ monitoring of ferroelectric domains during periodic electric field poling of $KTiOPO_4$," Journal of Applied Physics, vol. 90, no. 3, pp. 1489–1495, 2001.

[101] C. Eigner, M. Santandrea, L. Padberg, M. F. Volk, C. E. Rüter, H. Herrmann, D. Kip, and C. Silberhorn, "Periodically poled ridge waveguides in KTP for second harmonic generation in the UV regime," Optics Express, vol. 26, no. 22, pp. 28827–28833, 2018.

[102] L. Chang, Y. Li, N. Volet, L. Wang, J. Peters, and J. E. Bowers, "Thin film wavelength converters for photonic integrated circuits," Optica, vol. 3, no. 5, pp. 531–535, 2016.

[103] T. R. Volk, R. V. Gainutdinov, and H. H. Zhang, "Domain-wall conduction in AFM-written domain patterns in ion-sliced $LiNbO_3$ films," Applied Physics Letters, vol. 110, no. 13, p. 132905, 2017.

[104] C. Godau, T. Kämpfe, A. Thiessen, L. M. Eng, and A. Haußmann, "Enhancing the Domain Wall Conductivity in Lithium Niobate Single Crystals," ACS Nano, vol. 11, no. 5, pp. 4816–4824, 2017.

[105] J. T. Nagy and R. M. Reano, "Periodic Poling of Ion-Sliced X-Cut Magnesium Oxide Doped Lithium Niobate Thin Films," in Conference on Lasers and Electro-Optics, p. SF2I.2, OSA, 2018.

[106] J. T. Nagy and R. M. Reano, "Submicrometer periodic poling of lithium niobate thin films with bipolar preconditioning pulses," Opt. Mater. Express, vol. 10, no. 8, pp. 1911–1920, 2020.

[107] M. Rüsing, J. Zhao, and S. Mookherjea, "Second harmonic microscopy of poled x-cut thin film lithium niobate: Understanding the contrast mechanism," J. Appl. Phys., vol. 126, p. 114105, 2019.

[108] A. V. Ievlev, S. Jesse, A. N. Morozovska, E. Strelcov, E. A. Eliseev, Y. V. Pershin, A. Kumar, V. Y. Shur, and S. V. Kalinin, "Intermittency, quasiperiodicity and chaos in probe-induced ferroelectric domain switching," Nat. Phys., vol. 10, pp. 59–66, 2014.

[109] T. Kämpfe, P. Reichenbach, M. Schröder, A. Haußmann, L. M. Eng, T. Woike, and E. Soergel, "Optical three-dimensional profiling of charged domain walls in ferroelectrics by Cherenkov second-harmonic generation," Physical Review B - Condensed Matter and Materials Physics, vol. 89, no. 3, pp. 1–4, 2014.

[110] C. Canalias and V. Pasiskevicius, "Mirrorless optical parametric oscillator," Nat. Photonics, vol. 1, pp. 459–462, 2007.

[111] A. Christ, A. Eckstein, P. J. Mosley, and C. Silberhorn, "Pure single photon generation by type-I PDC with backward-wave amplification," Opt. Express, vol. 17, no. 5, pp. 3441–3446, 2009.

[112] A. Boes, V. Sivan, G. Ren, D. Yudistira, S. Mailis, E. Soergel, and A. Mitchell, "Precise, reproducible nano-domain engineering in lithium niobate crystals," Appl. Phys. Lett., vol. 107, p. 022901, 2015.

[113] S. Grilli, P. Ferraro, L. Sansone, M. Paturzo, and P. De Natale, "Fabrication of sub-micron period surface structures in $LiNbO_3$," Ferroelectrics, vol. 352, no. 1, pp. 72–77, 2007.

[114] A. C. Busacca, C. L. Sones, V. Apostolopoulos, R. W. Eason, and S. Mailis, "Surface domain engineering in congruent lithium niobate single crystals: A route to submicron periodic poling," Appl. Phys. Lett., vol. 81, no. 26, pp. 4946–4948, 2002.

[115] M. Minakata, M. S. Islam, S. Nagano, S. Yoneyama, T. Sugiyama, and H. Awano, "Nanometer size periodic domain inversion in $LiNbO_3$ substrate using circular form full cover electrodes," Solid-State Electronics, vol. 50, no. 5, pp. 848–852, 2006.

[116] C. Canalias, V. Pasiskevicius, R. Clemens, and F. Laurell, "Submicron periodically poled flux-grown $KTiOPO_4$," Appl. Phys. Lett., vol. 82, no. 24, pp. 4233–4235, 2003.

[117] C. Canalias, V. Pasiskevicius, and F. Laurell, "Periodic poling of $KTiOPO_4$: From micrometer to sub-micrometer domain gratings," Ferroelectrics, vol. 340, no. 1, pp. 27–47, 2006.

[118] A. Zukauskas, A. L. Viotti, C. Liljestrand, V. Pasiskevicius, and C. Canalias, "Cascaded counter-propagating nonlinear interactions in highly-efficient sub-μm periodically poled crystals," Sci. Rep., vol. 7, p. 8037, 2017.

[119] R. S. Coetzee, A. Zukauskas, C. Canalias, and V. Pasiskevicius, "Low-threshold, mid-infrared backward-wave parametric oscillator with periodically poled Rb:KTP," APL Photonics, vol. 3, p. 071302, 2018.

[120] G. Ghione, "Semiconductor Devices for High-Speed Optoelectronics," in Semiconductor Devices for High-Speed Optoelectronics, pp. 356–439, Cambridge University Press, 2009.

[121] R. S. Weis and T. K. Gaylord, "Lithium niobate: Summary of physical properties and crystal structure," Appl. Phys. A, vol. 37, pp. 191–203, 1985.

[122] M. Schröder, A. Haußmann, A. Thiessen, E. Soergel, T. Woike, and L. M. Eng, "Conducting Domain Walls in Lithium Niobate Single Crystals," Adv. Funct. Mater., vol. 22, pp. 3936–3944, 2012.

[123] K. Buse, A. Adibi, and D. Psaltis, "Non-volatile holographic storage in doubly doped lithium niobate crystals," Nature, vol. 393, pp. 665–668, 1998.

[124] A. Bartasyte, S. Margueron, T. Baron, S. Oliveri, and P. Boulet, "Toward High-Quality Epitaxial $LiNbO_3$ and $LiTaO_3$ Thin Films for Acoustic and Optical Applications," Adv. Mater. Interfaces, vol. 4, p. 1600998, 2017.

[125] L. Chang, Y. Li, N. Volet, L. Wang, J. Peters, and J. E. Bowers, "Thin film wavelength converters for photonic integrated circuits," Optica, vol. 3, pp. 531–535, 2016.

[126] P. O. Weigel and S. Mookherjea, "Design of folded hybrid silicon carbide-lithium niobate waveguides for efficient second-harmonic generation," J. Opt. Soc. Am. B, vol. 35, no. 3, pp. 593–600, 2018.

[127] M. Rüsing, P. O. Weigel, J. Zhao, and S. Mookherjea, "Toward 3D Integrated Photonics Including Lithium Niobate Thin Films: A Bridge between Electronics, Radio Frequency, and Optical Technology," IEEE Nanotechnol. Mag., vol. 13, no. 4, pp. 18–33, 2019.

[128] J. Zhao, M. Rüsing, M. Roeper, L. M. Eng, and S. Mookherjea, "Poling thin-film x-cut lithium niobate for quasi-phase matching with sub-micrometer periodicity," J. Appl. Phys., vol. 127, p. 193104, 2020.

[129] J. T. Nagy and R. M. Reano, "Fabricating Periodically Poled Lithium Niobate Thin Films with Sub-Micrometer Fundamental Period," in Frontiers in Optics/Laser Science, p. JTu3A.10, 2019.

[130] J. T. Nagy and R. M. Reano, "Reducing leakage current during periodic poling of ion-sliced x-cut MgO doped lithium niobate thin films," Opt. Mater. Express, vol. 9, pp. 3146–3155, 2019.

[131] V. Gopalan, V. Dierolf, and D. A. Scrymgeour, "Defect–Domain Wall Interactions in Trigonal Ferroelectrics," Annu. Rev. Mater. Res., vol. 37, no. 1, pp. 449–489, 2007.

[132] T. Jach, S. Kim, V. Gopalan, S. Durbin, and D. Bright, "Long-range strains and the effects of applied field at 180° ferroelectric domain walls in lithium niobate," Phys. Rev. B, vol. 69, p. 064113, 2004.

[133] K. Hassani, M. Sutton, M. Holt, Y. Zuo, and D. Plant, "X-ray diffraction imaging of strain fields in a domain-inverted $LiTaO_3$ crystal," J. Appl. Phys., vol. 104, p. 043515, 2008.

[134] V. Dierolf and C. Sandmann, "Confocal two photon emission microscopy: A new approach to waveguide imaging," J. Lumin., vol. 102-103, pp. 201–205, 2003.

[135] V. Dierolf and C. Sandmann, "Inspection of periodically poled waveguide devices by confocal luminescence microscopy," Appl. Phys. B, vol. 78, no. 3-4, pp. 363–366, 2004.

[136] C. L. Jia, S. B. Mi, K. Urban, I. Vrejoiu, M. Alexe, and D. Hesse, "Atomic-scale study of electric dipoles near charged and uncharged domain walls in ferroelectric films," Nat. Mater., vol. 7, no. 1, pp. 57–61, 2008.

[137] Y. B. Chen, M. B. Katz, X. Q. Pan, R. R. Das, D. M. Kim, S. H. Baek, and C. B. Eom, "Ferroelectric domain structures of epitaxial (001) $BiFeO_3$ thin films," Appl. Phys. Lett., vol. 90, p. 072907, 2007.

[138] J. Padilla, W. Zhong, and D. Vanderbilt, "First-principles investigation of 180° domain walls in BaTiO3," Phys. Rev. B, vol. 53, pp. R5969–R5973, 1996.

[139] B. Meyer and D. Vanderbilt, "Ab initio study of ferroelectric domain walls in $PbTiO_3$," Phys. Rev. B, vol. 65, no. 10, p. 104111, 2002.

[140] D. A. Scrymgeour, V. Gopalan, A. Itagi, A. Saxena, and P. J. Swart, "Phenomenological theory of a single domain wall in uniaxial trigonal ferroelectrics: Lithium niobate and lithium tantalate," Phys. Rev. B, vol. 71, p. 184110, 2005.

[141] S. Kim and V. Gopalan, "Optical index profile at an antiparallel ferroelectric domain wall in lithium niobate," Mater. Sci. Eng., B, vol. 120, no. 1-3, pp. 91–94, 2005.

[142] A. Turygin, D. Alikin, Y. Alikin, and V. Shur, "The formation of self-organized domain structures at non-polar cuts of lithium niobate as a result of local switching by an SPM tip," Materials, vol. 10, p. 1143, 2017.

[143] M. Younesi, P. Kumar, B. J. Stanicki, R. Geiss, W.-K. Chang, Y.-H. Chen, F. Setzpfandt, and T. Pertsch, "Periodic Poling with Short Period for Thin Film Lithium Niobate Waveguides," in CLEO Europe and EQEC, p. ck_8_4, 2019.

[144] H. Steigerwald, F. Von Cube, F. Luedtke, V. Dierolf, and K. Buse, "Influence of heat and UV light on the coercive field of lithium niobate crystals," Appl. Phys. B, vol. 101, no. 3, pp. 535–539, 2010.

[145] C. L. Sones, A. C. Muir, Y. J. Ying, S. Mailis, R. W. Eason, T. Jungk, Á. Hoffmann, and E. Soergel, "Precision nanoscale domain engineering of lithium niobate via UV laser induced inhibition of poling," Appl. Phys. Lett., vol. 92, p. 072905, 2008.

[146] B. Stanicki, M. Younesi, F. Löchner, H. Thakur, W.-K. Chang, R. Geiss, F. Setzpfandt, Y.-H. Chen, and T. Pertsch, "Surface domain engineering in lithium niobate," OSA Continuum, vol. 3, no. 2, pp. 345–358, 2020.

[147] P. A. Franken, A. E. Hill, C. W. Peters, and G. Weinreich, "Generation of optical harmonics," Physical Review Letters, vol. 7, no. 4, pp. 118–119, 1961.

[148] T. H. Maiman, "Stimulated Optical Radiation in Ruby," Nature, vol. 187, no. 4736, pp. 493–494, 1960.

[149] J. A. Armstrong, N. Bloembergen, J. Ducuing, and P. S. Pershan, "Interactions between light waves in a nonlinear dielectric," Physical Review, vol. 127, no. 6, pp. 1918–1939, 1962.

[150] P. Weigel and S. Mookherjea, "Design of folded hybrid silicon carbide-lithium niobate waveguides for efficient second-harmonic generation," J. Opt. Soc. Am. B, vol. 35, no. 3, pp. 593–600, 2018.

[151] S. S. Sané, S. Bennetts, J. E. Debs, C. C. N. Kuhn, G. D. McDonald, P. A. Altin, J. D. Close, and N. P. Robins, "11 W narrow linewidth laser source at 780nm for laser cooling and manipulation of Rubidium," Optics Express, vol. 20, no. 8, p. 8915, 2012.

[152] J. Zhao, M. Rüsing, and S. Mookherjea, "Optical diagnostic methods for monitoring the poling of thin-film lithium niobate waveguides," Opt. Express, vol. 27, no. 9, p. 12025, 2019.

[153] J. Kaneshiro, Y. Uesu, and T. Fukui, "Visibility of inverted domain structures using the second harmonic generation microscope: Comparison of interference and non-interference cases," J. Opt. Soc. Am. B, vol. 27, no. 5, pp. 888–894, 2010.

[154] D. A. Stocker, E. F. Schubert, W. Grieshaber, K. S. Boutros, and J. M. Redwing, "Facet roughness analysis for InGaN/GaN lasers with cleaved facets," Appl. Phys. Lett., vol. 73, no. 14, pp. 1925–1927, 1998.

[155] T. Umeki, O. Tadanaga, and M. Asobe, "Highly efficient wavelength converter using direct-bonded PPZnLN ridge waveguide," IEEE J. Quantum Electron., vol. 46, no. 8, pp. 1206–1213, 2010.

[156] M. Chauvet, F. Henrot, F. Bassignot, F. Devaux, L. Gauthier-Manuel, V. Pecheur, H. Maillotte, and B. Dahmani, "High efficiency frequency doubling in fully diced $LiNbO_3$ ridge waveguides on silicon," J. Opt., vol. 18, p. 085503, 2016.

[157] M. Neradovskiy, E. Neradovskaia, D. Chezganov, E. Vlasov, V. Y. Shur, H. Tronche, F. Doutre, G. Ayenew, P. Baldi, M. De Micheli, and C. Montes, "Second harmonic generation in periodically poled lithium niobate waveguides with stitching errors," J. Opt. Soc. Am. B, vol. 35, no. 2, pp. 331–336, 2018.

[158] L. Gui, Periodically Poled Ridge Waveguides and Photonic Wires in $LiNbO_3$ for Efficient Nonlinear Interactions. PhD thesis, University of Paderborn, 2010.

[159] O. Gayer, Z. Sacks, E. Galun, and A. Arie, "Temperature and wavelength dependent refractive index equations for MgO-doped congruent and stoichiometric $LiNbO_3$," Appl. Phys. B, vol. 91, pp. 343–348, 2008.

[160] I. H. Malitson, "Interspecimen Comparison of the Refractive Index of Fused Silica*†," J. Opt. Soc. Am., vol. 55, no. 10, pp. 1205–1209, 1965.

[161] J. H. Wray and J. T. Neu, "Refractive Index of Several Glasses as a Function of Wavelength and Temperature*," J. Opt. Soc. Am., vol. 59, no. 6, pp. 774–776, 1969.

[162] O. Alibart, V. D'Auria, M. D. Micheli, F. Doutre, F. Kaiser, L. Labonté, T. Lunghi, É. Picholle, and S. Tanzilli, "Quantum photonics at telecom wavelengths based on lithium niobate waveguides," Journal of Optics (United Kingdom), vol. 18, no. 10, 2016.

[163] J. E. Sharping, K. F. Lee, M. A. Foster, A. C. Turner, B. S. Schmidt, M. Lipson, A. L. Gaeta, and P. Kumar, "Generation of correlated photons in nanoscale silicon waveguides," Opt. Express, vol. 14, no. 25, pp. 12388–12393, 2006.

[164] I. W. Frank, J. Moore, J. K. Douglas, R. Camacho, and M. Eichenfield, "Entangled Photon Generation in Lithium Niobate Microdisk Resonators Through Spontaneous Parametric Down Conversion," in CLEO, p. SM2E.6, OSA, 2016.

[165] R. Luo, H. Jiang, S. Rogers, H. Liang, Y. He, and Q. Lin, "On-chip second-harmonic generation and broadband parametric down-conversion in a lithium niobate microresonator," Opt. Express, vol. 25, no. 20, pp. 24531–24539, 2017.

[166] A. Rao, N. Nader, M. J. Stevens, T. Gerrits, O. S. Magaña-Loaiza, G. F. Camacho-González, J. Chiles, A. Honardoost, M. Malinowski, R. Mirin, and S. Fathpour, "Photon Pair Generation on a Silicon Chip Using Nanophotonic Periodically-Poled Lithium Niobate Waveguides," in CLEO, p. JTh3C.2, OSA, 2018.

[167] L. G. Helt, M. Liscidini, and J. E. Sipe, "How does it scale? Comparing quantum and classical nonlinear optical processes in integrated devices," J. Opt. Soc. Am. B, vol. 29, pp. 2199–2212, 2012.

[168] S. F. Preble, M. L. Fanto, J. A. Steidle, C. C. Tison, G. A. Howland, Z. Wang, and P. M. Alsing, "On-Chip Quantum Interference from a Single Silicon Ring-Resonator Source," Phys. Rev. Appl., vol. 4, p. 21001, 2015.

[169] H. Jin, F. M. Liu, P. Xu, J. L. Xia, M. L. Zhong, Y. Yuan, J. W. Zhou, Y. X. Gong, W. Wang, and S. N. Zhu, "On-Chip Generation and Manipulation of Entangled Photons Based on Reconfigurable Lithium-Niobate Waveguide Circuits," Phys. Rev. Lett., vol. 113, p. 103601, 2014.

[170] M. Savanier, R. Kumar, and S. Mookherjea, "Photon pair generation from compact silicon microring resonators using microwatt-level pump powers," Opt. Express, vol. 24, p. 3313, 2016.

[171] W. C. Jiang, X. Lu, J. Zhang, O. Painter, and Q. Lin, "Silicon-chip source of bright photon pairs," Opt. Express, vol. 23, no. 16, p. 20884, 2015.

[172] M. Scholz, L. Koch, and O. Benson, "Statistics of Narrow-Band Single Photons for Quantum Memories Generated by Ultrabright Cavity-Enhanced Parametric Down-Conversion," Phys. Rev. Lett., vol. 102, p. 63603, 2009.

[173] X. Lu, Q. Li, D. A. Westly, G. Moille, A. Singh, V. Anant, and K. Srinivasan, "Chip-integrated visible–telecom entangled photon pair source for quantum communication," Nat. Phys., vol. 15, no. 4, pp. 373–381, 2019.

[174] T. Inagaki, N. Matsuda, O. Tadanaga, M. Asobe, and H. Takesue, "Entanglement distribution over 300 km of fiber," Opt. Express, vol. 21, pp. 23241–23249, 2013.

[175] M. Beck, "Comparing measurements of $g^{(2)}(0)$ performed with different coincidence detection techniques," J. Opt. Soc. Am. B, vol. 24, no. 12, pp. 2972–2978, 2007.

[176] P. Grangier, G. Roger, and A. Aspect, "Experimental Evidence for a Photon Anticorrelation Effect on a Beam Splitter: A New Light on Single-Photon Interferences," Europhys. Lett., vol. 1, no. 4, p. 173, 1986.

[177] A. B. Uren, C. Silberhorn, J. L. Ball, K. Banaszek, and I. A. Walmsley, "Characterization of the nonclassical nature of conditionally prepared single photons," Phys. Rev. A, vol. 72, no. 2, p. 021802(R), 2005.

[178] L. A. Ngah, O. Alibart, L. Labonté, V. D'Auria, and S. Tanzilli, "Ultra-fast heralded single photon source based on telecom technology," Laser & Photon. Rev., vol. 9, no. 2, pp. L1–L5, 2015.

[179] G. Brida, I. P. Degiovanni, M. Genovese, F. Piacentini, P. Traina, A. Della Frera, A. Tosi, A. Bahgat Shehata, C. Scarcella, A. Gulinatti, M. Ghioni, S. V. Polyakov, A. Migdall, and A. Giudice, "An extremely low-noise heralded single-photon source: A breakthrough for quantum technologies," Appl. Phys. Lett., vol. 101, no. 22, p. 221112, 2012.

[180] S. Krapick, H. Herrmann, V. Quiring, B. Brecht, H. Suche, and C. Silberhorn, "An efficient integrated two-color source for heralded single photons," New Journal of Physics, vol. 15, p. 033010, 2013.

[181] J. D. Franson, "Bell inequality for position and time," Phys. Rev. Lett., vol. 62, no. 19, pp. 2205–2208, 1989.

[182] P. G. Kwiat, A. M. Steinberg, and R. Y. Chiao, "High-visibility interference in a Bell-inequality experiment for energy and time," Phys. Rev. A, vol. 47, no. 4, pp. 2472–2475, 1993.

[183] J. F. Clauser and M. A. Horne, "Experimental consequences of objective local theories," Phys. Rev. D, vol. 10, no. 2, pp. 526–535, 1974.

[184] P. Main, P. J. Mosley, W. Ding, L. Zhang, and A. V. Gorbach, "Hybrid microfiber-lithium-niobate nanowaveguide structures as high-purity heralded single-photon sources," Phys. Rev. A, vol. 94, p. 063844, 2016.

[185] S. B. ELkus, K. Abdelsalam, A. Rao, V. Velev, S. Fathpour, P. Kumar, and S. G. Kanter, "Generation of broadband correlated photon-pairs in short thin-film lithium-niobate waveguides," Opt. Express, vol. 27, no. 26, pp. 38521–38531, 2019.

[186] A. M. Brańczyk, T. C. Ralph, W. Helwig, and C. Silberhorn, "Optimized generation of heralded Fock states using parametric down-conversion," New J. Phys., vol. 12, p. 063001, 2010.

[187] C. K. Law, I. A. Walmsley, and J. H. Eberly, "Continuous frequency entanglement: Effective finite hilbert space and entropy control," Phys. Rev. Lett., vol. 84, no. 23, pp. 5304–5307, 2000.

[188] J. P. Höpker, T. Gerrits, A. Lita, S. Krapick, H. Herrmann, R. Ricken, V. Quiring, R. Mirin, S. W. Nam, C. Silberhorn, and T. J. Bartley, "Integrated transition edge sensors on titanium in-diffused lithium niobate waveguides," APL Photonics, vol. 4, no. 5, p. 056103, 2019.

[189] G. B. Dorjin and I. G. Simakov, "Acoustic study of adsorbed liquid layers," Acoust. Phys., vol. 48, no. 4, pp. 436–440, 2002.

[190] N. Montaut, L. Sansoni, E. Meyer-Scott, R. Ricken, V. Quiring, H. Herrmann, and C. Silberhorn, "High-efficiency plug-and-play source of heralded single photons," Phys. Rev. Appl., vol. 8, no. 2, p. 024021, 2017.